

Spring 2015

Ablation of Cardiac Tissue with Nanosecond Pulsed Electric Fields: Experiments and Numerical Simulations

Fei Xie
Old Dominion University

Follow this and additional works at: https://digitalcommons.odu.edu/biomedengineering_etds



Part of the [Bioelectrical and Neuroengineering Commons](#), and the [Bioimaging and Biomedical Optics Commons](#)

Recommended Citation

Xie, Fei. "Ablation of Cardiac Tissue with Nanosecond Pulsed Electric Fields: Experiments and Numerical Simulations" (2015). Doctor of Philosophy (PhD), Dissertation, Electrical & Computer Engineering, Old Dominion University, DOI: 10.25777/kn1z-b503
https://digitalcommons.odu.edu/biomedengineering_etds/5

This Dissertation is brought to you for free and open access by the Biomedical Engineering at ODU Digital Commons. It has been accepted for inclusion in Biomedical Engineering Theses & Dissertations by an authorized administrator of ODU Digital Commons. For more information, please contact digitalcommons@odu.edu.

**ABLATION OF CARDIAC TISSUE WITH NANOSECOND PULSED
ELECTRIC FIELDS: EXPERIMENTS AND NUMERICAL
SIMULATIONS**

by

Fei Xie

B.Eng. July 2004, Chongqing University, China
M.Sc. March 2006, University of Southampton, UK

A Thesis Submitted to the Faculty of
Old Dominion University in Partial Fulfillment of the
Requirements for the Degree of

DOCTOR OF PHILOSOPHY
BIOMEDICAL ENGINEERING
OLD DOMINION UNIVERSITY

May 2015

Approved by:

Christian Zemlin (Director)

Shu Xiao (Member)

Michel Audette (Member)

Jiang Li (Member)

UMI Number: 3663143

All rights reserved

INFORMATION TO ALL USERS

The quality of this reproduction is dependent upon the quality of the copy submitted.

In the unlikely event that the author did not send a complete manuscript and there are missing pages, these will be noted. Also, if material had to be removed, a note will indicate the deletion.



UMI 3663143

Published by ProQuest LLC 2015. Copyright in the Dissertation held by the Author.

Microform Edition © ProQuest LLC.

All rights reserved. This work is protected against unauthorized copying under Title 17, United States Code.



ProQuest LLC
789 East Eisenhower Parkway
P.O. Box 1346
Ann Arbor, MI 48106-1346

ABSTRACT

ABLATION OF CARDIAC TISSUE WITH NANOSECOND PULSED ELECTRIC FIELDS: EXPERIMENTS AND NUMERICAL SIMULATIONS

Fei Xie

Old Dominion University, 2015

Director: Dr. Christian Zemlin

Cardiac ablation for the treatment of cardiac arrhythmia is usually performed by heating tissue with radio-frequency (RF) electrical currents to create conduction-blocking lesions in order to stop the propagation of electrical waves. Problems associated with RF ablation are recurrence of arrhythmias after successful treatments, tissue loss beyond the targeted tissue, long duration of the ablation procedure, and thermal side effects including thrombus formation that may lead to stroke. Here, we propose a new, non-thermal ablation method using nanosecond pulsed electric fields (nsPEFs) with better-controlled ablation volume, shorter procedure time, and no thermal side effects. We demonstrate that we can create non-conductive transmural lesions using different electrode configurations. We also develop a numerical model of nsPEF ablation, which allows us to estimate the critical electric field which leads in cardiac tissue and helps to provide a guideline for clinical tissue ablation.

Our experimental model is a Langendorff-perfused rabbit heart. The heart is placed in a life-support system, and optical mapping is performed to study its electrical activity. We further developed the capability to apply short sequences of nanosecond pulses to tissue through pairs of customized electrodes. In order to characterize the 3D geometry of an

ablated volume, we have adopted propidium iodide and TTC staining in conjunction with tissue sectioning. Our results obtained by optical mapping data and PI/TTC stained tissue show that fully transmural lesions can be obtained faster and with better control over the ablated volume than in conventional (RF) ablation, in the absence of thermal side effects.

In order to aid nsPEF ablation planning, we used the COMSOL finite element software to create a model of the electric field distribution in cardiac tissue, which has a complex anisotropic architecture, for different electrode configurations. The experimental and numerical results are consistent and suggest a critical electric field strength of 3kV/cm for the death of cardiac tissue. This threshold obtained by the numerical model can function as a guideline for future clinical nsPEF treatment of atrial fibrillation.

In summary, we have developed nsPEF ablation for the treatment of cardiac arrhythmia to provide better control over the ablated volume than conventional (RF) ablation, to reduce procedure time, and to avoid thermal side effects. Our ultimate goal is to bring this technology to the clinical practice.

Copyright, 2015, by Fei Xie, All Rights Reserved.

This thesis is dedicated to my parents, my wife Xintong Li and to all the people who helped me with a glass of water when I was thirsty (Matthew 25:35).

ACKNOWLEDGMENTS

First and foremost, praise and thanks goes to my savior Jesus Christ for the many blessings undeservingly bestowed upon me. He answered my prayer in 2008 when I was in China, before I got the opportunity to come to the United States to do my PhD research in August 2009, and faithfully answered it again in early 2012 before I met my current PhD advisor. By His unmeasurable grace and unfailing love, I was able to continue my research at the most difficult and confusing time, and could accomplish this wonderful PhD project.

I cannot image to accomplish this project, without the help and guidance from my respected PhD advisor, Dr Christian Zemlin. I feel extremely privileged and grateful for his tremendous patience of instruction, high standard academic training, and generous financial support, in the past 3 years. I am especially grateful for his continued patience at all kinds of academic activities: from experiments of rabbit surgery, coursework evaluation, paper editing, debugging of C++ codes, to my PhD dissertation editing. Beyond the academics, his humorous and easy-going personality makes me feel very comfortable to work with. I remember once I was later for a group meeting for almost 20 minutes in the morning, due to the incident of silent alarm, but he did not blame me for the late present. During the last 3 years, we had several chances of having conferences out of town, and I really appreciate these experiences. I will remember all the unforgettable experiences I had with Dr Zemlin in the Cardiac EP lab.

Secondly, I would also like to deeply thank my co-advisor and co-author Dr. Shu Xiao, who helped me with countless technical discussions and valuable suggestions on the nanosecond pulser. I am always encouraged after our discussions, and I also appreciate his

recommendation to Dr. Zemlin for me.

I also want to express my sincere gratitude to my co-worker in the organization of Chinese Students & Scholars Bible Study Group, Yuming Geng, for his unselfish support every Saturday to cook the meal for all of us, in the BCM church in 49th Street, from Dec 2011 until now. I am so grateful that God give me this nice and gentle co-worker, and his countless love on many people indeed can be a good example of Christ follower.

Also thanks for the time committed by my PhD committee members Dr Michel Audette and Dr Jiang Li, for my diagnostics, candidacy exam, and PhD defense. Also thank Dr Thomas Vernier for our discussion about effect of electroporation on conductivity.

I also want to extend my appreciation of the friendship I had during my study in ODU: my funny roommate, “rabbit” Xiao Lin and later the “marriage expert” Dr. Yanan Wang; my neighbors in 1055: “astrophysicist” Zhaohui Li (thanks for his time discussion about dipole), “AP man” Hao Qiu (thanks for his time discussion about COMSOL), “Lao Wang” Xianping Wang, and my former lab mate “OT” Ren Wang (thanks for his help in my previous MEMS lab).

Last, not not least, I would like to thank my grandma, 丁芝玲 and 林恒仙, my passed away grandpa 熊彦生 and 谢和芳, my respected and unconditional loving parents 谢增余 and 张新华, and my lovely wife, Xintong Li, for her prayers in front of the Lord.

TABLE OF CONTENTS

	Page
LIST OF TABLES	x
LIST OF FIGURES	xi
 Chapter	
1. INTRODUCTION	1
1.1 Ablation of cardiac tissue with RF ablation and cryoablation	1
1.2 Limitations of RF ablation & cryoablation	2
1.3 Irreversible electroporation ablation and related research by other groups	6
1.4 Advantages of using nsPEF ablation	10
1.5 Numerical simulations	12
 2. METHODS	 15
2.1 General approach	15
2.1.1 Animal surgery	16
2.1.2 Langendorff-perfused heart in the life-support system	16
2.1.3 Optical mapping system	18
2.1.4 Mechanism of voltage-sensitivity	19
2.1.5 PI / TTC staining and sectioning	20
2.2 Nanosecond pulse generation with pulse forming lines	22
2.3 Stimulator, temperature sensor and pressure sensor	24
2.4 GUI controlling panel	26
2.5 Electrodes configurations	32
2.6 Mathematical model of nsPEF ablation	36
2.6.1 Cardiac fiber orientation	38
2.6.2 Numerical modeling equations	43
2.6.3 COMSOL simulations	45
 3. EXPERIMENTAL RESULTS	 48
3.1 Single application ablation testing	49
3.2 Faster single application ablation	55
3.3 Multiple application ablations to create lesions	57
3.4 Lesion width statistics	65
3.5 Experimental results for endo-epi configurations	67
3.6 Discussion	70
 4. NUMERICAL SIMULATION RESULTS	 71
4.1 Numerical results for penetrating electrodes configuration	71
4.1.1 Explanation of indentation of electric field distribution	71
4.1.2 Joule heating analysis	74
4.1.3 Electric field distribution for smoothly varying fiber direction	75

4.1.4 Comparison of numerical and experimental results for penetrating configuration	77
4.2 Endo-epi and endo-endo configurations	82
4.2.1 Comparison of numerical and experimental results for endo-epi configuration	84
4.3 Numerical modeling for human left ventricle ablation.....	84
4.4 Numerical modeling for human atrium ablation.....	89
4.5 Limitations of our numerical model	91
4.6 Discussion.....	93
5. CONCLUSIONS AND FUTURE WORK	95
5.1 Conclusions.....	95
5.2 Future work.....	96
5.2.1 Inclusion of membrane permeabilization into numerical model	98
5.2.2 Synergy ablation clamp design	99
REFERENCES	102
VITA	111

LIST OF TABLES

Table	Page
1. Different types of radio frequency ablation catheters and their strengths and weaknesses.....	3
2. List of built-in programs of Little Joe	30
3. Geometry and dielectric property of tissue and electrodes	46

LIST OF FIGURES

Figure	Page
1. Schematic drawing of radio frequency catheter ablation on the cardiac tissue demonstrating the region of resistive heating of blood and tissue and convective heat loss from into the circulating blood pool and epicardial coronary arteries	2
2. Thrombus at the electrode-tissue interface produced by RF ablation delivered with a closed loop electrode in low blood flow.....	4
3. Myocardial sections containing representative radio frequency lesions created by the open irrigated tip.....	5
4. Diagram of lesion dimensions [mm] for RF applications with closed-irrigated and open irrigated tip in different blood flow (0.1 m/s and 0.5m/s)	6
5. Schematic diagram illustrating reversible and irreversible electroporation	7
6. Schematic diagrams for RF ablation and different electrode configurations for nsPEF ablation of myocardial tissue	8
7. Proof of principle of line ablation with microsecond pulses	9
8. Millisecond shock ablation with ring-shaped electrodes	10
9. Overlay of electric-field contours predicted by the numerical model onto live/dead cells after 300 V (a) and 450 V (b) are applied through a pair of electrodes in the center	12
10. Electric field, conductivity, temperature and thermal damage distributions after an 80s IRE treatment of tumor ablation in the brain.....	13
11. Electric field distribution for isotropic and anisotropic skeletal muscle conductivity	14
12. Langendorff-perfused heart in the life support system	17
13. Typical optical mapping system consisting of three major components: 1) the heart preparation; 2) illumination; and 3) a detector	18

14. Mechanism of voltage-sensitive dye.....	20
15. Schematic diagram of the pulser (A) and the ideal square pulse it produces (B).....	22
16. Comparison of matching resistance using different resistors	23
17. Stimulator (shown as a straight black insulated metal wire) placed onto the surface of Langendorff-perfused rabbit heart	26
18. Screen shot of GUI for data control and processing	27
19. Chinese characters captured by the camera “Little Joe” with programmed features.....	29
20. Space running average filtering and time running average filtering.....	31
21. Post-processed signal after spacing and temporal averaging, flipping, subtracting the minimum and stretching.....	30
22. Penetrating electrodes design.....	33
23. Penetrating electrodes in a rabbit heart.....	34
24. Electrode design for the endo-endo configuration.....	35
25. Electrode design for the endo-epi configuration.....	35
26. Heart preparation for endo-epi experiment.....	37
27. Electrode setup for the endo-epi configuration.....	38
28. Cardiac fiber structure.....	39
29. Schematic diagram of muscle fiber orientation in myocardium.....	40
30. Typical sequence of photomicrographs showing fiber angles in successive sections taken from a heart (Left column: canine, right column: murinae).....	41
31. Transmural trajectories of the myocardial fiber helix angle obtained by DTI datasets of fixed, intact normal mouse, rabbit and sheep hearts.....	42
32. Regions of interest for left ventricular myocardial fiber helix angles analysis	43
33. Definition of fiber helix angle α for COMSOL numerical model	46

34. Mesh of the physical model	47
35. Single ablation shows the action potentials can be blocked successfully in the targeted region (2kV, 20 pulses at the frequency of 1 Hz, 2 mm electrode spacing)	49
36. Smaller ablated area obtained with lower pulse amplitude (1.5kV, 20 pulses at the frequency of 1 Hz, 2 mm electrodes spacing)	50
37. Incomplete ablated area (0.7kV, 20 pulses at the frequency of 1 Hz, 2 mm electrode spacing).....	50
38. 4 mm electrodes spacing ablated area (2 kV, 20 pulses at the frequency of 1 Hz, 4 mm electrode spacing).....	51
39. PI fluorescence rabbit cardiac tissue images for ablation with different parameters	52
40. Comparison of different amplitude of pulses applied for 4 mm electrodes spacing ...	53
41. Three-dimensional reconstruction of the ablated volume (4 kV, 20 pulses, 4 mm electrodes spacing)	54
42. Cardiac surface before and after an ablation (2.3kV, 5 pulses at the frequency of 3Hz with 2mm electrodes spacing)	56
43. Determining optimal orientation for lesions to best demonstrate non-conductiveness using activation map.....	57
44. Different ways of creating lesions from single application ablations.....	59
45. Optical mapping data verifies that lesions were created successfully by multiple ablations on left ventricle of rabbit heart.....	60
46. Two more successful nsPEF lesions, one created on the left ventricle (upper row) and one on the right ventricle (lower row) of a rabbit heart.....	61
47. TTC stained sectioned tissue with lesions created using 2.3kV, 5 pulses at a frequency of 3Hz with 2mm electrode spacing for both columns	63
48. Microphotographs of the marked regions in Figure 47	64

49. 3D re-construction for the TTC sectioned tissue on the left column of Figure 50	65
50. Lesion width statistics and standard deviation for different pulse amplitudes.	66
51. Cross sections of nsPEFs ablated tissue stained with TTC with 6.5 kV, 6 pulses at the frequency of 3 Hz	68
52. Sections of an ablation volume created with the endo-epi electrode configuration	69
53. Electric field norm distribution changes due to different value of σ_L / σ_T	72
54. E_x , E_y , and the norm of the electric field for different anisotropy ratios	73
55. Illustration of local electric field distribution due to different fiber orientations.	74
56. Temperature distribution in our model after one shock (2.3 kV, 350 ns) is applied between penetrating electrodes with 2 mm separation.....	75
57. Comparison of theoretical simulation of electric field distribution with experimental results obtained from PI stained ablated area	76
58. Isosurface of electric field strength ($E= 3$ kV/cm) induced in tissue with twisted anisotropy with electrodes aligned in x-axis (upper row) and y-axis (bottom row).	77
59. The human heart in cross section, similar structure can be found for rabbit heart	79
60. Superposition of the projection of the isosurface of electric field strength ($E= 3$ kV/cm) from numerical model (green) onto sectioned TTC stained tissue ablated by 2.3 kV, 5 pulses at 3Hz with 2 mm spacing, from epicardium to endocardium	80
61. Superposition of the projection of the isosurface of electric field strength ($E= 3$ kV/cm) from numerical model (red) onto sectioned PI stained tissue ablated by 4kV, 20 pulses at 1Hz with 4 mm spacing, from epicardium to endocardium	81
62. Isosurface (3 kV/cm) plotting of electric field distribution with 6.5kV shocks applied for endo-epi electrodes configuration.....	82
63. Isosurface (3 kV/cm) plotting of electric field distribution with 9kV shocks applied for endo-endo electrodes configuration.....	83
64. Superposition of critical electric field of 3 kV/cm with same electrode radius from numerical simulation onto the experimental results from Figure 51 and 52	84

65. DTMRI-acquired fiber orientation at different subdivisions in the left ventricle.....	85
66. Isosurface (3 kV/cm) for 2.3 kV shocks applied with the penetrating electrodes configuration	87
67. Isosurface (3 kV/cm) for 4.1 kV shocks applied for endo-epi electrodes configuration	88
68. Schematic diagram of serial dissections from subepicardium to subendocardium (left to right) in the left atrium to display the atrial myoarchitecture in a normal human heart	89
69. Isosurface (3 kV/cm) for 1.8 kV shocks applied for penetrating electrodes configuration	90
70. Isosurface (3 kV/cm) for 2.3 kV shocks applied for endo-epi electrodes configuration	91
71. Electrical conductivity versus electric field with different pulse widths at $24\pm 2^{\circ}\text{C}$	92
72. Schematic diagram of the four-electrode technique for measuring tissue conductivities.....	98
73. Synergy ablation clamp.....	100
74. Ablation protocol using AtriCure synergy ablation clamp.....	101

CHAPTER I

INTRODUCTION

1.1 ABLATION OF CARDIAC TISSUE WITH RF ABLATION AND CRYOABLATION

Ablation of myocardial tissue is an essential technique for the treatment of atrial fibrillation (AF), the most common cardiac arrhythmia, with about 3 million affected in the United States alone¹. Patients with AF have a fivefold increase in the risk of stroke^{2,3}, accounting for approximately 15% of all strokes nationally⁴, and their quality of life is significantly reduced⁵. In the normally functioning heart, the natural pacemaker creates periodic activations that travel as activation waves first across the atria and then across the ventricles and induce the contraction of muscle cells as they pass⁶. During atrial fibrillation, this activation mechanism is disturbed, either by pathologic activations from sources other than the natural pacemaker, or by abnormal propagation patterns such as spiral waves or reentry⁷. The first therapy for AF patients is usually pharmacological, but this yields satisfactory results in only about half the patients⁴. For the remaining half, the most common therapy is radio frequency (RF) ablation, a procedure in which conduction-blocking lesions are created in the atria in order to stop AF⁸. It is estimated that approximately 100,000 patients in the United States receive RF ablation therapy every year⁹.

RF ablation involves a catheter which is inserted into the heart for delivery of ablation energy to kill a volume of cardiac tissue. RF ablation works by applying heat via an intra-atrial catheter to the endocardium until the tissue around the catheter is destroyed; the catheter is then moved slightly and the procedure repeated. The ablation energy is delivered by an AC current at a frequency between 350-750 kHz¹⁰ between an catheter tip electrode resting on the endocardium and a grounding patch placed on the body surface (also known as a dispersive electrode, it has a much greater surface area than the catheter tip to minimize any heat delivered to the skin as current flows through the patch). RF frequencies are high enough to prevent the induction of ventricular

fibrillation¹¹.

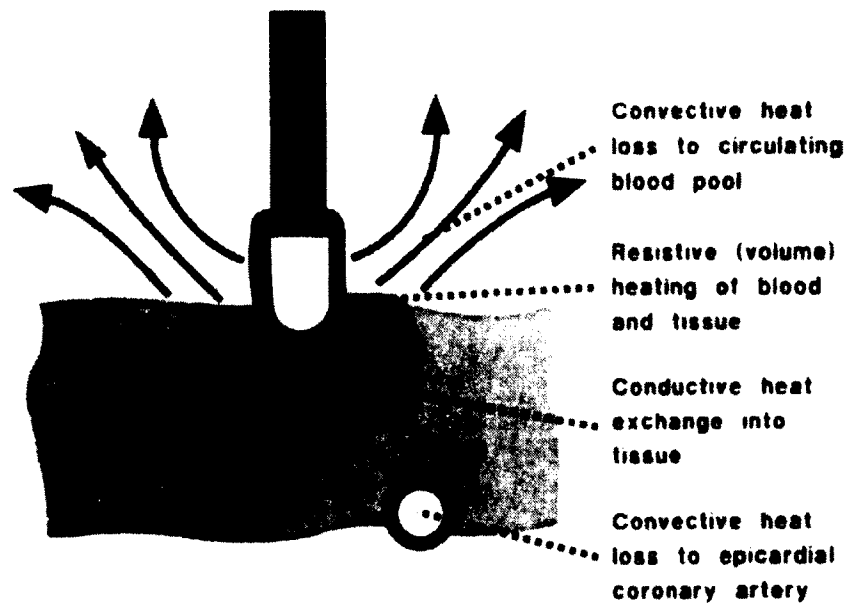


Figure 1. Schematic drawing of radio frequency catheter ablation on the cardiac tissue demonstrating the region of resistive heating of blood and tissue and convective heat loss from into the circulating blood pool and epicardial coronary arteries⁹⁶.

Heating of the tissue around the catheter tip occurs in two ways: resistive heating and conductive heating (Figure 1). Resistive heating occurs in the layers of tissue adjacent to the electrode as the AC current passes through. At the same time, the generated heat is transported to neighboring regions via heat conduction. The resulting lesion size is determined by the balance of tissue conductive heat generation and convective heat loss carried away by tissue blood flow (Figure 1). Thus, lesion volume can be influenced by tissue blood flow within an area below the catheter tip.

The only alternative to RF ablation in clinical practice today is cryoablation¹². Since the late 1990s, cryoablation has evolved as an alternative to conventional RF ablation¹³. The catheter tip is cooled to -70°C to -80°C by means of liquid NO_2 injected into the catheter^{14, 15}.

1.2 LIMITATIONS OF RF ABLATION & CRYOABLATION

Both RF and cryoablation have limitations related to their thermal nature. At present, there are four major types of radio frequency (RF) catheter ablation systems available for clinical use in the United States: (1) standard 4-mm-tip catheters; (2) large 8–10-mm-tip catheters; (3) open-loop irrigated-tip catheters; and (4) closed-loop irrigated-tip catheters (Table 1).





Catheter	Electrodes	RF Delivery	Advantages	Disadvantages
Standard 4-mm-tip		RF energy delivery	Predictable lesion size Good signal resolution	Limited power delivery Smaller lesion volume and depth
Large 10-mm-tip		Passive cooling due to large surface area enables more power delivery	Larger lesion volume and depth	Reduced signal resolution Thrombus and char formation Steam pop
Open-irrigated 3.5-mm-tip		External irrigation cools electrode and tissue interface, allows greater power delivery	Increased lesion depth and volume Good signal resolution	Intravascular fluid overload Risk of steam pops
Closed-irrigated 4-mm-tip		Internal irrigation cools electrode, allows greater power delivery	Increased lesion depth and volume Good signal resolution	Risk of thrombus formation Risk for steam pops

Table 1. Different types of radio frequency ablation catheters and their strengths and weaknesses⁹⁵.

A simple way to explain the evolution of these technologies is as follows: standard tip 4 mm electrode are the simplest design and were the first electrodes used. Their main limitation is limited lesion depth. To get deeper lesions, the tip size was increased, but this also increased the thermal load on the tissue and led to serious side effects such as thrombus formation (blood around the

ablated area to clot) at the endocardial surface (Figure 2). To get deep lesions without side effects from heating, researchers started cooling the tip, either by circulating cooling liquid inside the tip (closed irrigation), or by expelling it through small holes at the tip (open irrigation). Open irrigation reduces heat related side effects more effectively, but it can lead to intravascular fluid overload.

A major problem in RF ablation is that it is hard to know exactly how much RF power is needed to ensure a complete lesion. Since incomplete lesions are ineffective, clinicians usually use relatively high power and wide lesions to make sure all lesions are complete^{12, 16} but this leads to substantial loss of tissue, and severe thermal side effects can occur.

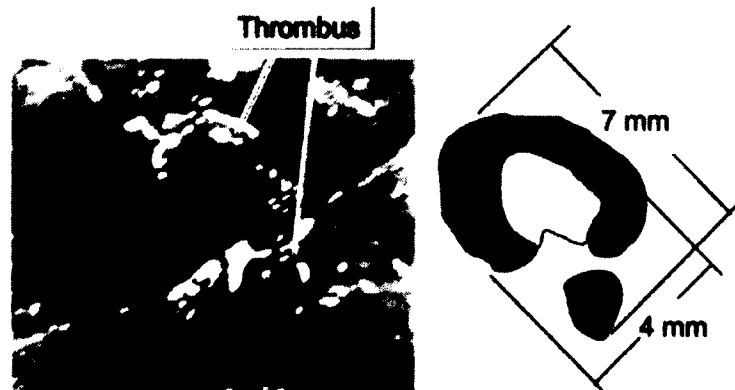


Figure 2. Thrombus at the electrode-tissue interface produced by RF ablation delivered by a closed loop electrode in low blood flow. The thrombus formed on the electrode-tissue interface surrounding the ablation electrode. The size of the thrombus outline on the right was 7x4 mm²¹.

In general, high temperatures are needed to make sure that all layers of the tissue are ablated. However, these high temperatures can also lead to blood and tissue accumulating on the catheter tip. This is known as char formation, or charring. When charring occurs, only the outer layer of tissue may be ablated, which means the lesion is not transmural. In addition, heat generated by radio frequency energy may also cause thrombus formation (blood around the ablated area to clot). If a clot were to dislodge from the heart, a stroke could occur.

The second concern with RF ablation is recurrence over the long term: in a substantial portion of the initially successful ablations, lesions eventually become conductive again and AF recurs¹⁷. The

third problem is that RF ablation is a lengthy procedure---a full ablation procedure usually takes 4-6 hours¹⁸. This is because a single ablation usually takes around 30-60 seconds to ablate the region transmurally due to the thermal mechanism. By repeating single ablations at different locations, transmural lesions can be created. Finally, since RF ablation uses heat to ablate cardiac tissue, the ablated area is not constant in all layers of the myocardium, but its cross section is elliptical (Figure 3). Figure 4 illustrates the cross-section geometry of lesions created by RF ablation using closed and open irrigation tips. A large number of research groups agrees on these basic geometries^{14, 19, 20, 21}. The geometries are all ellipsoidal, but the centers of the ellipsoids are different for different types of RF ablation. For closed irrigation, the center is either located at the surface of the cardiac tissue or slightly below the surface, depending on the flow rate of blood; for open irrigation, the center is located below the surface.



Figure 3. Myocardial sections containing representative radio frequency lesions created by the open irrigated tip. The cross sectioned area of ablated region is elliptical rather than rectangular⁹⁴.

The main limitation of using traditional cryoablation is that it has a slower and lower freezing capacity, with a mean time for the complete ablation procedure of approximately 25 to 30 minutes, and the endocardial freezing process needs a bloodless field²².

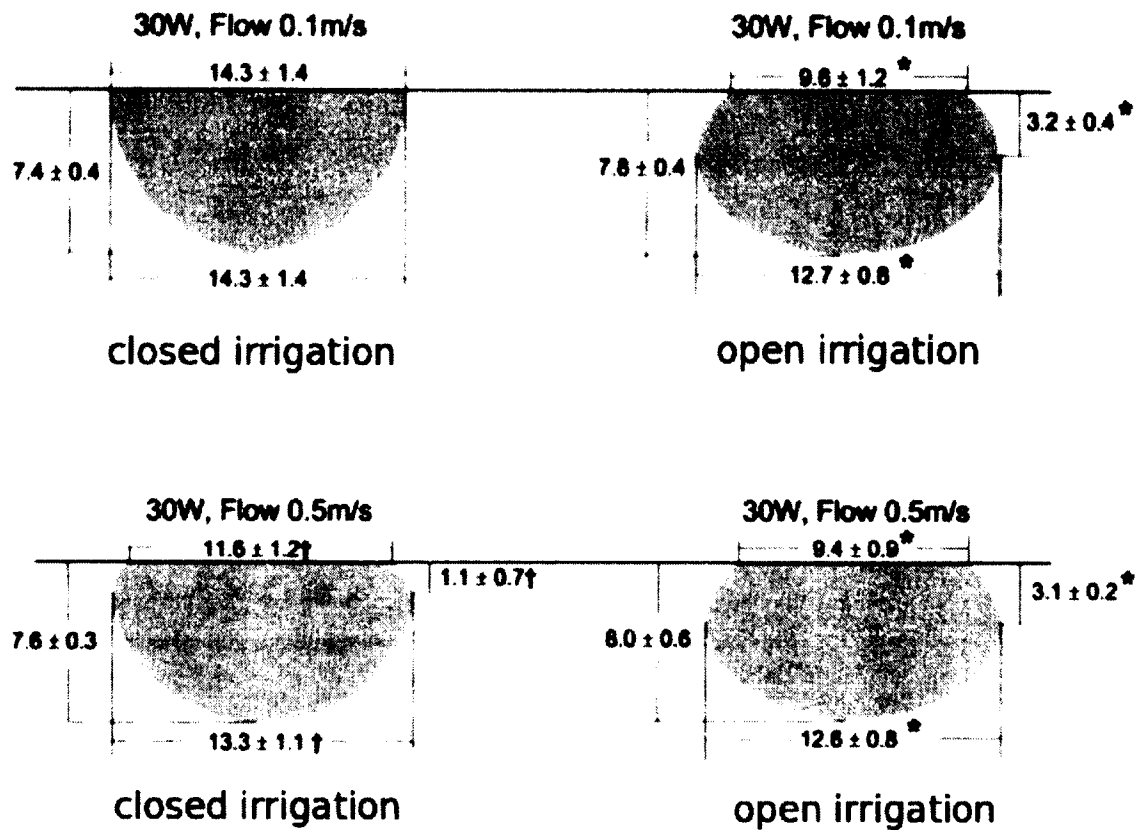


Figure 4. Diagram of lesion dimensions [mm] for RF applications with closed-irrigated and open-irrigated tip in different blood flow (0.1 m/s and 0.5m/s)²¹.

1.3 IRREVERSIBLE ELECTROPORATION ABLATION AND RELATED RESEARCH BY OTHER GROUPS

When electric fields of sufficient amplitude are applied to cells, there is a significant increase in the electrical conductivity and permeability of the cell plasma membrane. This phenomenon of cell membrane permeabilization is called electroporation; it is used in biotechnology and medicine for delivery of drugs and genes into living cells^{23, 24, 25, 26}. Electroporation can be described as the development of pores in the cell membrane (dramatic increase of membrane permeability) caused by external electric pulses, typically short and intense pulses. Depending on the induced transmembrane potential (the electric potential difference across the plasma membrane), electric

pulses can either have no effects on the cell membrane, reversibly porate the cell membrane (after which cells can survive), or irreversibly porate the cell membrane, resulting in structural rearrangement of the lipid bilayer (after which the cells die). These “pores” create permanent aqueous path ways for ions and macromolecules to pass through. Figure 5 illustrates the difference between reversible and irreversible electroporation.

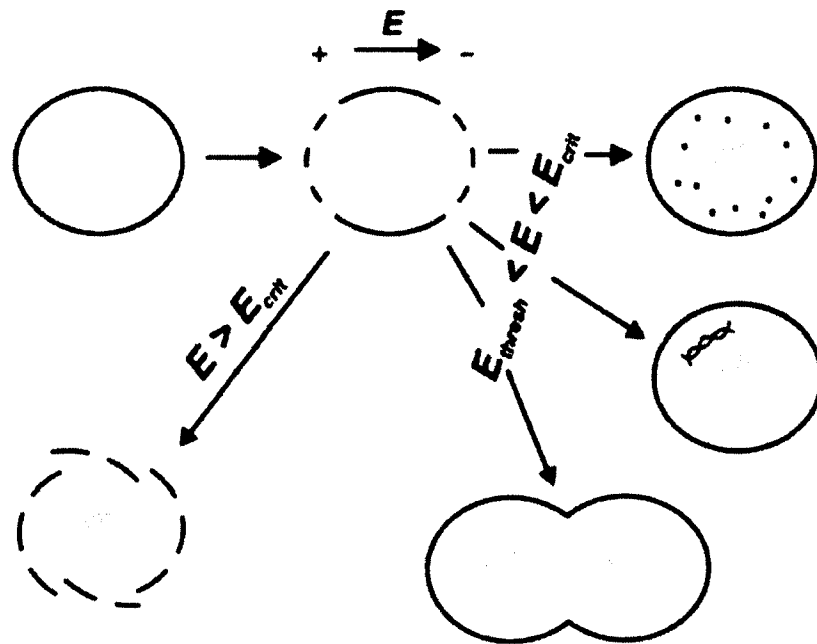


Figure 5: Schematic diagram illustrating reversible and irreversible electroporation. When the external electric field reaches threshold value (E_{thresh}), the cell membrane is electroporated. Molecules that are smaller than the induced size of pores can be introduced into the cell, or when two cells are in close contact, their membranes can fuse if $E_{thresh} < E < E_{crit}$. When the external electric field exceeds certain critical value (E_{crit}), irreversible electroporation occurs, resulting in cell membrane disintegration and cell death⁹².

In this project, we propose a new method to ablate myocardial tissue that uses nanosecond pulsed electric fields (nsPEFs) delivered by 3 different configurations of customized electrodes (Figure 6). Such high-intensity electric fields with short durations have been successfully used in tumor ablation^{27, 28, 29}, but not yet for cardiac tissue.

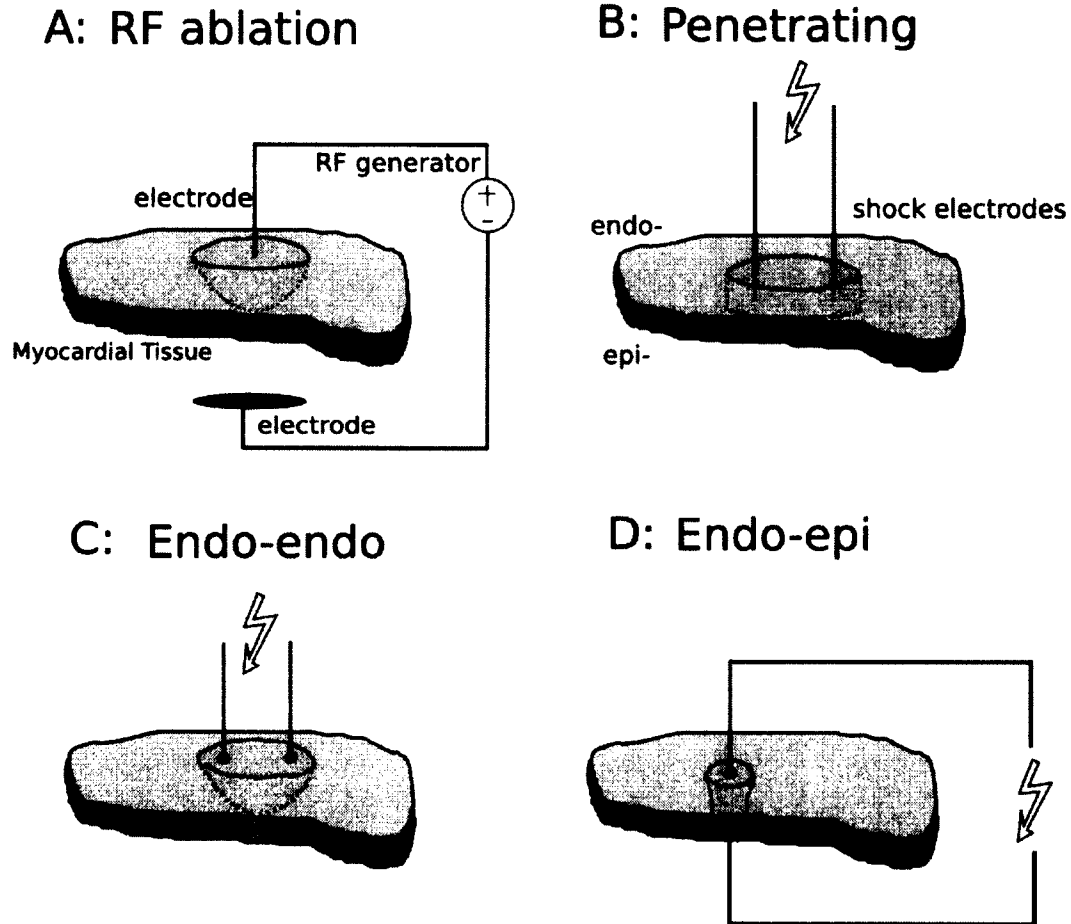


Figure 6. Schematic diagrams for RF ablation and different electrode configurations for nsPEF ablation of myocardial tissue. Pink slab shows the tissue. A typical region of ablation is marked yellow and enclosed by red lines. **A:** RF Ablation. **B:** Penetrating electrodes configuration. **C:** Endo-endo configuration. Two contact electrodes touch the endocardium. **D:** Endo-epi configuration. One contact electrode touches the endocardium, another the epicardium.

Figure 6 compares the standard electrode configuration for RF ablation with the electrode configurations we propose for nsPEF ablation. In the standard RF configuration (Panel A), one catheter electrode is placed on the endocardium, and the second, dispersive electrode is far away. Panel B shows the configuration that we have been using in most of our nsPEF ablations, with two thin electrodes penetrating the tissue. The endo-endo configuration in Panel C of Figure 6, uses two electrodes touching the endocardial surface without penetration. Compared to the other two nsPEF

electrode configurations, the endo-endo configuration is the most straightforward to implement; existing RF ablation (Panel A) catheters could be used with small modifications. The endo-epi configuration (Panel D) requires one endocardial and one thoracic catheter, but it works without tissue penetration and leads to ablation volumes with better geometries than those created with the endo-endo configuration (see Results sections).

Previous studies show that therapy based on irreversible electroporation (IRE) is effective for tumor ablation^{30, 31, 32}, especially in regions where precision and conservation of the extracellular matrix, such as blood vessel and nerves, are of importance^{33, 34}. The mechanism of cell death is related to the altered membrane permeability, not thermal effects. Using IRE-based *microsecond* pulsed electric fields (PEF), a proof of principle for cardiac tissue ablation was performed (Figure 7)³⁵. However, in that study caliper-shaped electrodes were used and compatibility with catheter-based surgery was not a concern.

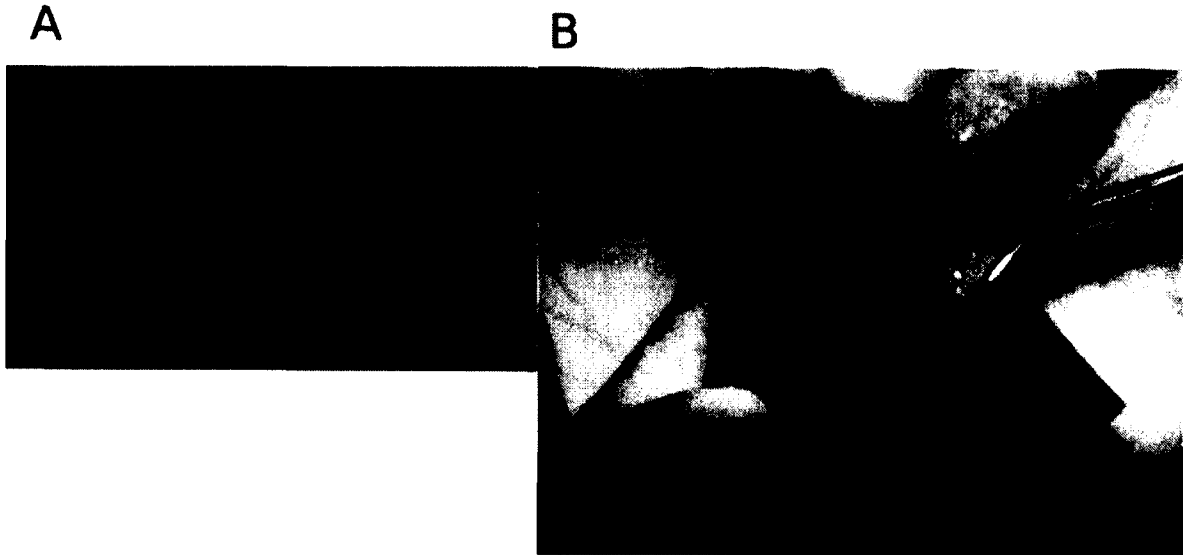


Figure 7. Proof of principle of line ablation with microsecond pulses. **A:** Shock applicator, with electrodes stretching along the insides of the caliper jaws. With a single application, a linear lesion can be created. **B:** Tissue with two linear lesions³⁵.

In another PEF approach, ring-shaped electrodes with shock durations in the *millisecond* range have been used to create lesions in the atrial ostia. While this method is very rapid and reaches

considerable tissue depth, it does not achieve complete transmural ablation (Figure 8)^{36, 37}.

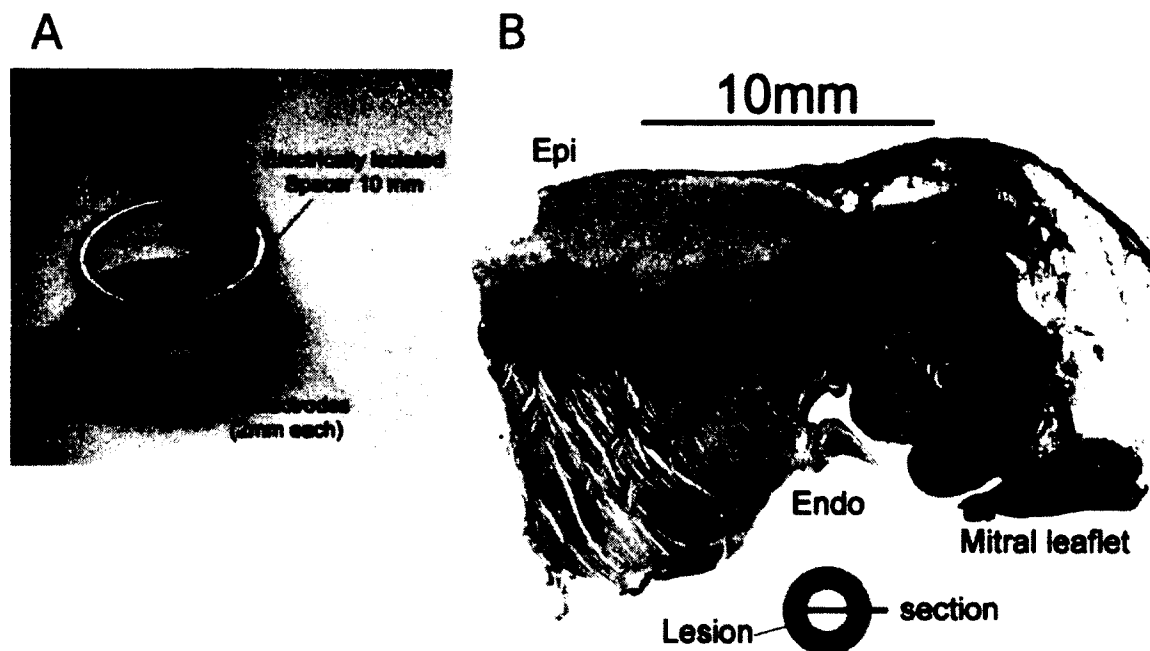


Figure 8. Millisecond shock ablation with ring-shaped electrodes. **A:** Shock application electrode. **B:** Histological elastic–van Gieson–stained section through the center of a circular lesion. Pink areas indicate ablated tissue. Note that the lesion is not transmural, because there is an isolated region in yellow showing surviving tissue that has not been ablated³⁷.

1.4 ADVANTAGES OF USING NSPEF ABLATION

Nanosecond PEF ablation has important advantages over longer shocks, particularly ablation uniformity. By ablation uniformity we mean how evenly all cells within the tissue are electroporated. It has been shown in modeling studies that the strong fields used for nanosecond pulses electroporate all cells indiscriminately, while the weaker fields associated with longer pulses lead to spatially heterogeneous, incomplete electroporation^{38, 39, 40, 41, 42}. While it would be in principle possible to generate pulses that are both strong and long, such pulses would deposit large energies, which would lead to unwanted thermal effects. Nanosecond pulses also have the benefit that it has already been shown that besides ablating cells via necrosis, they can also ablate them via apoptosis^{43, 44}. Such an additional ablation mechanism also increases the confidence that complete

ablation can be achieved. It is presently not known whether weaker, longer shocks can also induce apoptosis.

Ablation with nsPEFs may lead to a breakthrough in arrhythmia treatment in patients. By definition, nsPEFs are trains of electric shocks, each of a duration between 1 and 1,000 ns. We are considering short trains (1-20 shocks) with durations up to 350 ns and shock amplitudes up to 10 kV/cm. nsPEFs interact with cells either by electroporating the cell membrane or by electroporating membranes inside the cell^{45, 46, 47}. Both theoretical results³⁰ and the data we present here suggest that the nsPEF ablation volume can be controlled with better precision than in RF ablation. The basic reason for this better control is that electrical fields drop off much more sharply in the electrode configurations that we propose (see Figure 6. Panels B and D) than temperature does during RF ablation (where heat diffuses from the site of the catheter). Also, electrical fields cannot be transported away, while heat can be transported away by blood. The increased control that nsPEF ablation promises is vital to address the high recurrence rate of which RF ablation suffers. Lesions are most likely to become conductive at locations where they were not sufficiently wide to begin with; if nsPEF ablation can ensure a more uniform lesion thickness, recurrence would likely go down. Since electroporation can be induced rapidly, nsPEF ablation will likely require substantially less time than RF ablation; this would be a major improvement both for the individual patient and the ablation centers that could more easily satisfy the rising demand for this procedure.

To sum up, we expect the following advantages over conventional RF ablation are 1) Better control of the ablated volume; 2) lack of thermal side effects such as damage to neighboring tissue because the energies deposited in nsPEF ablation are too small to significantly heat tissue^{48, 49}; 3) acceleration of the ablation procedure, since both RF ablation and pulsed electric fields (PEFs) ablation create lesions segment by segment, but heating the tissue until it is destroyed takes more time than the application of electrical shocks; 4) different layers (epi- to endocardium) are exposed to identical shocks, so a high degree of translational symmetry in the ablated cross sections can be expected (this symmetry is limited by the heterogeneity of the cardiac tissue) compared with RF

ablation. In Chapter III, we demonstrate in experiments that nsPEF ablation really exhibits the expected advantages listed above.

1.5 NUMERICAL SIMULATIONS

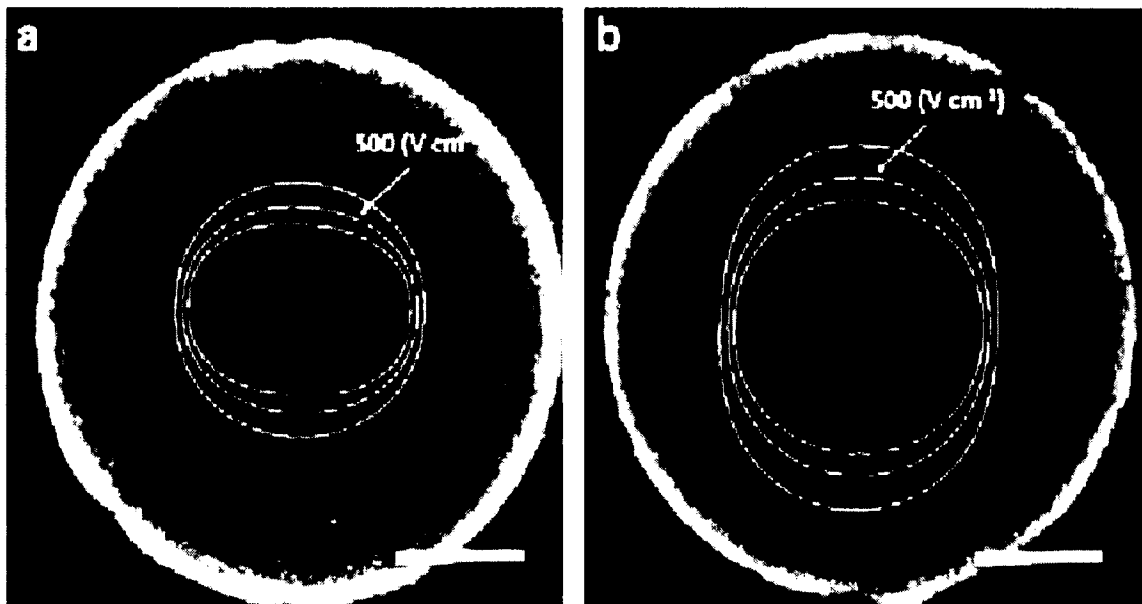


Figure 9: Overlay of electric-field contours predicted by the numerical model onto live/dead cells after 300 V (a) and 450 V (b) are applied through a pair of electrodes in the center. Live cells were stained green using Calcein AM and dead cells were stained red using propidium iodide (PI). Scale bars, 2.5 mm⁵¹.

Although IRE has great potential in the treatment of numerous diseases, its effects remain poorly characterized for many tissues. In order to ablate the targeted tissue with IRE, a numerical model can help to predict the ablated area with different pulse amplitude and electrode configuration (size, spacing, and number)⁵⁰. This numerical model can also be used to test different parameter sets for IRE treatment planning.

An example such a numerical model, for 3D tumors consisting of cancer cells cultured within hydrogels, indicates that tissue death can be accurately predicted by identifying the cells that are exposed to a critical electrical field threshold obtained from their numerical model (Figure 9)⁵¹. This model responds to external series of microsecond pulses in a manner analogous to that observed in

in vivo pathological systems. However, because the model is at cell level, features that are crucial for cardiac tissue, like its fiber structure and complex architecture, are not included.

On the tissue level, there are simulation analyses of irreversible electroporation of liver⁵² and brain⁵³ tissue (Figure 10) for tumor treatment, and of reversible electroporation of skeletal muscle tissue^{54,55} with anisotropic electrical conductivity for gene therapy (Figure 11).

The electric field distribution in cardiac tissue has not yet been studied. In Chapter IV, we developed a model that enhances the model described above by including anisotropic conduction and complex fiber geometry that are characteristic of cardiac tissue. We establish the critical field needed for ablation of cardiac tissue and simulate the ablation of human cardiac tissue. The results of our simulations suggest that the endo-epi configuration will be most useful for nsPEF ablation of human cardiac tissue.

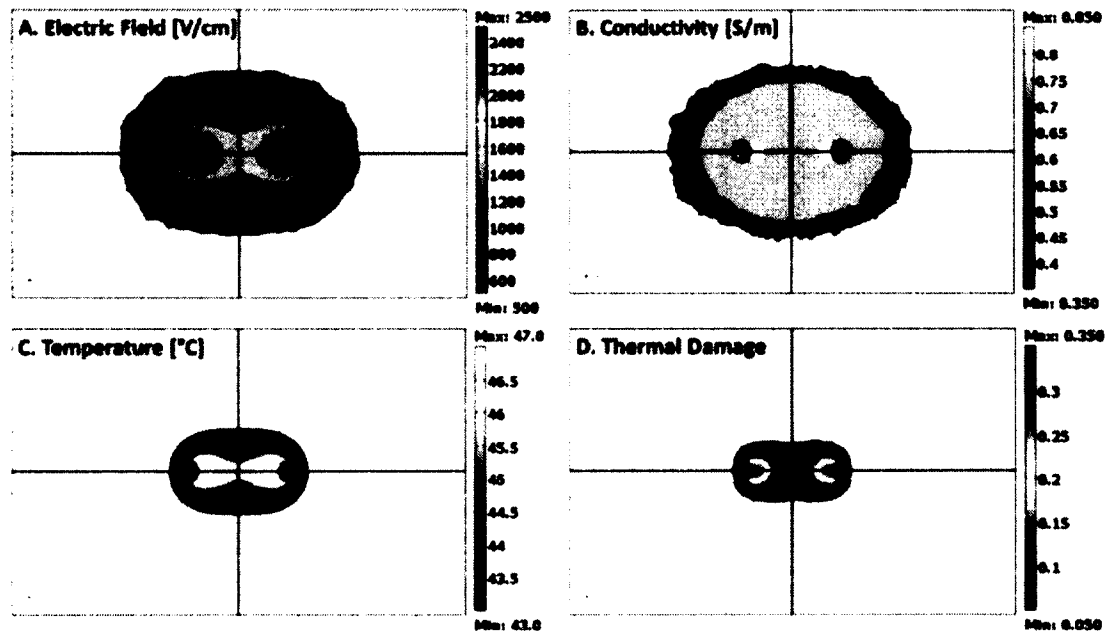


Figure 10. Electric field, conductivity, temperature and thermal damage distributions after an 80 s IRE treatment of tumor ablation in the brain⁵³.

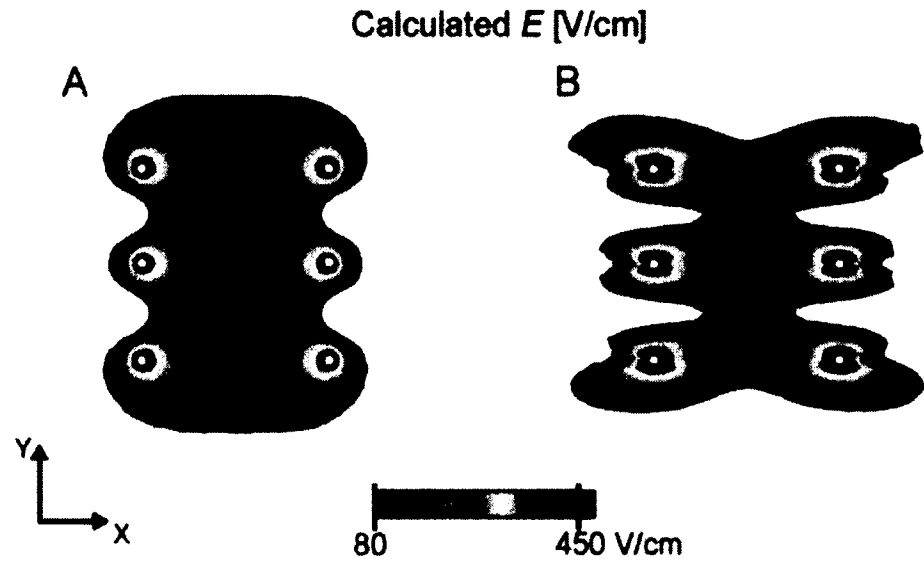


Figure 11. Electric field distribution for isotropic and anisotropic skeletal muscle conductivity. Electric field distribution for six needle electrodes (white circles) with A) isotropic tissue and B) anisotropic tissue properties⁵⁴.

CHAPTER II

METHODS

The evaluation of the proposed ablation techniques requires complex experimental designs, which involve interdisciplinary techniques from electrical engineering, computer programming, and cell biology. In this chapter we will discuss methods used both for experiments and our numerical model.

2.1 GENERAL APPROACH

We need to prepare isolated hearts to a state in which nsPEF ablation can be performed. Rabbits are anesthetized, and the hearts are extracted and Langendorff-perfused in our life-support system. In order to quantitatively analyze the performance of nsPEF ablation, we use our lab's optical mapping system to record the transmembrane potential of the heart at various sites and estimate the electrical status of the heart. The tissue is stained with special dye molecules which proportionally convert variations in transmembrane voltage signal into fluorescence, which allows the researcher to map the electrical activity of the isolated heart. The heart can be kept alive for several hours in the life support system. The nsPEF ablation shocks are delivered through a pair of electrodes, either by penetrating or endo-epi configurations. Data post-processing is performed using customized software to obtain different maps to quantitatively assess the effects of ablation. In order to understand the effects of the ablation transmurally from epi- to endocardium, fluorescent dyes which mark live or dead cells are used, and the ablated cardiac tissue is sectioned, to reconstruct the 3D geometry of the ablated volume.

2.1.1 ANIMAL SURGERY

During rabbit surgeries, we use procedures designed to limit animal discomfort, stress, pain, and injury. All procedures are approved by the Old Dominion University Institutional Animal Care and Use Committees (IACUC). Before surgery, the rabbits are heparinized (500 i.u, i.v.) and anesthetized with isoflurane (3-5%) in oxygen via a mask. A toe pinch is used to ensure that the animal is deeply anesthetized before starting the procedure. Once a surgical plane of anesthesia is achieved, a midline sternotomy is performed, and the heart is immediately extracted and placed in cold (4°C) cardioplegic solution. This is done as quickly as possible to guarantee that the heart does not suffer from a lack of perfusion more than necessary. Removal of the heart takes approximately 5 minutes.

2.1.2 LANGENDORFF-PERFUSED HEART IN THE LIFE-SUPPORT SYSTEM

The Langendorff-perfused rabbit heart is one of the most studied models of human heart physiology and pathophysiology. Many types of arrhythmias observed clinically can be reproduced in the rabbit heart model⁵⁶. A general principle of the method is to deliver oxygenated (95% O₂ and 5% CO₂) blood substitute, Tyrode's solution into the removed heart of an animal through a cannula inserted and fixed in the ascending aorta. Since the aortic valve is closed, the perfusion fluid cannot enter the left ventricle; rather, it is forced into the coronary vessels, which supply the heart tissue with blood. As a consequence, the entire perfusate enters the coronary arteries via the ostia at the aortic root. After passing through the coronary circulation, the perfusate drains into the right atrium via the coronary sinus. The perfusion pressure during the experiment is kept constant by adjusting the perfusion rate. Langendorff-perfusion delivers nutrients and oxygen to the cardiac muscle at a controlled temperature, allowing the heart to continue beating for several hours after its removal from the animal. The schematic diagram of a Langendorff-perfused heart in the life support system

is shown in Figure 12. By adjusting the oxygen rate, pH of the heart chamber can be maintained at 7.35 ± 0.05 .

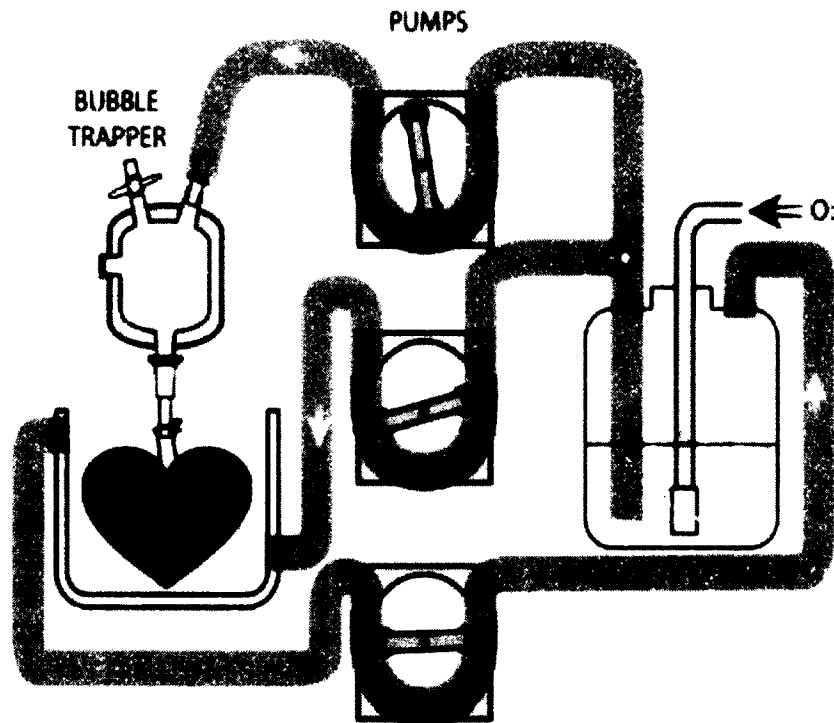


Figure 12. Langendorff-perfused heart in our life support system⁹³. By supplying oxygenated blood substitute (called Tyrode's solution) into the heart at constant rate, the heart can be kept alive for several hours with normal electrophysiological activity. The top pump is for delivering Tyrode's solution into the heart; the middle one is used to guarantee a constant temperature environment, and the bottom one is for recycling the Tyrode's solution.

In order to sustain the electrophysiological activities of the Langendorff-perfused hearts, Tyrode's solution is perfused to provide basic nutrients to the myocardium through the vessels called coronary arteries around the heart. Tyrode's solution contains 5.128 mM (mol/L) of NaCl, 0.8 mM of NaHCO_3 , 0.048 mM of NaH_2PO_4 , 0.042 mM of MgCl_2 , 0.188 mM of KCl, 0.052mM of CaCl_2 , 2 g/L of glucose.

2.1.3 OPTICAL MAPPING SYSTEM

An optical mapping system consists of three major components: 1) the heart preparation, which is an isolated Langendorff-perfused rabbit heart stained with a voltage-sensitive dye; 2) the illumination system, which is to excite voltage-sensitive dye of the heart; 3) a CCD camera which measures the fluorescent light. A schematic diagram of the optical mapping system is shown in Figure 13.

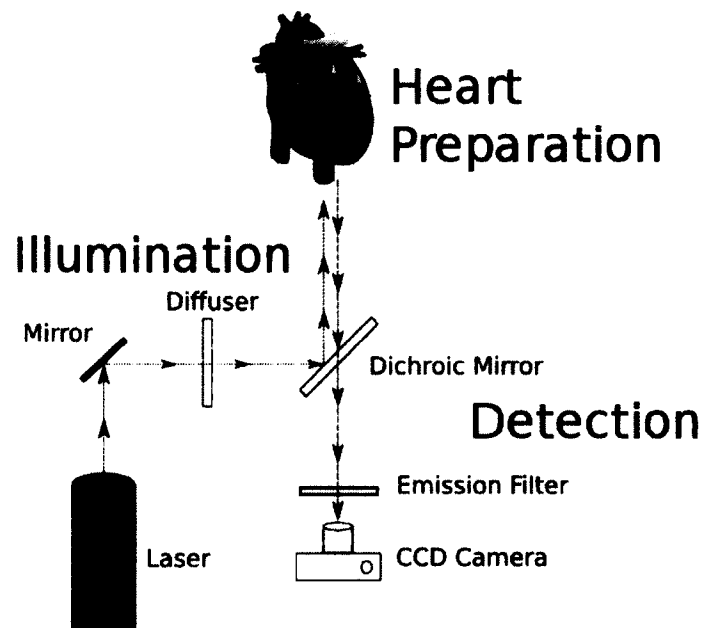


Figure 13. Typical optical mapping system consisting of three major components: 1) the heart preparation; 2) illumination; and 3) a detector. A laser is used excite fluorescent dye in the heart through a dichroic mirror, which selectively reflects light of excitation wavelength and directs it toward the heart. In response to excitation light, voltage-sensitive dye molecules bound to the heart cells fluoresce light in proportion to the transmembrane potential of the bound cells. Light emitted from the dye has a longer wavelength, and therefore passes through the dichroic mirror, undergoes a final stage of filtering, and is focused onto the detector.

In our experiments, Langendorff-perfused hearts will be loaded with the voltage-sensitive fluorescent dye Di-4-ANBDQBS (JPW-6033) and the electro-mechanical uncoupler 2,3-BUTANEDIONE MONOXIME (BDM). The purpose of adding BDM into Tyrode's solution is to

suppress motion artifacts in the optical signals caused by muscle contraction. The stock solution of JPW-6033 was prepared by dissolving 10 mg, 570.73 g/mol JPW-6033 powder into 1.2 ml of ethanol to make the concentration of 8.33 mg/ml. For each experiment, 30 μ L of the stock solution was mixed with 15 mL of Tyrode's solution, and then injected through a connector into the cannula to be perfused into the heart with normal Tyrode's solution.

To prepare the BDM stock solution, 5.05 g of BDM was dissolved into 250 ml of Tyrode's solution to make 0.2 M (0.2 mol/liter) of the solution. For each experiment, if there is a total of 2 liters of Tyrode's solution (tubing+chamber+erlenmeyer flask) in the life-support system, we added 110 ml BDM stock solution into 2 liters of the Tyrode's solution to make the final concentration 11mM of BDM.

The heart is illuminated with a 671 nm laser light (the red DPSS laser we use is SDL-671-1000T, Shanghai Dream Laser Technology Co, China) and fluorescent light (>715 nm) is recorded with a CCD camera (Little Joe, SciMeasure).

2.1.4 MECHANISM OF VOLTAGE-SENSITIVITY

The optical mapping system uses voltage-sensitive dyes which have high affinity to the cell membranes (Figure 14). While bound to the cardiac cell membrane, if the dye molecules absorb photons of a certain wavelength, they are excited to a higher energy state. As the molecules return to the ground state, photons of a longer wavelength are emitted (fluorescence). During the excitation process, a charge in the dye molecule moves from one molecule to the other. If there is a change of transmembrane potential, say depolarization happens, more positive charges are present at the outer membrane and more negative charges at the inner membrane, making the physical movement of charges of dye molecule easier or harder (Panel A). Consequently, the energy required (or fluorescence energy emitted) changes compared to the energy required before the depolarization happened. That is why there is a shift of the emission/absorption spectrum in Panel B. As the

spectrum indicates, the change of light intensity ΔF is proportional to the transmembrane potential, and with a chosen filter (highlighted in the green square), this change in fluorescence light can be visualized. Therefore, the dye molecules transduce the voltage signal into light. This allows one to precisely evaluate the propagation of a wave of excitation visually.

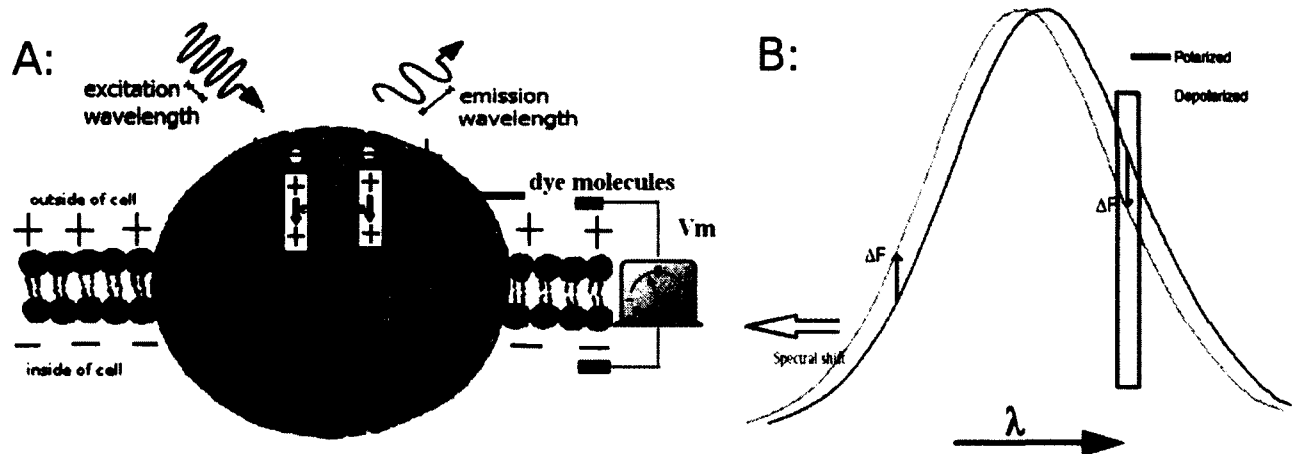


Figure 14. Mechanism of voltage-sensitive dye. **A:** Schematic representation of voltage-sensitive dye molecules (inside the dotted blue circle) bound to the cardiac cell membrane. **B:** The emission (or absorption) spectrum is shifted to shorter wavelength as the cardiac cell is depolarized. Depolarization produces a decrease in fluorescence at the red wing of the spectrum and an increase when fluorescence is monitored on the blue wing of the spectrum (squared in green for our experimental setup). The magnitude of the spectral shift will be linearly related to the change in potential.

2.1.5 PI / TTC STAINING AND SECTIONING

Propidium Iodide (PI) is a membrane impermeant fluorescent molecule and is generally excluded from viable cells. PI is commonly used for identifying dead cells in a population and as a counterstain to the dead cells by binding their DNA⁵⁸. We stained the tissue with propidium iodide (PI, 30 $\mu\text{mol/l}$ Tyrode), using our coronary perfusion, for 30 minutes, and then washed it out for another 40 minutes, leaving the dead cells with a compromised membrane stained with PI.

To measure PI fluorescence, we used a setup similar to our optical mapping setup: 1) laser light (532 nm) to excite the PI molecules, 2) a dichroic mirror to reflect the laser light onto the PI stained tissue and to allow excited fluorescent light to pass through, 3) a diffuser to widen the scope of laser

light so a larger area of the PI tissue can be illuminated, 4) a filter to pass fluorescent light from PI staining, and 5) a camera to record images.

In order to better analyze the dead/live tissue after nsPEF ablation, we later added 2,3,5-triphenyltetrazolium chloride (TTC) staining to our project. We became aware of the high resolution of live/dead assessments with TTC staining later in our project. Since this resolution was not as we wanted it with PI stains, we switched to TTC stains.

TTC has been used successfully for early histochemical diagnosis of myocardial infarction^{59, 60}. The staining action of tetrazolium salts is based on the presence of the enzyme called dehydrogenase^{61, 62}. Tissue with normal levels of the enzyme is stained red, whereas infarcted or ablated tissue remains unstained owing to loss of the enzyme. The TTC staining solution was prepared with TTC powder (5 g) mixed with 500 ml of normal saline (0.90% w/v of NaCl). After Tyrode's solution was removed from our life-support system, the heart was perfused using the TTC solution for 20 minutes in a dark environment. Then the heart was removed from the life-support system, and fixed in 10% neutral buffered formalin for future sectioning and histological analysis.

In order to histologically analyze and identify the ablated tissue transmurally from epicardium to endocardium, we cut the ablated tissue and mounted it into a mold filled with melted agarose gel at a temperature between 40-45°. When the temperature drops to the room temperature, agarose becomes solid like rubber and embeds the piece of tissue. This helps for sectioning as the surrounding agarose provides enough mechanical support. Then the embedded tissue is glued onto the platform of the vibratome (Lancer®, series 1000). By adjusting the horizontal height and angle of a vibrating razor blade, a different thickness of sectioned tissue can be obtained. In our experiment, we normally set each sectioned tissue to be 200-300 µm thick, the best compromise we found between quality (which increases with section thickness) and quantity (which decreases with section thickness).

2.2 NANOSECOND PULSE GENERATION WITH PULSE FORMING LINES

Our nanosecond ablation requires the delivery of nanosecond, high voltage pulses to cardiac tissue. A preferred method of generating short rectangular pulses with excellent accuracy is using a pulsed forming line (PFL).

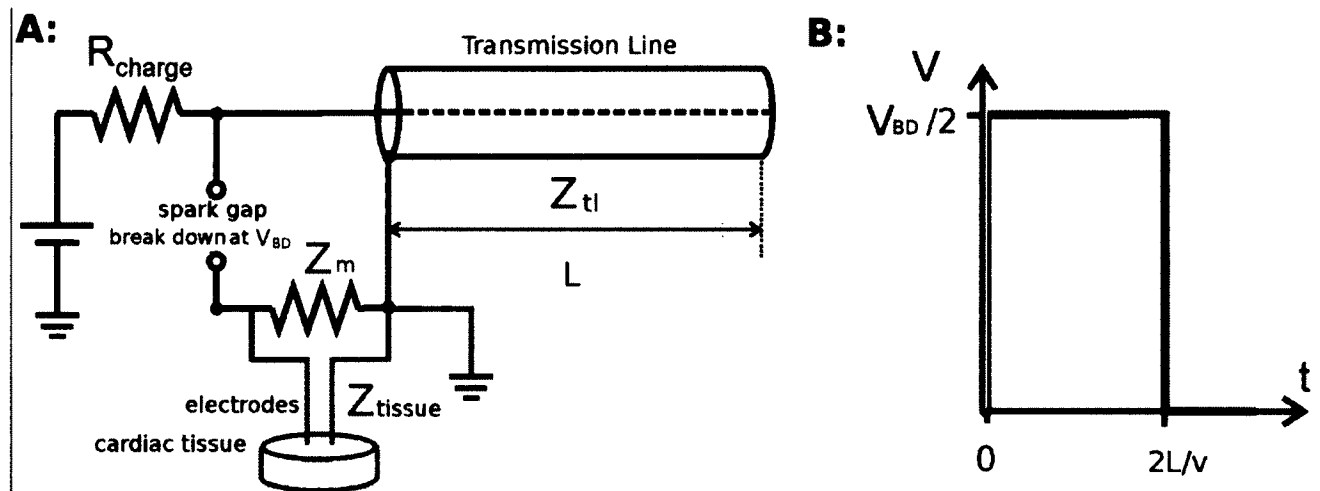


Figure 15. Schematic diagram of the pulser (A) and the ideal rectangular pulse it produces (B).

Figure 15 shows a schematic diagram of the pulser we used and the corresponding ideal pulse shape.

The circuit includes a high voltage DC power supply, a charging resistor R_{charge} to limit the charging current, a transmission line that acts as a capacitor, and an adjustable spark gap between the charging resistor and the testing resistor Z_m . Once the transmission line (with the length of L) has been charged to the breakdown voltage V_{BD} , the spark gap becomes conductive, and the line is allowed to discharge into the load (a matching resistor parallel with the tissue).

The voltage on the load V_1 is determined by the impedance of the load Z_1 (matching resistor Z_m parallel with the impedance of the cardiac tissue Z_{tissue}) and the impedance of the transmission line (Z_{tl}):

In the case where the impedances of the transmission line and the load are equal, then clearly the voltage on the load V_l will be $V_{BD}/2$.

Thus, by changing the width of the spark gap, we can adjust the breakdown voltage V_{BD} , which will finally determine the amplitude of our rectangular pulse on the cardiac tissue (the amplitude will be $V_{BD}/2$).

Because the stored energy source for the pulse is a transmission line, the load experiences a rectangular voltage pulse whose duration is equal to twice the time an electromagnetic wave takes to travel through the line:

$$t = \frac{2L}{v_p} \quad 63$$

$$v_p = \frac{c}{\sqrt{\epsilon_r}} \quad 63$$

where c is the velocity of light in vacuum and ϵ_r is the relative permittivity of the dielectric material which insulates the transmission line.

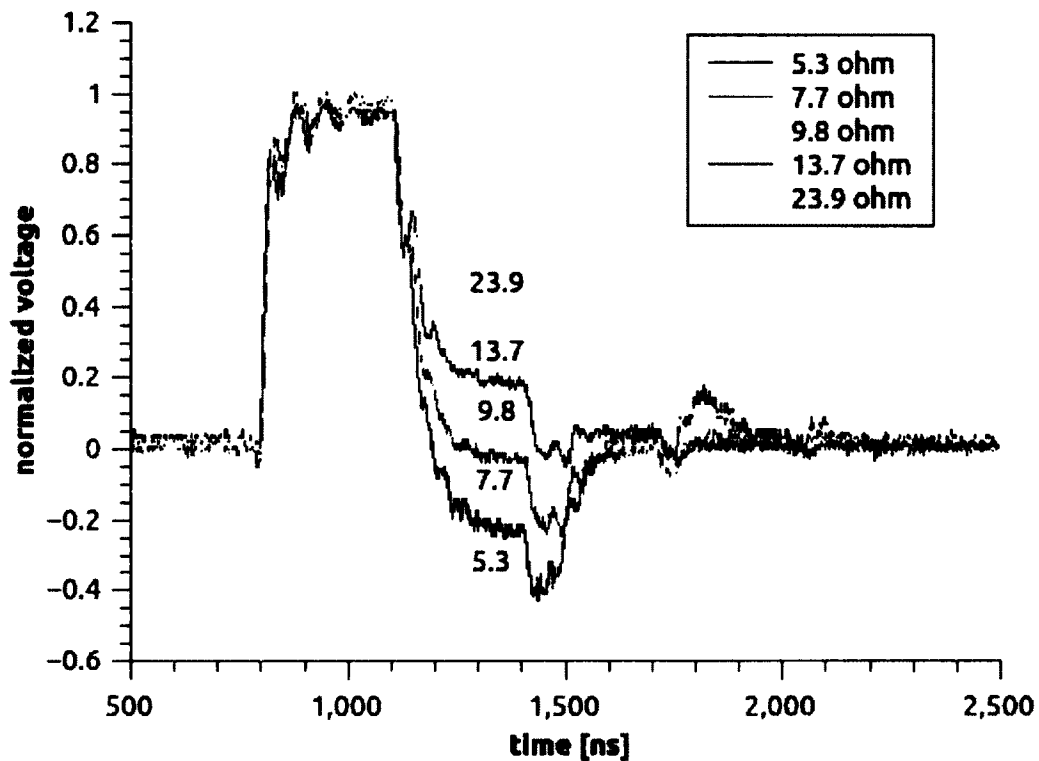


Figure 16. Comparison of matching resistance using different resistors. We chose $Z_m=13.7 \Omega$ because the corresponding pulse exhibits almost no negative peaks and good rectangular shape.

In our experiment, we use a RG-58 coaxial cable as the transmission line with a relative permittivity of $\sqrt{\epsilon_r} = 1.5$. Since we want to generate 350 ns pulses, we used a coaxial of length $L = 350 \text{ ns} \times 3 \times 10^8 \text{ m/s} \times (2 \times 1.5) = 35 \text{ m}$. A high voltage probe (P6015A, Tektronix) as well as a high sampling rate oscilloscope is utilized for the measurement of the produced pulses. In order to generate a nearly square pulse, the matching resistor of impedance Z_m needed to be adjusted such that the resistance of the coaxial cable ($\sim 10 \Omega$) matches the total load impedance (Z_m parallel with Z_{tissue}). In general, too small loads result in more negative peaks on the tail, while too large loads results in more positive peaks on the tail⁶⁴.

To find a good matching Z_m , we tested five different matching resistors ranging from 5.3 Ω to 23.9 Ω . We find that for $Z_m > 9.8$ there will be more positive peaks on the tail and that for $Z_m \leq 5.3$, more negative peaks appears on the tail. For $Z_m = 13.7 \Omega$, on the other hand, no negative peaks appear, and the pulse is close to rectangular. Consequently, we chose $Z_m = 13.7 \Omega$ for our experimental setup (see Figure 16).

2.3 STIMULATOR, TEMPERATURE SENSOR AND PRESSURE SENSOR

Stimulator

A stimulator functions as a pacemaker that can be selectively placed on specific locations of the heart's surface. We place the stimulus electrode (black) on the heart surface (see center of Figure 17), while the ground electrode is immersed into the heart chamber filled with Tyrode's solution (shown as a metal wire on the top left of Figure 17). The purpose of pacing the heart is that one can selectively initiate the occurrence of an action potential and then use nsPEF ablation to block the pathway of its propagation. In such a way it is very helpful to visualize the effect of nsPEF ablation. The stimulator we used is a Grass S5 model SM5E medical stimulator. It can continuously provide square waves with different parameters. The amplitude of the stimulation for our experiment is between 8-15 V, 5-10 milliseconds duration, and 3-4 Hz.

Temperature stabilization

Temperature sensors are used to continuously monitor the temperature in different locations in our system in real time. One sensor is immersed into the heart chamber, and another one is inserted into the tubing which perfuses the aorta. As the schematic diagram in Figure 12 shows that two pumps control the flow rate of Tyrode's solution into the aorta and the heart chamber, respectively. There are also two heating coils (which are not shown in Figure 12) mounted with the perfusion tubing and the heart chamber tubing (the top and middle tubing in Figure 12), each connected to a water bath. In this way, the temperature of the solution entering the heart and the solution in the chamber can be adjusted by setting suitable temperatures of both water baths. By adjusting the flow rate of both pumps and water baths, both the temperature in heart chamber and in the aorta are maintained at 37 ± 0.5 °C for the rabbit heart. The temperature sensor we used for our experimental setup is an insulated thermocouple element (<http://www.tcdirect.com>). Temperature values are converted to electric signals by using a dual transmitter (TXDIN70 model, Omega) and displayed on a LED screen. After the temperature signal has been converted by the dual transmitter, electric signals are also acquired and recorded into the computer by the signal acquisition board (BNC 2110, National Instruments, Inc), and displayed onto a customized control QT graphical user interface (GUI) on the computer screen, for better monitoring.

Pressure stabilization

A pressure transducer (TD1000, Transducer Direct, Inc) is mounted with a “T” connector to the cannula tubing in order to monitor the pressure of the aorta in real time. By adjusting the flow rate of the perfusion pump, the aortic pressure was maintained at 60 ± 5 mmHg⁵⁷. Like the temperature sensor, the pressure sensor is also connected to the acquisition board, so its value is displayed onto the customized control QT graphical user interface (GUI) on the computer screen.



Figure 17. Stimulator (shown as a straight black insulated metal wire) placed onto the surface of Langendorff-perfused rabbit heart.

2.4 GUI CONTROLLING PANEL

In order to acquire the action potential movies of the heart and post-processing data, we used C++ and Qt to design a graphical user interface (GUI) which allows users to acquire, load and save movies, control the CCD camera, and post-process the movie to obtain different functional maps, such as the amplitude map and activation map (Figure 18). The most important features of this GUI are discussed below.

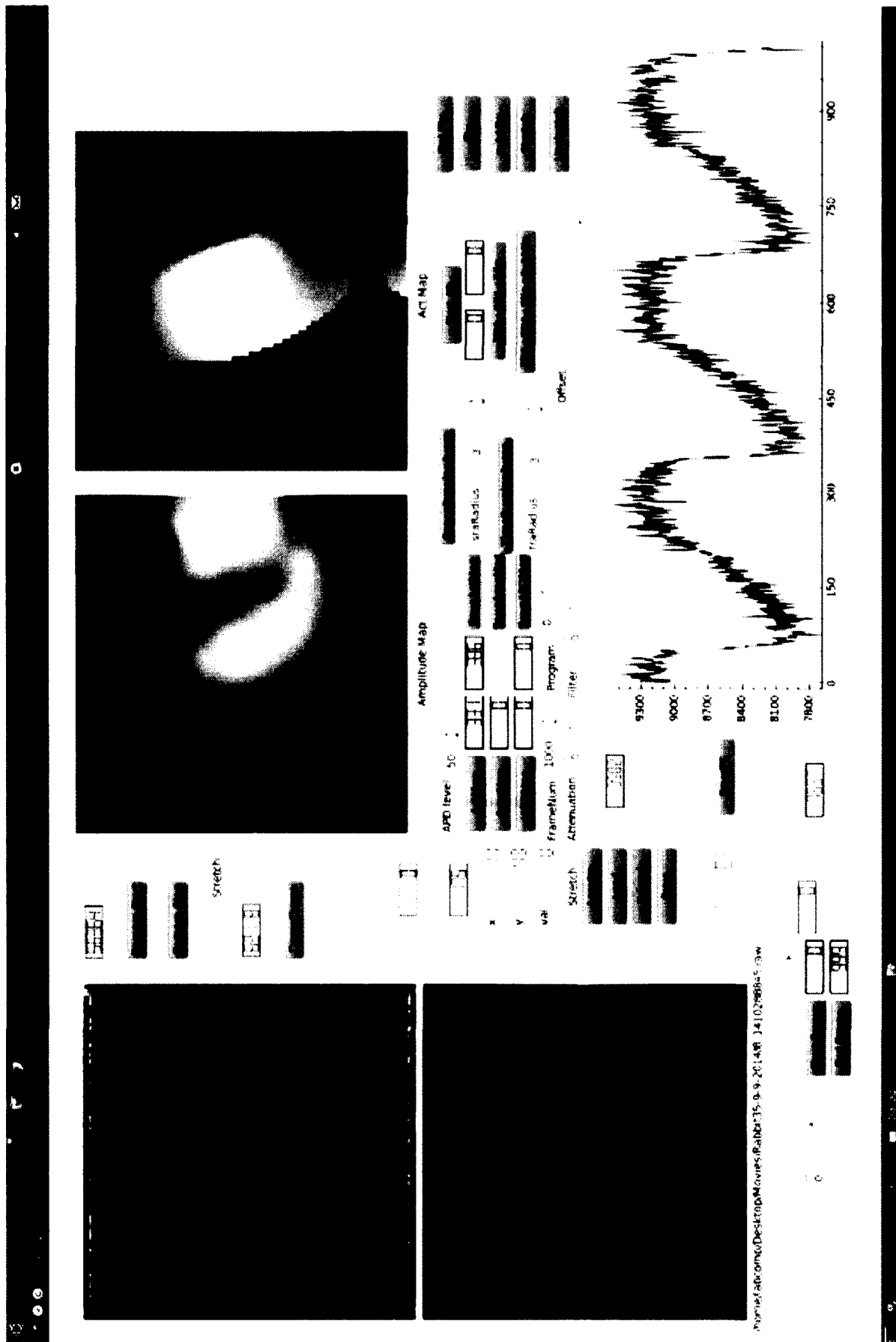


Figure 18. Screen shot of GUI for data control and processing.

Movie Acquisition

A charge-coupled device (CCD) camera (Little Joe, SciMeasure) in our lab is used to record optical mapping movies from the rabbit heart. The advantage of Little Joe is that it provides digital video at high frame rates and high light sensitivity. Its intended user is a scientist, such as an astronomer or biological researcher [The “Little Joe” Digital Camera: Technical Manual and Users’ Guide]. Another advantage of this CCD camera is that several features like attenuation, frame rate, image size, binning, and offset, can be programmed using camera commands, because many of Little Joe’s modules contain programmable logic devices. Depending on the required movie, there is a balance between frame rate and the resolution of the movie. Generally speaking, higher recording speed will reduce the resolution of the movie and vice versa (see Table 2 where the unit for image size is pixel, and 2x2 binning refers to the combination of two pixels into one, for instance). Other features like background level, filtering, and attenuation of recorded images can be adjusted.

To better control the camera, we programmed an interface for communication with the camera through our QT C++ platform that allows us to adjust all camera features that are important to us. Figure 19 illustrates an example of capturing images by selecting different programmed features. By adjusting different programs, attenuation, filtering and offset settings, a different frame rate of recording the movie can be realized, with different contrast, background noise, and gain.

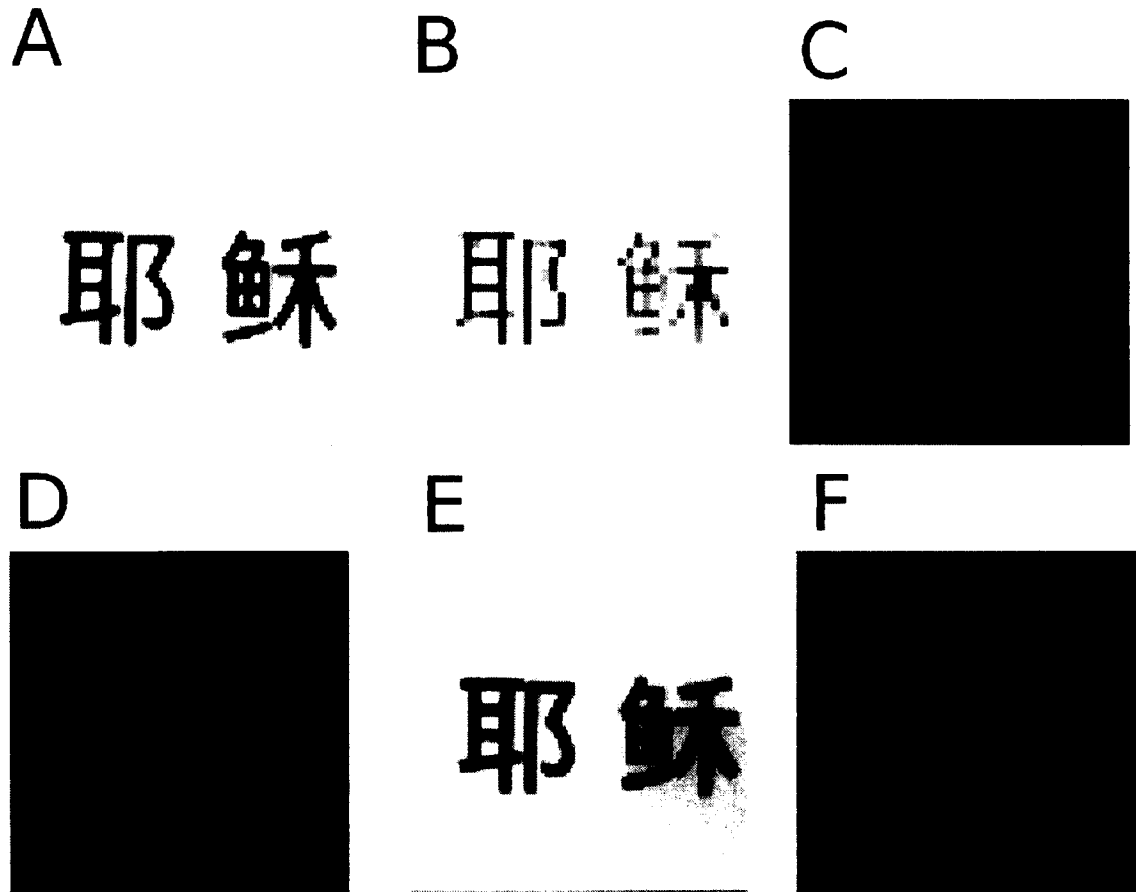


Figure 19. Chinese characters captured by the camera “Little Joe” with programmed features. **A:** 1000 Frame/sec, with 1x1 binning (program 1, attenuation set to be zero, filter zero, offset zero). In Table 2, eight programs with different frame rate, image size and binning are listed **B:** 3000 Frame/sec, with 2x2 binning (program 5, attenuation set to be zero, filter zero, offset zero). **C:** 2000 Frame/sec, with 2x2 binning (program 7, attenuation set to be zero, filter zero, offset zero). **D:** Attenuation (refers to as gain or amplification) set to be 1 (program 0, filter zero, offset zero). **E:** Filter (pertain to filtering the signal frequency response) set to be 1 (program 0, attenuation zero, offset zero). **F:** Offset (black level) set to be 800 (program 0, attenuation zero, filter zero).

Program	Nominal Frame Rate (Hz)	Image size	Binning
0	1000	80 x 80	1 x 1
1	625	80 x 80	1 x 1
2	125	80 x 80	1 x 1
3	40	80 x 80	1 x 1
4	2000	40 x 40	2 x 2
5	3000	40 x 40	2 x 2
6	5000	26 x 26	3 x 3
7	2000	80 x 80	2 x 2

Table 2. List of built-in programs of Little Joe.

By selecting different programs of the CCD camera, we can record different movies with different requirements. For example, if we want to record the movies faster with lower resolution, we can choose program 7. If we want the higher image resolution and the fastest speed, one can choose program 0 (this program is the most common choice for our ablation project). By adjusting other features such as offset, filtering and attenuation, one can achieve the best quality of signals required.

Signal processing

Raw movies acquired by the CCD camera, including background white noise and camera noise, can be linearly filtered with spatial and temporal filtering to have higher SNR. The schematic diagram in Figure 20 depicts the algorithm of both kinds of filtering.

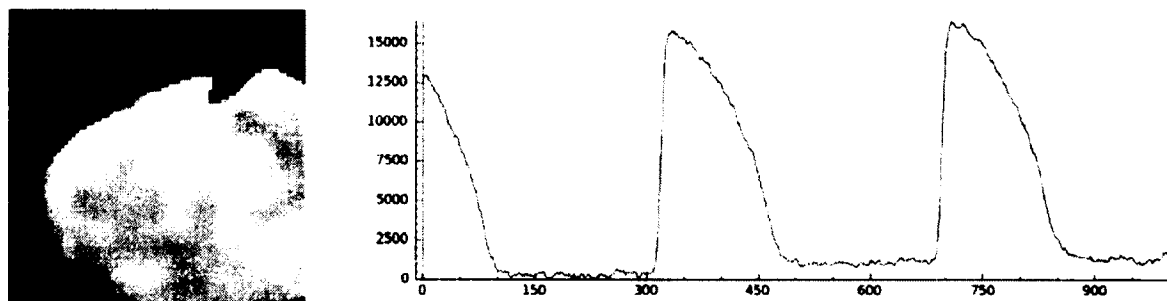


Figure 21. Post-processed signal after spatial and temporal averaging, flipping, subtracting the minimum and stretching. **Left:** One frame of the post-processed movie. **Right:** Post-processed action potentials obtained from a random location of the heart.

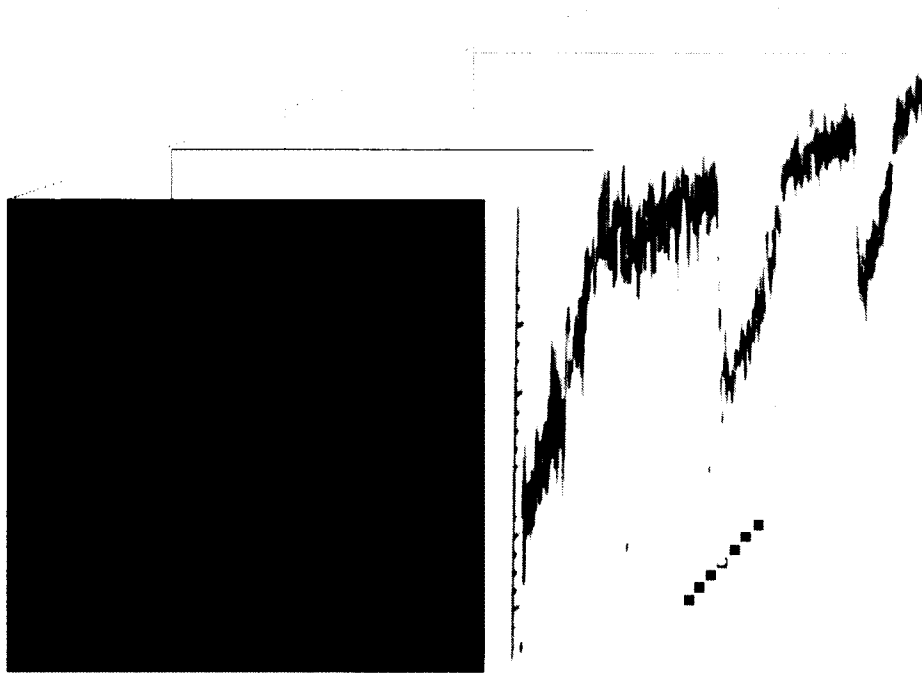


Figure 20. Space running average filtering and time running average filtering. Green marked spot in the movie picture shows the location of action potential signal, and the surrounding red spots show the averaged area in space (in this case 3x3); For time averaging, signal amplitude of each frame is averaged with its neighbors (typically within 3 frames).

Due to our normal camera setting for action potentials recording, the recorded 80x80 pixel movie contains 1,000 frames lasting 1 second. In Figure 20, the action potentials of a selected pixel (marked green) are shown for illustration. In order to have smooth action potentials, a spatial running average filter and a temporal running average filter are applied. After flipping, subtracting the minimum amplitude of the light intensity and stretching the signal, we obtained the post-processed signal shown in Figure 21.

Activation map

An activation map illustrates the activation sequence in cardiac tissue. This helps one to understand the dynamics of cardiac activation.

The algorithm for determining the activation map is the following: first, the user manually selects a range of frames that contains an activation. For example, in Figure 21 we can either choose a

range of roughly frame 250 to frame 500 or from frame 600 to frame 800. This allows us to specifically choose the action potential we want to analyze. Then, the threshold of the depolarization needs to be determined. Usually it has been assumed to be half of the depolarization amplitude. In the example of Figure 21, 7500 will be the threshold. Having gotten the threshold for each pixel in the movie, the next step is to determine the time (or the frame number) corresponding to the threshold of depolarization. To find such an activation frame, we need to compare each voltage for the individual pixel with the threshold we just identified. If one voltage happens to be bigger than the threshold and also satisfy that its previous voltage is smaller than the threshold, then this frame is identified as the activation frame. After the frame of activation has been determined for all the pixels of the heart, frame numbers are converted into times and displayed color-coded; the resulting map is called the activation map.

Amplitude map

An amplitude map describes the amplitude of the action potential for each pixel of the heart. The brighter the area, the higher the action potential amplitude of such an area. The algorithm of determining the amplitude map is straightforward: find the difference between the maximum and minimum voltage of each pixel, and run the loop of searching for all the pixels of the heart.

2.5 ELECTRODE CONFIGURATIONS

To deliver the pulses, a pair of customized electrodes are penetrated into the heart and shocks are applied, in order to make a transmural and complete dead region between electrodes.

The electrodes need to be conductive and thin, for easy insertion and to limit tissue damage. We chose tungsten as our electrode material, inserted into a insulating material (red color in Figure 22). The uninsulated part of the electrode is 4 mm long to guarantee the full penetration of 4 mm through the ventricle wall. Electrode diameters are only 250 μm for easy penetration. We tested a

variety of inter-electrode distances and found that $d \geq 4$ mm leads to ablated volumes that are too wide (the desired range is ~ 3 -5.5 mm). In particular, $d \geq 4$ mm regularly led to an ablation geometry that was more than 6 mm wide, which is too wide to create a normal lesion (see Figure 41 below). We finally adopted $d=2$ mm as our standard electrode distance; that produced ablated volumes with a width of ~ 3 mm. Figure 23 shows the penetrated heart with electrodes.

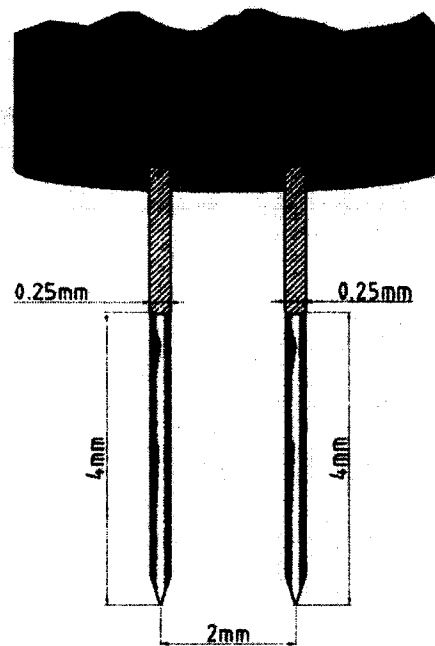


Figure 22. Penetrating electrodes design.



Figure 23. Penetrating electrodes in a rabbit heart. The tips of electrodes were dipped into surgical ink, so the sites of penetrated tissue would be marked with two dark dots. This ink stains tissue permanently, it is not washed away in the Tyrode's solution or in formalin.

Besides the penetrating electrodes configuration that we have tested so far, there are two other configurations we plan to test for nanosecond pulsed electric field ablation. Figures 24 and 25 show the designs of the electrodes for endo-endo and endo-epi configuration. We chose stainless steel nails as the contact material because stainless steel is non-reactive and non-toxic and the nails have a nicely sized circular contact surface of 6 mm diameter. For the endo-endo configuration, we spaced the electrodes 2 mm apart (so that there is a 2 mm gap between the contact areas).

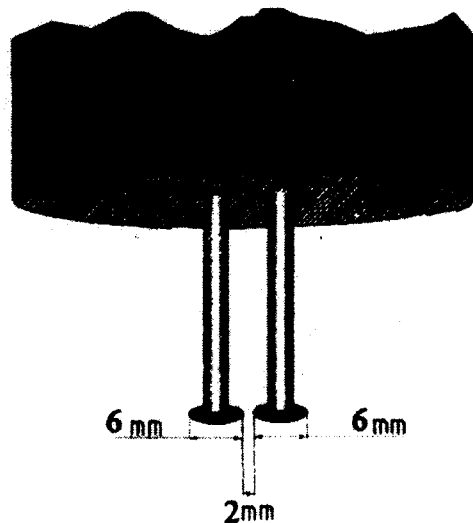


Figure 24. Electrode design for the endo-endo configuration.

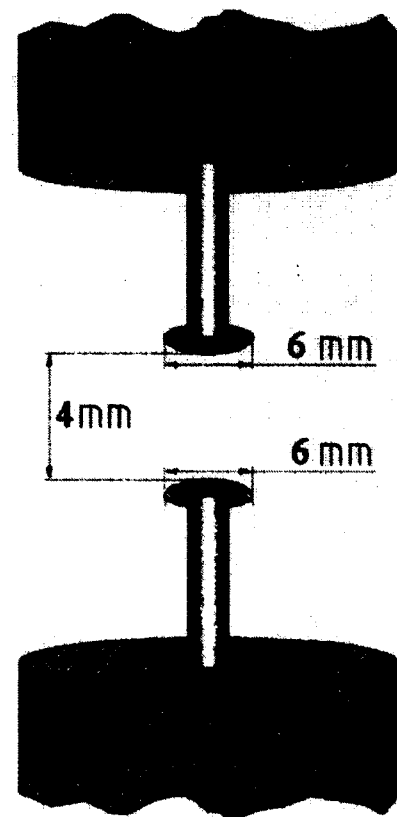


Figure 25. Electrode design for the endo-epi configuration.

The endo-epi configuration (in Figure 25) has one electrode touching the endocardium and the other the epicardium; it does not require tissue penetration, and existing catheters can be used with minimal modifications. On the downside, this configuration is the only one that will require two catheters (one endocardial and one endo-thoracic). Again, the electrodes do not need to penetrate tissue, and we chose the circular contact area of diameter 6 mm (see Figure 25) which should lead to ablated volumes with a width of 4-6 mm.

For both endo-epi and endo-endo configurations, we need to isolate a free wall of either the right or left ventricle, stretch it onto a frame, and immerse it into Tyrode's solution. Unlike the Langendorff-perfused heart preparation in which a cannula is inserted into the aorta, the stretched preparation is reserved with the free wall of the right/left ventricle and a cannula is inserted into the

coronary artery for the Tyrodes' perfusion (see Figure 26). Due to the limitation of the number of rabbits, we only did one experiment of endo-epi ablation (Figure 27). Because the surface of the heart for ablation is not big, only two ablation applications were conducted.

2.6 MATHEMATICAL MODEL OF NSPEF ABLATION

The basic assumption of our model is that there is a critical electric field amplitude which leads to the death of cardiac tissue (and fields with even higher amplitude also do). In order for such a model to accurately predict ablated volumes, it has to incorporate the physical properties of cardiac tissue that determine the local electric field distribution. Also, the critical electric field amplitude has to be determined. To have such an accurate numerical model, the following criteria need to be considered for the numerical simulation:

- 1) The electric field distribution depends on electric conductivities, and in the heart, local conductivities depend on the cardiac fiber orientations⁶⁵. Therefore, our model needs to include information regarding the different fiber orientations in different cardiac layers.
- 2) By superimposing the dead area determined in an experiment and the corresponding electric field distribution map computed with a model, the critical field amplitude that leads to ablation can be determined.
- 3) Electric fields lead to currents that heat the tissue via Joule heating. This can lead to adverse thermal side effects, so it is desirable to include the temperature distribution in the tissue into the model to assess the importance of heating. Increased temperature also affects the conductivity of tissue and therefore the electric field distribution.
- 4) Once both conditions are satisfied (i.e. no thermal side effects and threshold of the electric field is determined), the model can be used to predict the field distributions for different pulse amplitudes and electrode configurations. These predictions can then be compared to experimental results.



Figure 26. Heart preparation for endo-epi experiment. The left ventricle of the rabbit heart is stretched and a cannula is inserted into coronary artery for perfusion with Tyrode's solution. The preparation is retrogradely perfused through the aorta (as in Langendorff perfusion). The CCD camera is located to face the epicardial wall to record the action potentials when the heart is illuminated by laser light.

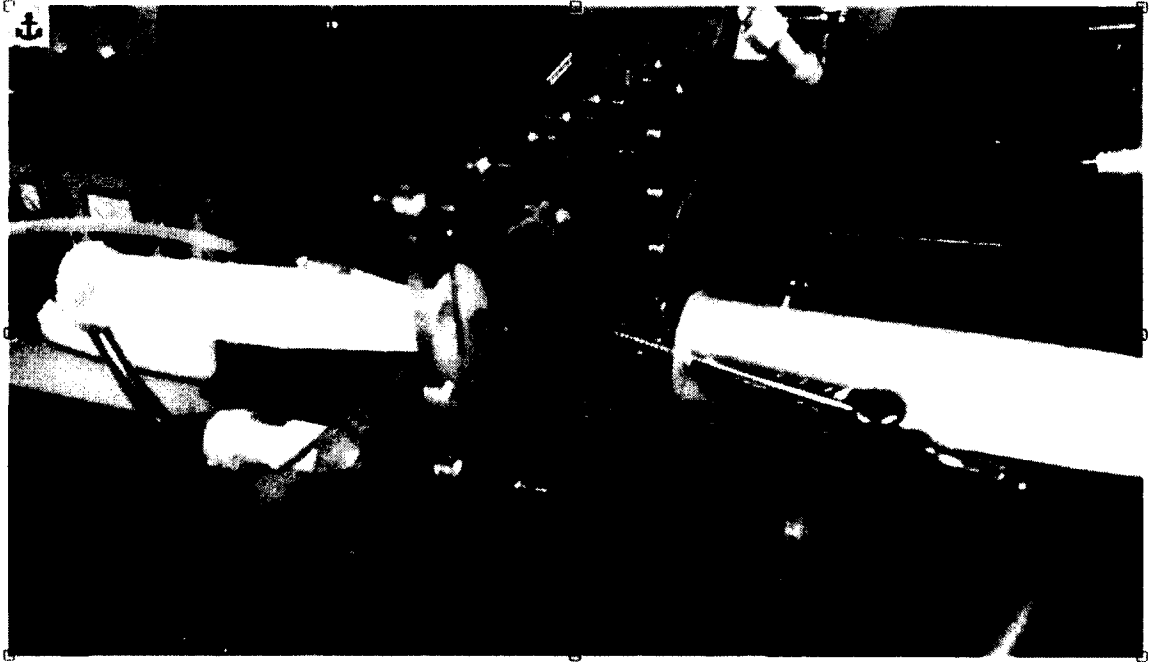


Figure 27. Electrode setup for the endo-epi configuration. The frame on which the tissue is stretched was taken out of the chamber to better access to perform the ablation.

2.6.1 CARDIAC FIBER ORIENTATION

The heart has its own special architecture. The wall of the heart consists of two thin layers at the surface, the epicardium (outer layer) and the endocardium (inner layer), and in between is the myocardium which makes up most of the wall⁶⁶. Figure 28 shows how the myocardial microstructure is made of laminar sheets of muscle fibers (called myofibers). The space between the laminar sheets is composed of extracellular liquid and a collagen network linking the laminar sheets together. Cardiac myofibers have anisotropic electrical conduction properties, i.e. impulse propagation is faster in the axial direction than transversally⁶⁷. The components of the conductivity tensors are determined by the electrical properties of the cardiac tissue and the fiber geometry. The electrical conductivity along the local fiber direction, called the longitudinal direction, is σ_L . The electrical conductivities perpendicular to the local fiber direction, called the transverse directions, are σ_{Ty} (in y-axis) and σ_{Tz} (in z-axis).

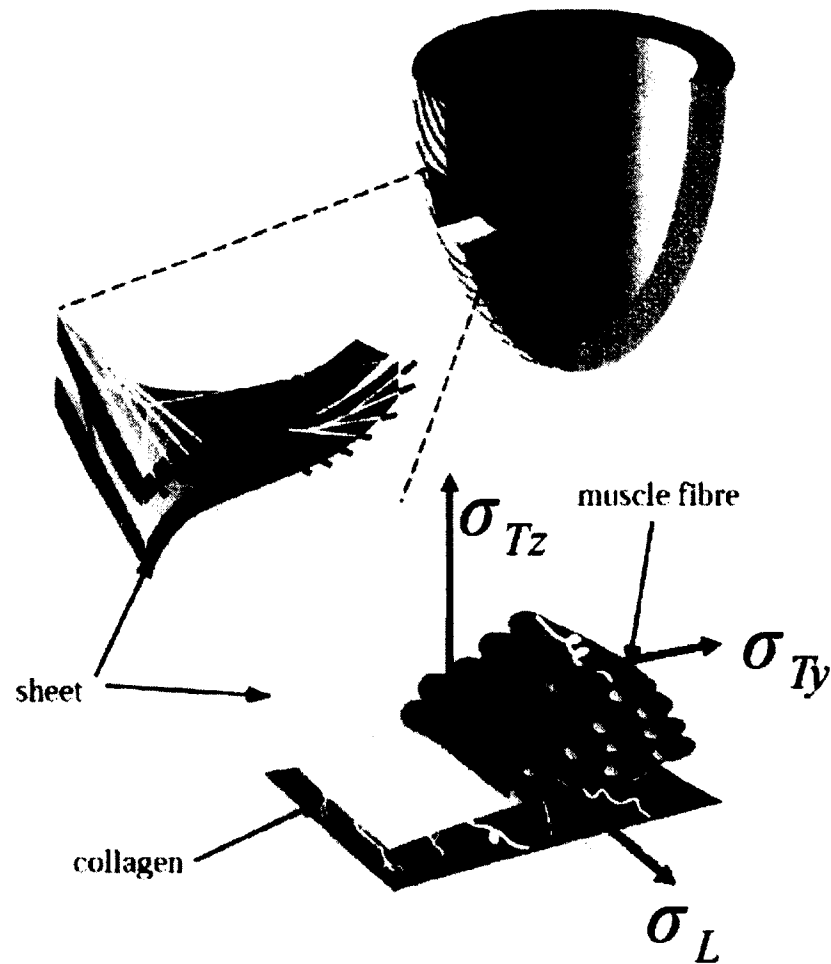


Figure 28. Cardiac fiber structure⁶⁵. The myocardium is made of laminar sheets of cardiac myofibers. Electrical conductivity along the fiber σ_L is larger than that in transversal direction, σ_{Ty} (in y-axis) and σ_{Tz} (in z-axis or called transmural direction).

Myofiber orientation is commonly quantified by the helix and transverse angles⁶⁸. The left panel of Figure 29 shows both transversal and helix angles. The transversal angle in the upper panel shows a tangential overall cardiac muscle fiber “spiraling” through the wall thickness from outer to inner surfaces. Within each layer of myocardium, transversal angles describe the individual rotation of the fiber with respect to its inner/outer layers.

Depending on the species of animal and the location site of the myocardium, transversal myofiber orientation varies from around -100° at the epicardium to 100° at the endocardium^{69, 70, 71, 72, 73}. Modern histological techniques have shown that in the plane of the wall, the mean muscle fiber angle makes a smooth transmural transition from epicardium to endocardium. In our numerical model, the fiber angles α always refer to the transversal angle in the bottom panel. Myocardial fiber orientations are conventionally measured using histology^{72, 73}. Figure 30 shows the sectioned transversal fiber angles of the canine and murine hearts.

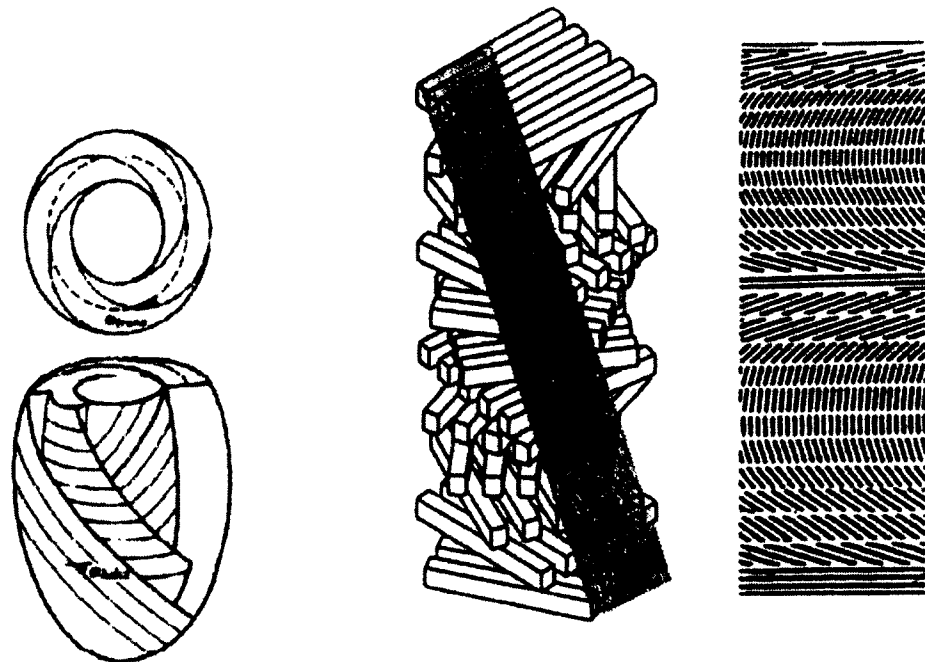


Figure 29. Schematic diagram of muscle fiber orientation in myocardium. **Left panel:** The bottom drawing shows the helix angle α_{helix} , which is negative at the indicated epicardial location; the upper drawing shows the transverse angle α_{trans} , in a top view of the basal plane⁸⁹. **Middle panel:** Parallel fibers which continuously rotate by a constant angle from plane to plane in a helical structure with a section in grey color. **Right Panel:** Microstructure of sectioned tissue⁹¹.

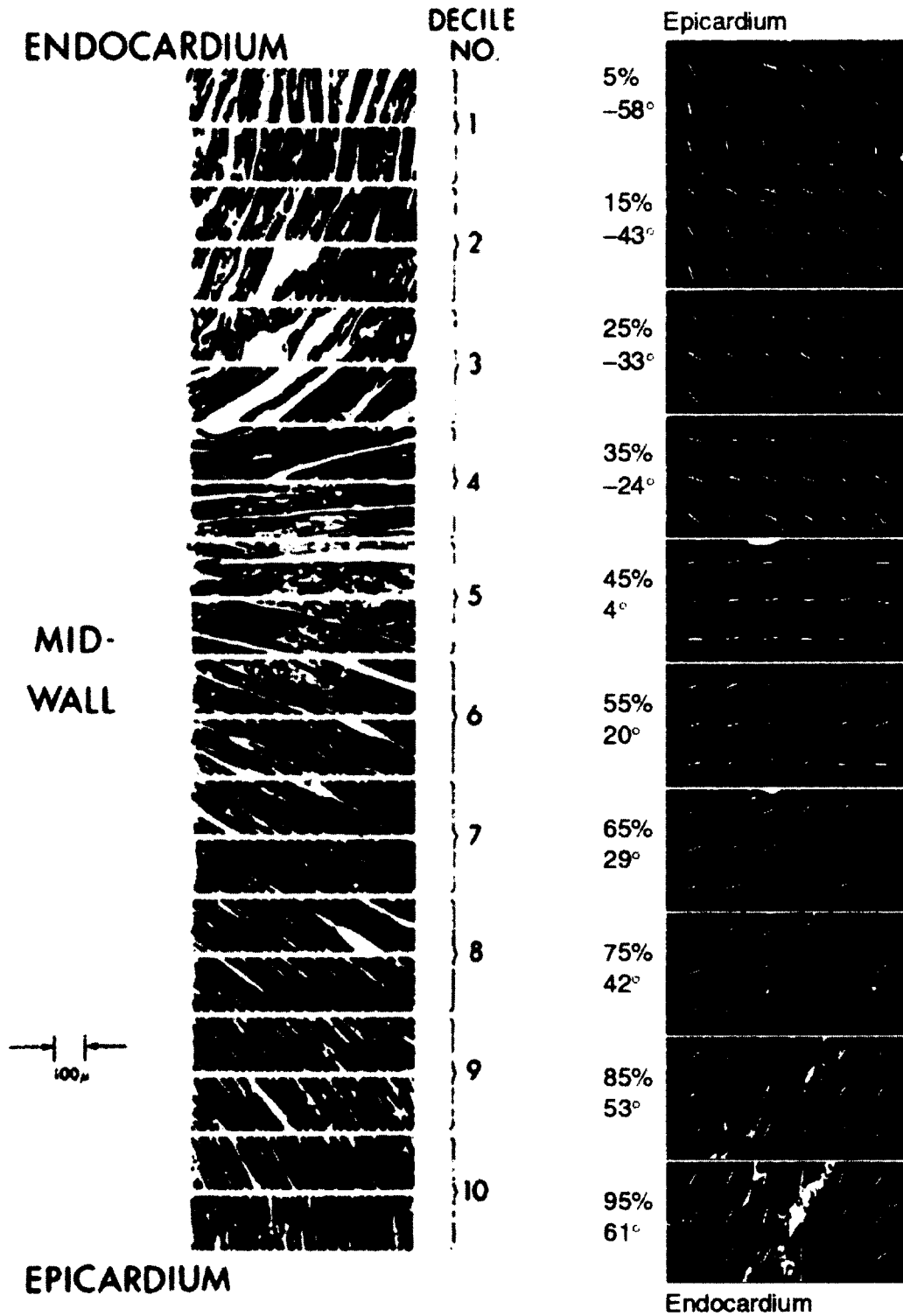


Figure 30. Typical sequence of photomicrographs showing fiber angles in successive sections taken from a heart (Left column: canine⁷³, right column: murine⁷²) The sections are parallel to the epicardial plane. **Left column:** The sequence of numbers refers to deciles of wall thickness. **Right column:** The percentage refers the depth into endocardium.

As a viable alternative to conventional histological sectioning, cardiovascular magnetic resonance (CMR) diffusion tensor imaging (DTI) has emerged with the advantages of being non-destructive, relatively convenient, and inherently 3D⁷⁴. A recent study quantitatively obtained myocardial fiber helix angles of mice, rabbits, and sheep using diffusion tensor cardiovascular magnetic resonance⁷¹.

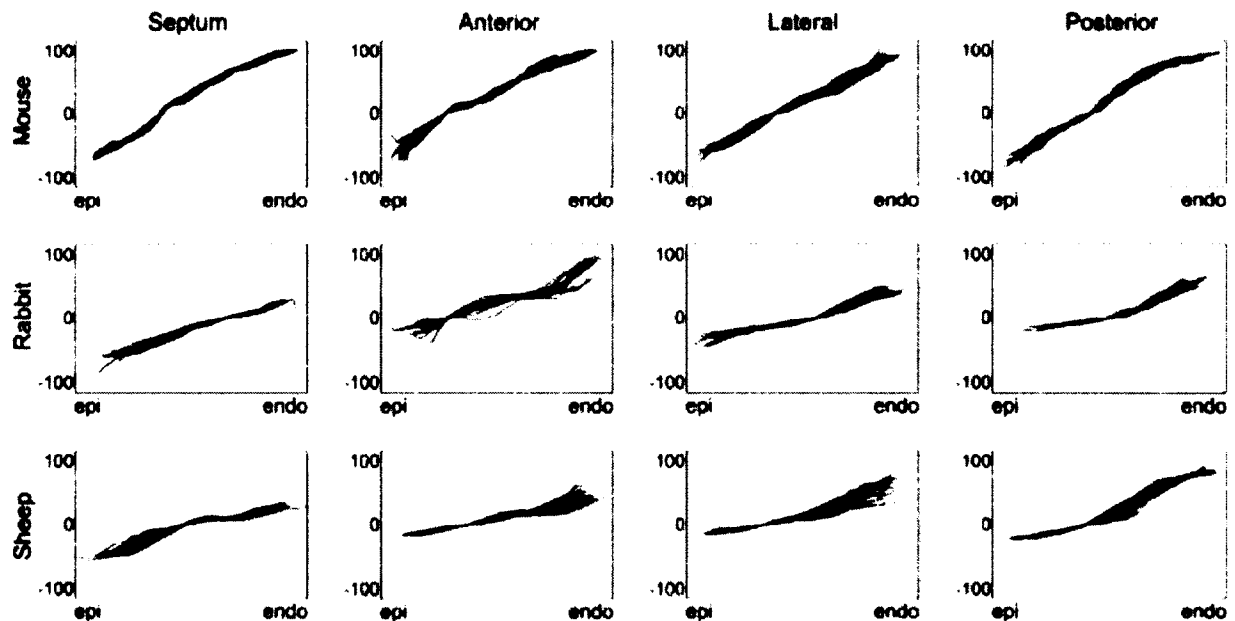


Figure 31. Transmural trajectories of the myocardial fiber helix angle obtained by DTI datasets of fixed, intact normal mouse, rabbit and sheep hearts⁷¹. Fiber rotation is given for different locations in the heart: the middle of the septum, anterior free wall, lateral free wall, and posterior free wall of left ventricles (see Figure 32).

The myocardial structural helix angles of the left ventricle were investigated at 4 wedge-shaped regions-of-interest (ROIs, Figure 31), at (a) the middle of the septum, (b) the anterior free wall, (c) the lateral free wall, and (d) the posterior free wall, as depicted in Figure 32.

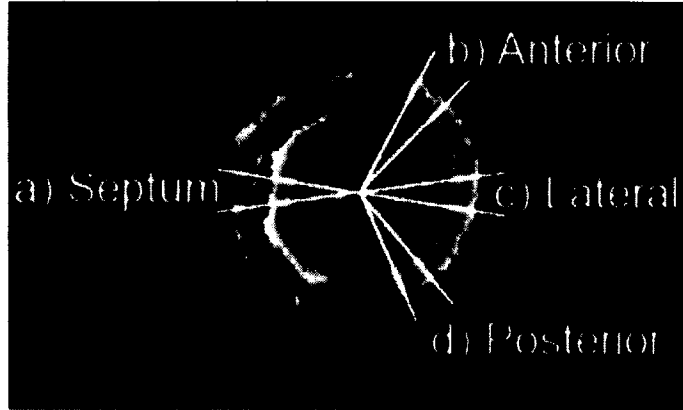


Figure 32. Regions of interest for left ventricular myocardial fiber helix angles analysis (see Figure 31). ROIs include (a) mid septal wall, (b) anterior, (c) lateral, and (d) posterior free wall⁷¹.

In order to best match the numerical simulation result to the nsPEF ablated rabbit hearts results, we chose the column “lateral data” of the rabbit heart from Figure 31. This is because the majority of our experiments were conducted in this ROI. Thus, the fiber helix angles are set to be -50° to 50° from epicardium to endocardium for numerical simulation. IRE ablation results relate to electric field distribution, which is dependent on the conductivity distribution in the targeted regions⁷⁵. Longitudinal and transversal electrical conductivities of the rabbit heart were determined by Schwab et al, using 3D confocal microscopy and image reconstruction⁷⁶. Longitudinal conductivity $\sigma_L = 0.264 \pm 0.082$ S/m, transversal conductivity in y-direction $\sigma_{Ty} = 0.126 \pm 0.056$ S/m, transversal conductivity in z-direction (transmural direction) $\sigma_{Tz} = 0.217 \pm 0.073$ S/m.

2.6.2 NUMERICAL MODELING EQUATIONS

The electrical potential within the tissue associated with the pulse is determined by solving the governing Laplace equation for the electrical potential Φ :

$$-\nabla \cdot (\sigma \nabla \Phi) = 0, \quad (1)$$

where σ is the electrical conductivity tensor, and the nabla symbol ∇ is defined by

$$\nabla = \vec{i} \frac{\partial}{\partial x} + \vec{j} \frac{\partial}{\partial y} + \vec{k} \frac{\partial}{\partial z} . \quad (2)$$

The electric field \mathbf{E} (vector) is defined by the gradient of the electric potential Φ :

$$\mathbf{E} = -\nabla \Phi. \quad (3)$$

In a 3D space, x , y , z components of the electric field are defined as

$$E_x = -d \Phi / dx \quad (4)$$

$$E_y = -d \Phi / dy \quad (5)$$

$$E_z = -d \Phi / dz. \quad (6)$$

The electrical boundary condition of the tissue that is in contact with one electrode on voltage, V_0 , is applied:

$$\Phi(x_1) = V_0. \quad (7)$$

The electrical boundary condition at the interface of the other electrode is

$$\Phi(x_2) = 0. \quad (8)$$

Then, for any small region of tissue, the conductivity tensor can be written with respect to a local coordinate system oriented along the longitudinal direction with 0 degree rotation as:

$$\sigma(0) = \begin{pmatrix} \sigma_L & 0 & 0 \\ 0 & \sigma_{Ty} & 0 \\ 0 & 0 & \sigma_{Tz} \end{pmatrix} \quad (9)$$

In all other layers, to represent this tensor in Cartesian coordinates, we must rotate this tensor by multiplying it on each side by a rotation matrix. We assume that the fiber orientation α is a function of layer depth z , and it is determined by local fiber orientation $\alpha = \alpha(z)$, so the corresponding conductivity tensor is:

$$\sigma(z) = \begin{pmatrix} \cos(\alpha) & -\sin(\alpha) & 0 \\ \sin(\alpha) & \cos(\alpha) & 0 \\ 0 & 0 & 1 \end{pmatrix} \begin{pmatrix} \sigma_L & 0 & 0 \\ 0 & \sigma_{Ty} & 0 \\ 0 & 0 & \sigma_{Tz} \end{pmatrix} \begin{pmatrix} \cos(-\alpha) & -\sin(-\alpha) & 0 \\ \sin(-\alpha) & \cos(-\alpha) & 0 \\ 0 & 0 & 1 \end{pmatrix}$$

(10)

$$\sigma(z) = \begin{pmatrix} \cos^2(\alpha(z))\sigma_L + \sin^2(\alpha(z))\sigma_{Ty} & \cos(\alpha(z))\sin(\alpha(z))(\sigma_L - \sigma_{Ty}) & 0 \\ \cos(\alpha(z))\sin(\alpha(z))(\sigma_L - \sigma_{Ty}) & \cos^2(\alpha(z))\sigma_{Ty} + \sin^2(\alpha(z))\sigma_L & 0 \\ 0 & 0 & \sigma_T \end{pmatrix} = \begin{pmatrix} \sigma_{x1} & \sigma_{x2} & 0 \\ \sigma_{y1} & \sigma_{y2} & 0 \\ 0 & 0 & \sigma_{Tz} \end{pmatrix}$$

(11)

Combining equations (1)-(6) and (11), equation (1) can be expanded as:

$$-(\sigma_{x1} + \sigma_{y1}) \vec{i} \frac{\partial E_x}{\partial x} - (\sigma_{x2} + \sigma_{y2}) \vec{j} \frac{\partial E_y}{\partial y} - \sigma_{Tz} \vec{k} \frac{\partial E_z}{\partial z} = 0 \quad (12)$$

All outer boundaries were assumed to be electrically insulating, i.e. $-\mathbf{n} \cdot \mathbf{J} = 0$, where \mathbf{J} is the magnitude of the current density.

The temperature distribution in the tissue can be obtained by transiently solving a modified version of the Pennes bioheat equation with the inclusion of a Joule heating term:

$$\rho C \frac{\partial T}{\partial t} = \nabla \cdot (k \nabla T) + |\mathbf{J} \cdot \mathbf{E}|, \quad (13)$$

where tissue density ρ is chosen to be 1000 kg/m^3 ⁷⁷, heat capacity C is chosen to be $977.16 \text{ J/(kg}\cdot\text{K)}$ ⁷⁸, and the thermal conductivity k is chosen to be $0.512 \text{ W/(m}\cdot\text{k)}$ ⁷⁹.

All external boundaries were treated as convective cooling, with an exterior temperature of 37°C (the heart was immersed into the Tyrode's solution during ablation):

$$-\mathbf{n} \cdot (-k \nabla T) = h(T_{ext} - T) \quad (18)$$

,where the heat-transfer coefficient h is set to be $25 \text{ [W}\cdot\text{m}^{-2}\text{K}^{-1}]$.

2.6.3 COMSOL SIMULATIONS

COMSOL Multiphysics is a powerful finite element analysis software that allows modeling and

simulation of many physics-based systems. It allows the computation of electrical fields in complex-shaped materials with arbitrary electrode positions. The AC/DC and Joule Heating module (version 4.3b) can be used to solve for the local electric field and temperature distribution when nsPEFs are applied.

Electrodes radius	electrode spacing	Tissue dimension	Tissue layers	Tissue fiber helix angle	Tissue conductivity
250 μm	2 mm	5 mm radius; 4 mm thickness	40	$\alpha = -50^\circ$ to 50° , each layer has the increment of 2.56° ⁷¹	$\sigma_L=0.264$, $\sigma_{T,y}=0.126$, $\sigma_{T,z}=0.217 \text{ S/m}$ ⁷⁶

Table 3: Geometry and dielectric property of tissue and electrodes

To include the anisotropic conductivities with twisted fiber direction from epicardium to endocardium, the epicardium was set to be -50° , with increments of 2.56° for each layer, and the 40th layers (endocardium) will be around 50° . The definition of the fiber helix angle α in COMSOL is illustrated in Figure 33.

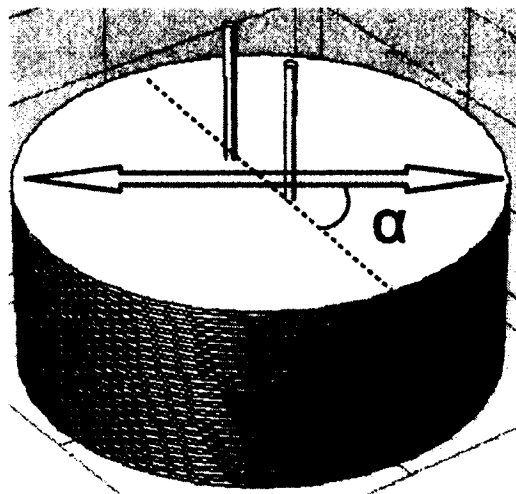


Figure 33. Definition of fiber helix angle α for COMSOL numerical model.

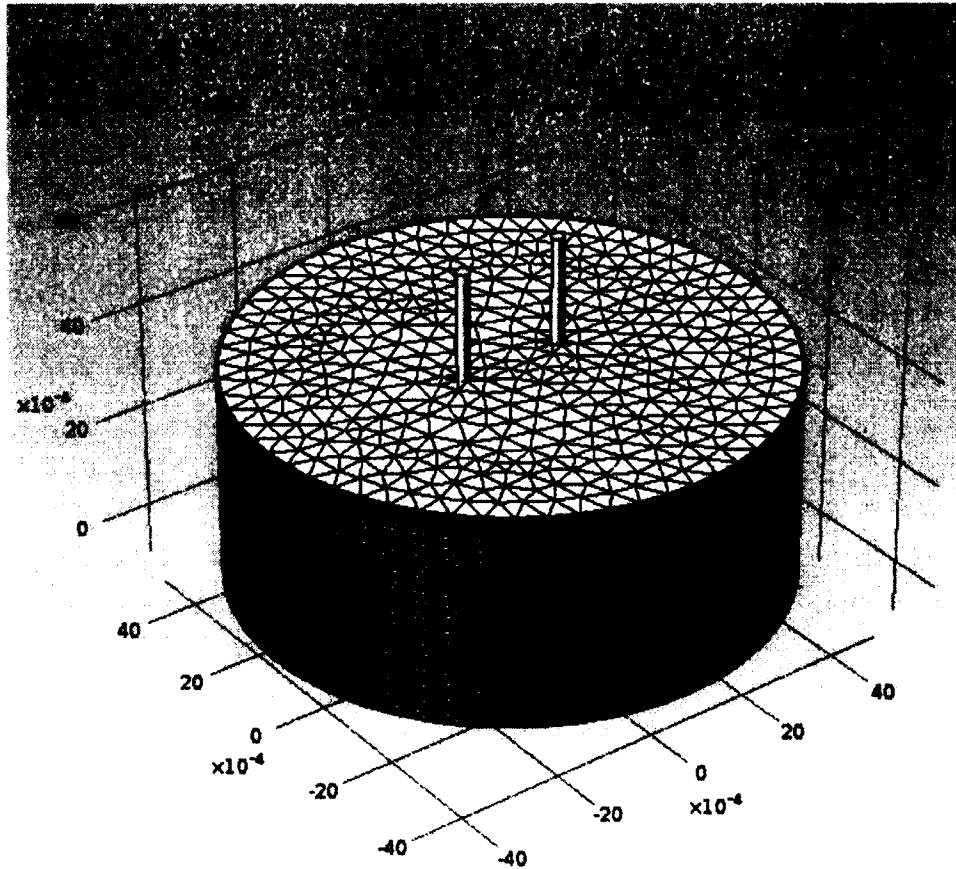


Figure 34. Mesh of the physical model. Note the pair of electrodes that are inserted into the cylindrical cardiac tissue.

A 3D geometry with the same dimensions as our experimental setup (see Table 3) was constructed in COMSOL. The mesh that COMSOL generated consisted of 101,963 tetrahedral elements (Figure 34).

CHAPTER III

EXPERIMENTAL RESULTS

In this chapter, we demonstrate the effectiveness of nsPEF ablation with different electrode configurations, both in optical mapping experiments and with histological analysis of the treated tissue with PI and TTC stains.

A total of 21 rabbits were sacrificed for this ablation project in the past 2 years. The primary goal for this project is to achieve fast and effective nsPEF ablation to create lesions on the ventricular wall of the heart experimentally. The strategy of achieving this goal was divided into 3 steps:

- 1) Testing single application ablation with different electrode spacings and pulse amplitudes,
- 2) Single application ablation with faster speed,
- 3) Multiple application ablations to create lesions.

The reasoning behind this approach is that the effects of electrode spacing and pulse amplitude (Step 1) are complex and should be studied in the simplest possible setting first. We started with a pulse protocol that was successful in tumor ablation and verified that it also can ablate cardiac tissue. Then we studied the effects of varying electrode spacing and pulse amplitude.

Once we understood how we could ablate a volume of the desired geometry, we tried different pulse protocols to increase ablation speed while preserving the ablation geometry as much as possible (Step 2).

With Steps 1 and 2 in place, we had a fast way of creating a single ablation with desirable geometry, and then considered how best to concatenate multiple such ablations into lesions.

3.1 SINGLE APPLICATION ABLATION TESTING

Optical mapping results

Using both activation and amplitude maps, we were able to show that nsPEFs generate electrically inactive tissue that blocks the propagation of excitation. Figure 35 shows a successful ablation with a shock amplitude of 2kV, 20 pulses at the frequency of 1 Hz, and 2 mm electrode spacing. In Figure 36, we reduced the shock amplitude to 1.5 kV. We still observe block, although Panel C shows that the ablated area is reduced in size. In Figure 37, we show that still lower amplitude further reduces the size of the ablated area (Panel C), and propagation block is no longer achieved (Panel B).

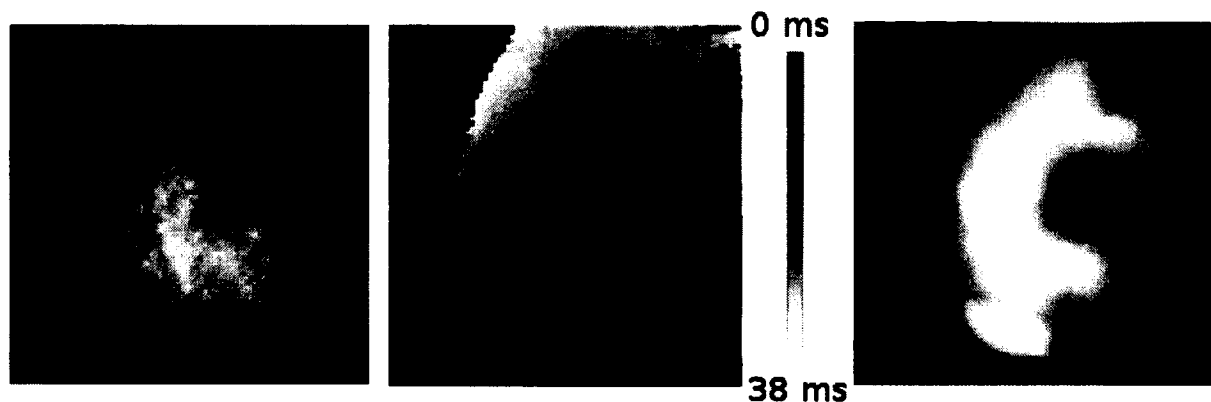


Figure 35. Single ablation shows that action potentials can be blocked successfully in the targeted region (2kV, 20 pulses at the frequency of 1 Hz, 2 mm electrode spacing). **Left:** Photograph of the cardiac surface. The two dark dots were mark the locations of the penetrating electrodes. The black needle on the right part is the stimulation electrode. **Middle:** Activation map, showing the activation sequence. **Right:** Amplitude map shows the amplitude of electric signals for each pixel. White color means maximum amplitude, while dark means minimum or zero amplitude.

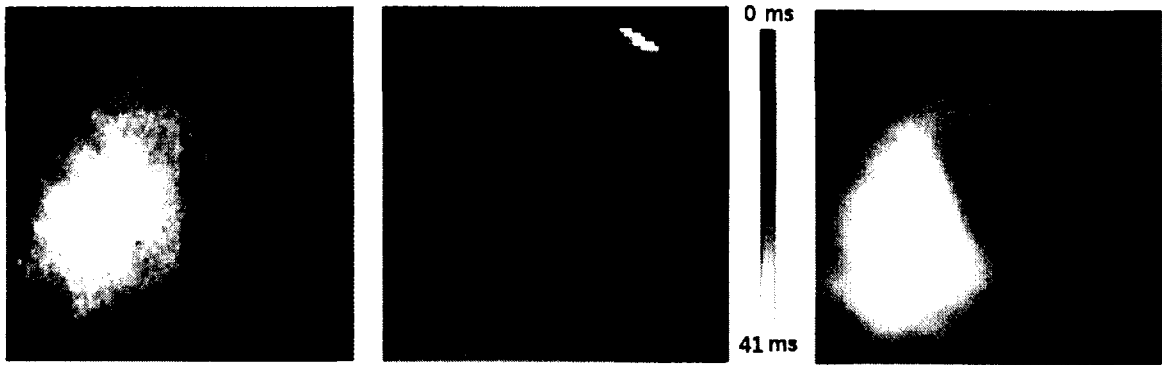


Figure 36. Smaller ablated area obtained with lower pulse amplitude (1.5kV, 20 pulses at the frequency of 1 Hz, 2 mm electrode spacing). See the caption of Figure 35 for details.

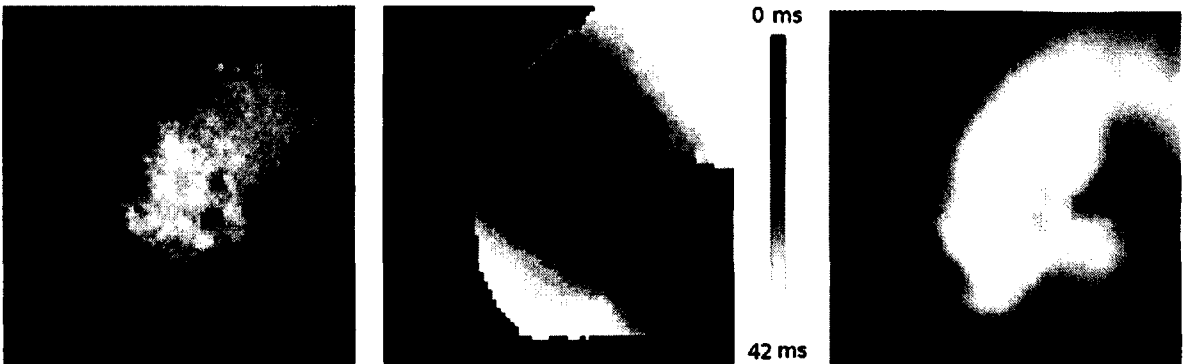


Figure 37. Incomplete block (0.7kV, 20 pulses at the frequency of 1 Hz, 2 mm electrode spacing). See the caption of Figure 35 for details.

For an increased electrode spacing of 4 mm, we observed the same general dependency of ablation result on the pulse amplitude: small amplitudes created no block; sufficiently large amplitudes did create block, and any further increase further increased the ablated volume. As expected, the larger electrode spacing required a larger shock amplitude to achieve block and led to larger ablation volumes (for sufficiently large fields). Figure 38 shows a representative result for 4 mm electrode spacing and otherwise the same pulse parameters as the result shown in Figure 35.

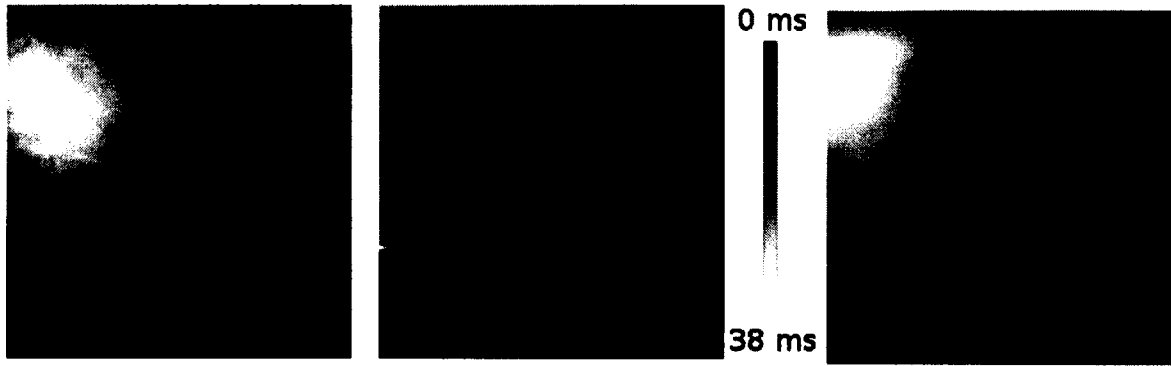


Figure 38. Ablation with 4 mm electrode spacing (2 kV, 20 pulses at the frequency of 1 Hz, 4 mm electrode spacing). For details, see the caption of Figure 35.

Histology results

With PI staining, we confirmed that the propagation block that we observed in optical mapping experiments is indeed the result of tissue ablation (i.e. the tissue has been killed).

Figure 39 shows that we can create a contiguous area of dead tissue around both electrodes, both for 2 mm and for 4 mm electrode separation. The fluorescence is recorded from the epicardial surface in all preparations. In the case of 4 mm separation, we further show that, as expected, a larger pulse amplitude leads to a larger ablated area.

In Figure 40, we show in more detail how the ablated surface area depends on pulse amplitude, for a fixed electrode distance of 4 mm. For a pulse amplitude of 1 kV (Panel A), we observe some dead tissue about each of the electrodes, but there clearly is surviving tissue between the electrodes. Such an ablation would not cause conduction block. For a pulse amplitude of 2 kV (Panel B), the ablated area has increased significantly and there is no more surviving tissue between the electrodes. If the amplitude is further increased to 4 kV, the ablated area becomes wider (Panel C).

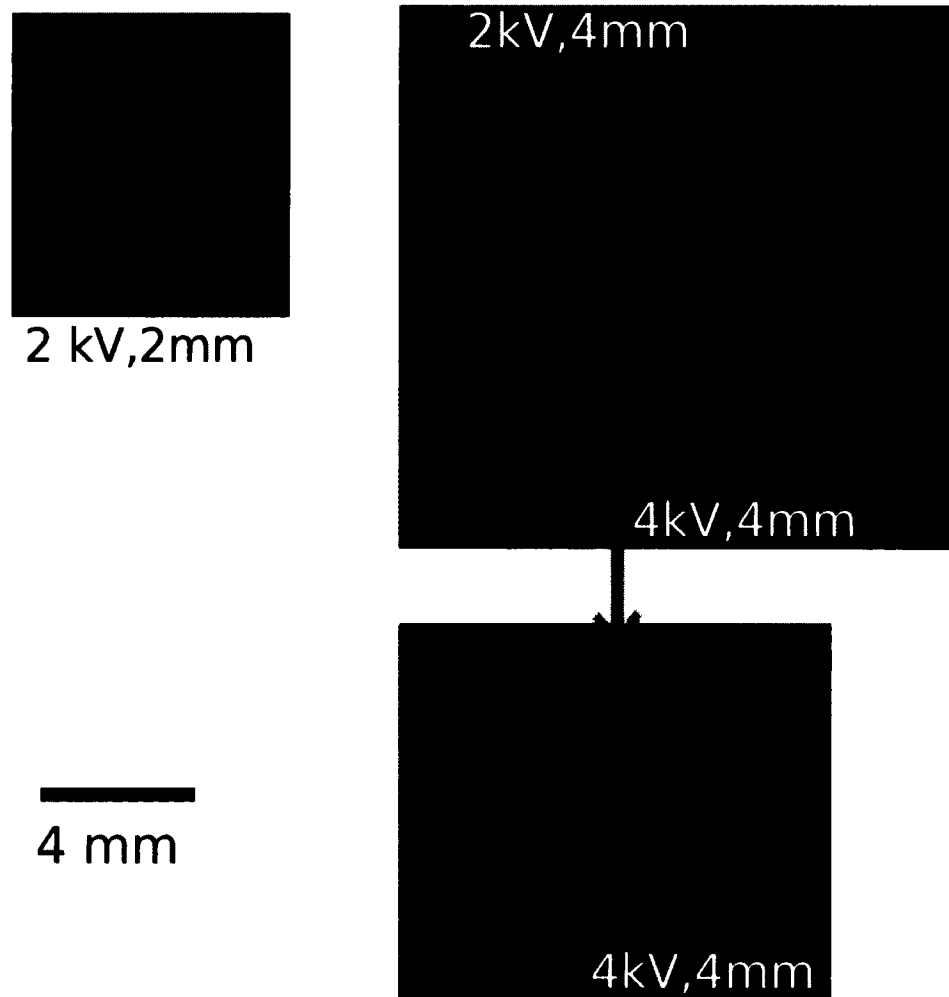


Figure 39. PI fluorescence for ablation with different parameters. It was found that the width of the ablated area is ~ 3 mm for 2kV and 2 mm spacing, and 4.5 mm for 4 kV and 4 mm spacing. Another view of the 4kV, 4 mm ablation was shown under the green arrow for a better view, by adjusting the recording angle.

The fluorescent image came from PI staining of the heart, when excited with green laser and filtered and recorded by a Canon EOS Rebel T1i camera. The fluorescent area indicates high PI concentration, which occurred in dead cells where PI can enter and bind to the DNA (those PI which cannot bind to live cells were washed out by the perfusion of Tyrode's solution). The strong fluorescence indicates that there was a high concentration of dead cells, most likely because the electric field was strongest around the electrodes (marked as two dark dots by surgical ink). We also noticed there was weaker fluorescent light further away from the electrodes, indicating fewer dead

cells due to a weaker electric field.

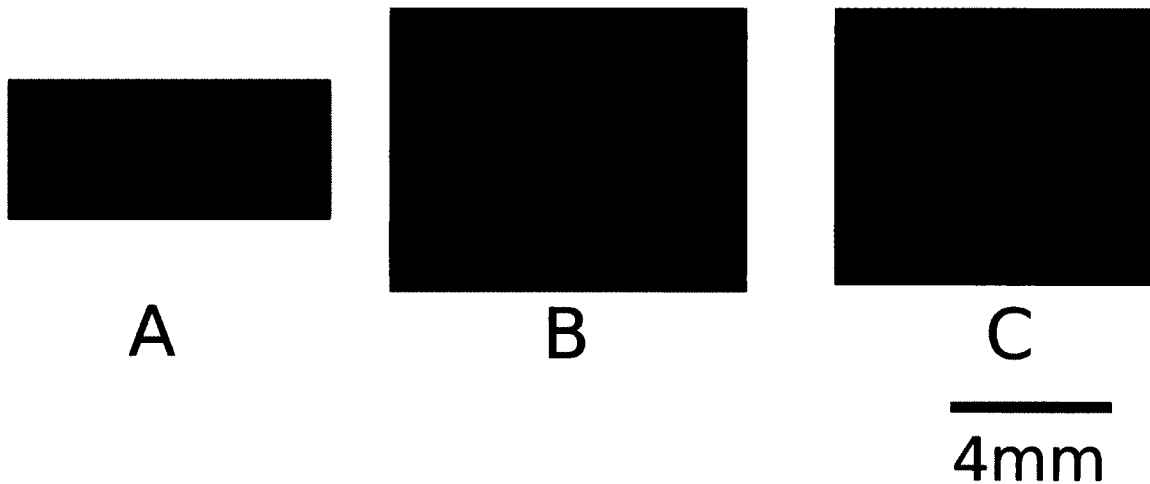


Figure 40. Comparison of different pulse amplitudes, applied with 4 mm electrode spacing (20 pulses). **A:** 1 kV. **B:** 2 kV. **C:** 4 kV.

To determine if the ablation is symmetric from epi- to endocardium, we sectioned all the PI stained tissue with 300 μm thickness (4 kV, 20 pulses at 1Hz, 4 mm electrode spacing). Then we recorded the fluorescence for each section (see Figure 41A). By defining a fluorescence threshold that corresponds to dead tissue and stacking the sections, we could reconstruct the three-dimensional geometry of the ablated volume (see Figure 41B). It can be seen that there is indeed good approximation translational symmetry, and that the boundaries are quite smooth and uniform. The shape shown in Figure 41B is well suited to create linear non-conducting lesions.

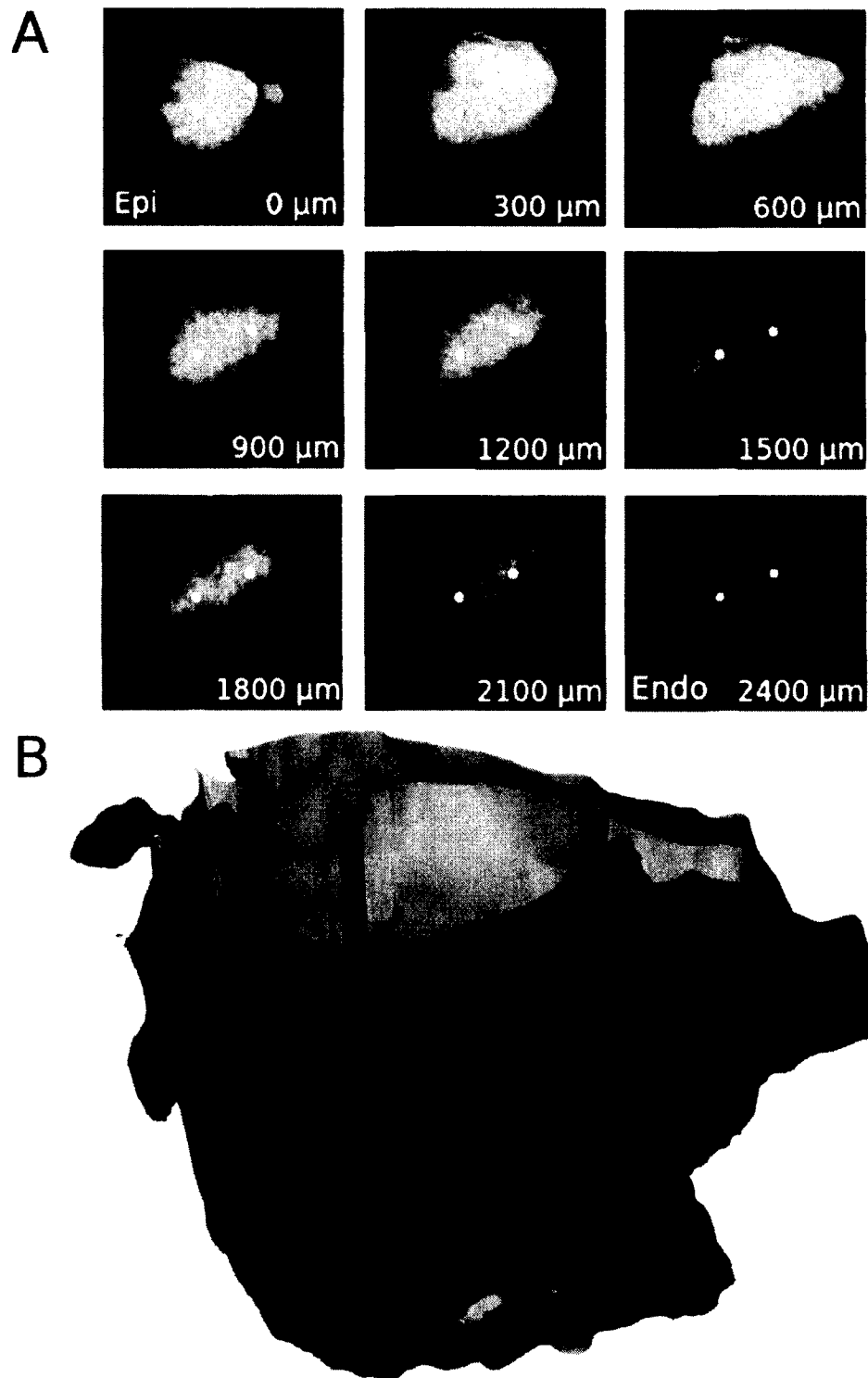


Figure 41. Three-dimensional reconstruction of the ablated volume (4 kV, 20 pulses, 4 mm electrode spacing). **A:** Post-processed propidium iodide fluorescence images of the individual sections. For each section, we indicate its distance from the epicardium. The total thickness of the tissue was 2,400 μm . **B:** Rendering of the 3D geometry of the ablated volume. Red rods indicate the shock electrodes, gray surface encloses the ablated area.

3.2 FASTER SINGLE APPLICATION ABLATION

It would be very desirable to reduce the ablation time needed for RF ablation, typically around 30-60 seconds, for a single ablation. In the previous section, using 20 pulses at a frequency of 1 Hz, we achieved a reduction of ablation time to 20 seconds per site. In order to ablate the cardiac tissue even faster, we attempted the single application ablation using fewer pulses, and faster repetition rates. We succeeded with 5 pulses at the frequency of 3 Hz. We found this ablation is effective as for 20 pulses at 1 Hz if we adjust the amplitude from 2 kV to 2.3 kV for 5 pulses ablation. It should be expected that lower number of pulses requires higher amplitude of pulses to permeabilize a similar population of cell membranes, thus to ablate the same volume of tissue. With 5 pulses at 3 Hz, a single application ablation takes less than two seconds, so that there is not much to be gained by further reduction of the number of pulses. We tried to ablate with single shocks but did not succeed with the maximum shock amplitude that our pulser could produce (approximately 8 kV). It should be noted that for our ultimate goal delivering nsPEF ablation pulses through a catheter, it is desirable to keep the pulse amplitude down (this reduces the risk of sparking between the wires), so that the 5 pulses at 3 Hz whose effectiveness we demonstrated may not need to be modified.

Figure 42 illustrates tissue is ablated with 5 pulses of 2.3 kV at the frequency of 3Hz. We performed 15 such ablations in 5 different hearts, and all of them exhibited block as shown in Figure 42.

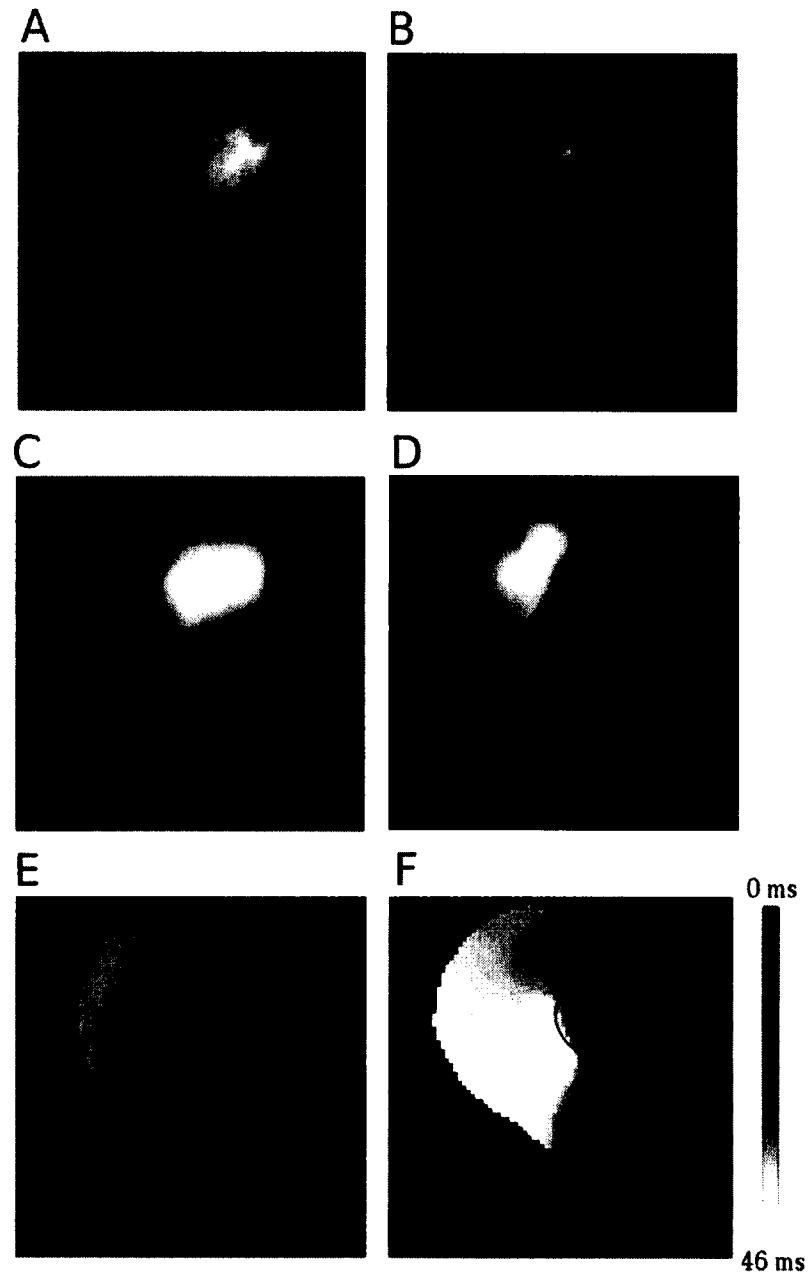


Figure 42. Cardiac surface before and after an ablation (2.3kV, 5 pulses at the frequency of 3Hz with 2mm electrode spacing). **A:** Photograph of the cardiac surface before ablation. **B:** Photograph of the cardiac surface after ablation. The electrode insertion points are marked by black dots. The elongated black shape on the right is the shadow of the stimulation electrode (used to initiate electrical activation). **C:** Action potential amplitude map before shock application. Black corresponds to zero action potential amplitude, white to maximal action potential amplitude. **D:** Action potential amplitude map after shock application. The action potential amplitude is dramatically reduced in the area between the shock electrodes. **E:** Activation map before shock application. Colors code the time after stimulus application at which a surface element is activated. Black areas are activated first, white areas last (see scale). Arrows show the propagation speed proportional to the scale. **F:** Activation map after shock application. Activation travels around the area of shock application with curved arrows. The two red spots mark the location of the electrodes, and the circled area shows the ablated tissue.

3.3 MULTIPLE APPLICATION ABLATIONS TO CREATE LESIONS

To demonstrate non-conductive lesions convincingly, the anisotropic nature of cardiac tissue should be considered. Generally, cardiac activations travel faster in the local direction of the fibers than orthogonal to it. It is best to first identify the direction of fast propagation at the stimulation electrode (see the green arrow in Figure 43) and then orient the lesion perpendicular to that (the red line in Figure 43). The reason such a perpendicular orientation is preferred is that a conduction block is more readily visible if fast propagation is blocked than if slow propagation is blocked.



Figure 43. Determining optimal orientation for lesions to best demonstrate non-conductiveness using an activation map. The direction of fastest propagation (green arrow) is determined before ablation, and then lesions are created perpendicular to this direction (red bar), to produce pronounced conduction block.

While our previous results showed that we can fully ablate the tissue between the electrodes for a spacing of either 2 mm or 4 mm, we focused on 2 mm spacing in the following simply to have enough space in the rabbit ventricle to perform several ablations in a row (typically 4 or 5).

We considered 3 different ways to create lesions by a single application ablation we proposed at

the beginning of the experiment, shown in Figure 44. For the first ablation scheme (Panel A), we would move the ablation electrodes in the direction defined by the insertion points between shock applications. More specifically, we would move them by more than the electrode spacing so that the lesion becomes contiguous only if each single application ablates tissue beyond the area between the electrodes. In our experience, for an electrode spacing of 2 mm, moving the electrodes by 3 mm between applications is appropriate. This results in gaps of 1 mm between the insertion points and consistently gave us non-conducting lesions.

In a second ablation scheme, the electrodes are still move in the direction defined by their insertion points, but only by half the electrode spacing, so the single application ablations become interwoven (Figure 44 B). This should lead to more uniform lesion thickness, but the ablation process should take about twice as long as for side-by-side lesions. We have successfully used this scheme a few times, but have not pursued it further because the more efficient scheme shown in Figure 44A consistently produced non-conducting lesions.

The third ablation scheme that we considered is to move electrodes in the direction perpendicular to that defined by their insertion points between shock applications. This is the most time-consuming scheme, but it should lead to the lesions with most homogeneous widths. As in the case of the second ablation scheme, we only tried a few ablations with this scheme because it is more time consuming and the anticipated gain in uniformity was not yet a major concern.

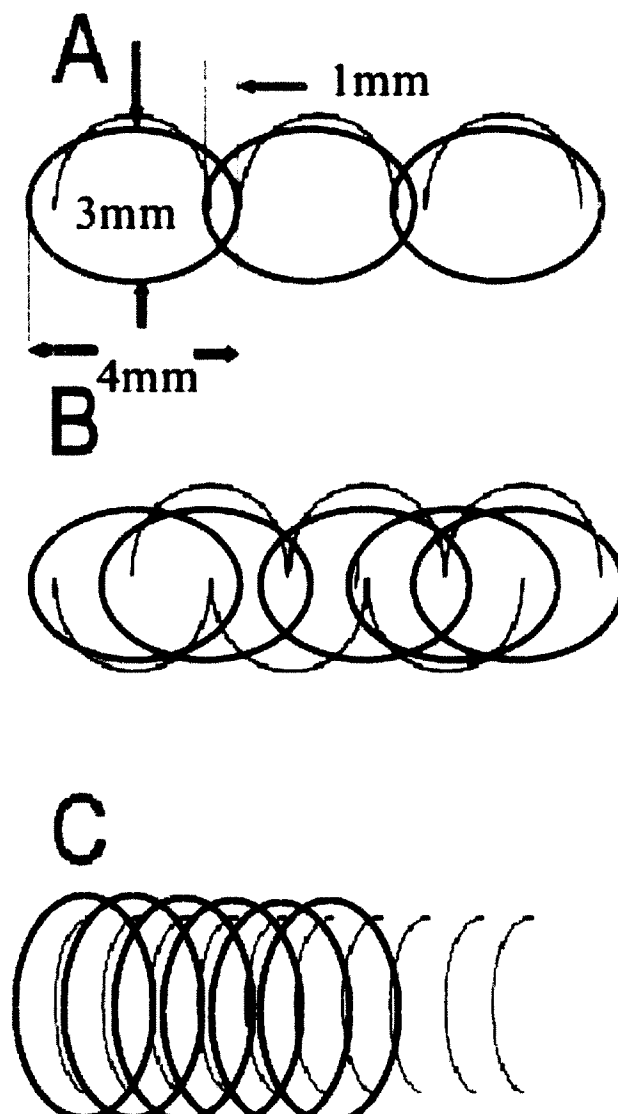


Figure 44. Different ways of creating lesions from single application ablations. Each semicircle indicates a single ablation application with the electrode positions at the end points of the semicircle. Ablated area are circled in red color. **A:** Electrodes are shifted in field direction between applications, large shift. **B:** Electrodes are shifted in field direction between applications, small shift. **C:** Electrodes are shifted perpendicular to the field direction between applications.

Optical mapping results

In each rabbit heart, there was enough space to create 2 lesions on each free ventricular wall using the scheme of Figure 44A. In our experiments, we successfully created lesions of length 12-14 mm, which need 4-5 single ablations. Figures 45 and 46 show representative optical mapping

data that demonstrate the presence of non-conductive lesions.

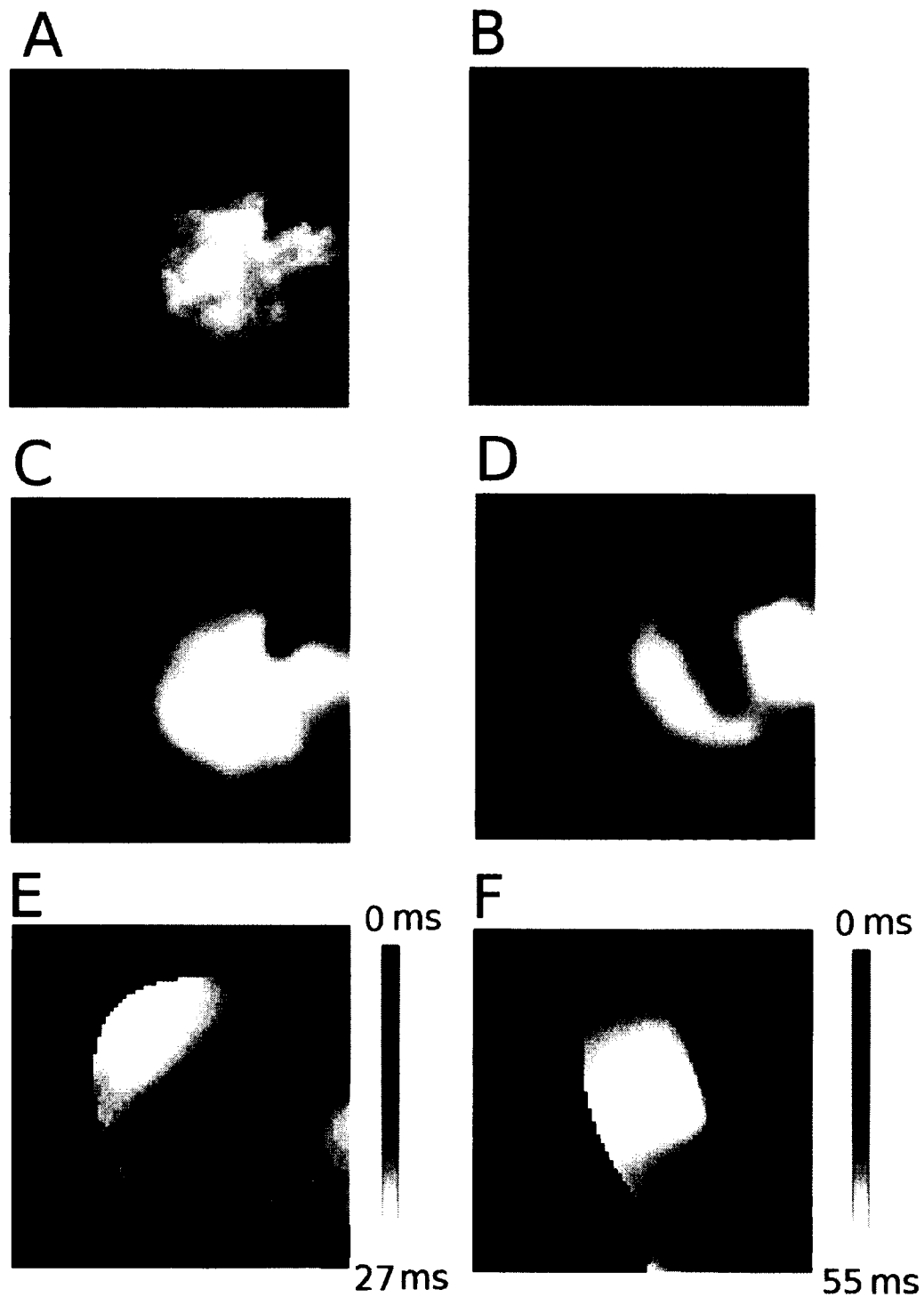


Figure 45. Optical mapping data verifies that lesions were created successfully by multiple ablations on left ventricle of rabbit heart (5 single ablations conducted by side-by-side method, each ablation adopted the parameter of 2.3 kV, 5 pulses at the frequency of 3 Hz with 2 mm electrode spacing). See captions of Figure 42 for details.

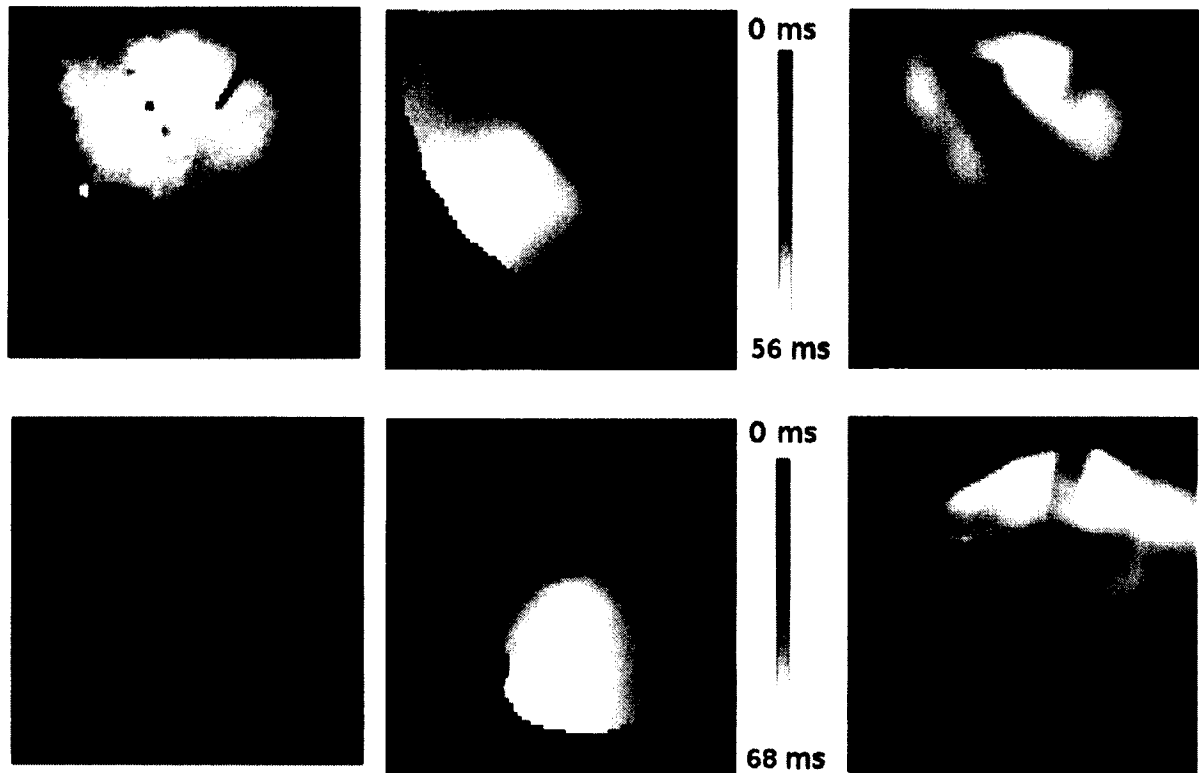


Figure 46. Two more successful nsPEF lesions, one created on the left ventricle (upper row) and one on the right ventricle (lower row) of a rabbit heart. **Left column:** Photographs of ablated tissue. **Middle column:** Activation maps. **Right column:** Amplitude maps.

Histology results

As we described in Section 2.1.5, we originally used PI to measure the extent of tissue ablation in our experiments but later switched to TTC. As a result, we have two different sets of data that characterize the geometry of the lesions that we created with nsPEF. Here, we show the TTC results because they offer a more detailed view, but in our statistical analysis (Section 3.4), we consider lesion data obtained with both methods.

Figure 47 shows sample sets of TTC-stained sections of lesions parallel to the cardiac surface. Sections of 300 μm thickness were obtained at different tissue depths; each column illustrated the sectioned tissue from epicardium to endocardium. If the lesion happened to be located on a part of the heart with high curvature, we discarded sections that contained too little tissue; that is the reason why the number of sections differs from section to section.

In the left column of Figure 47, we observed straight, sharp boundaries between ablated and surviving tissue. Indeed, the zoom shown in Figure 48A shows that there is an almost complete switch from white (dead) tissue to red (live) tissue from one fiber to the next, i.e. within about 100 μm . The middle and the right column of Figure 47 exhibit more curved boundaries between ablated and surviving tissue, and the zoom in Figure 48B shows that the boundaries are not quite as sharp as in the case of Figure 48A.

Further experiments confirmed that when the applied field is in the fiber direction, we get straight and very sharp boundaries; if the field is applied across fibers, the boundary is less straight and not quite as sharp. A compelling explanation for this finding is that the good connectivity along fibers facilitates the exchange of ions and molecules, including those specific to dead cells that may also harm neighboring cells (“death signals”). In this view, death of part of a fiber promotes death of the remainder of the fiber. Applying this idea to Figures 47 and 48, we should expect that in the left column of Figure 47 and in Figure 48A, in which the field within each fiber is relatively constant, to either die completely or not at all. At the same time, the middle and right columns of Figure 47 and Figure 48 show a situation in which the fibers extend from the maximum between the electrodes all the way to near-zero fields, so the cells that make up the fiber should die between the electrodes but not far away from them. Still the “death signal” from the cells between the electrodes travels outside for some distance, and this process is not stable and leads to less straight and sharp boundaries.



Figure 47. TTC stained sectioned tissue with lesions created using 2.3kV and 5 pulses at a frequency of 3Hz with 2mm electrode spacing for both columns. Section thickness is 300 μ m.

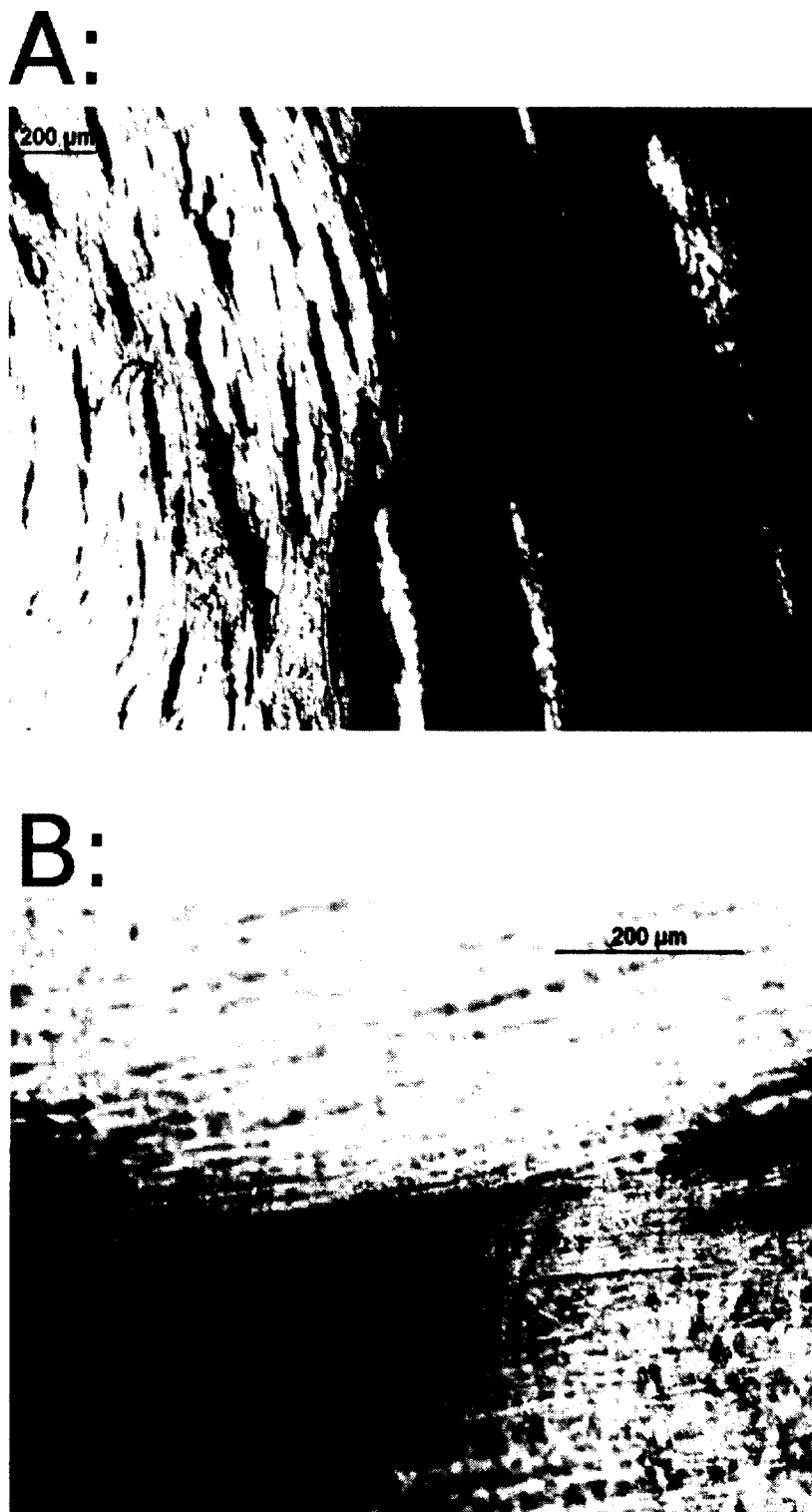


Figure 48. Microphotographs of the marked regions in Figure 47. **A:** Microstructure of highlighted region on the left column of Figure 47. Fibers are aligned with the applied field. **B:** Microstructure of highlighted region on the right column of Figure 47. Fibers are perpendicular to the applied field.

We used the sections of Figure 47 to reconstruct the 3D geometry of the sections (see Figure 49). The sharp, straight boundary and great consistency of the ablated volume are far superior to the geometry that RF ablation achieves. Even the middle and the right row, for which the boundary is less straight, have excellent consistency of the ablated volume from epi- to endocardium.



Figure 49. 3D re-construction for the TTC sectioned tissue on the left column of Figure 50. The two renderings show the same ablation volume from different angles.

3.4 LESION WIDTH STATISTICS

A total of 12 rabbits were used to acquire lesion statistics and assess the reproducibility of lesion creation (14 lesions were evaluated). The results are illustrated in Figure 50. For 2 mm electrode separation and 2.3 kV pulse amplitude, we assessed the lesion width both with PI stains and TTC stains. For PI stains ($n=7$) we found an average width of 2.3 mm (standard deviation 0.2 mm), while

with TTC stains (n=7), the average was 3.1 mm (SD 0.56 mm). We also created two lesions with 4 mm electrode separation and 4.3 kV pulses (n=2); evaluation of the lesion with TTC staining gave an average thickness of 5.5 mm (SD 0.5 mm).

Differences between the PI and TTC values may on the one hand be caused by the blurred images that PI staining produces, which limits the accuracy with which we can determine lesion thickness. At the same time, the stains target different, complex processes in the cell (see Section 2.1.5), and some variation should be expected.

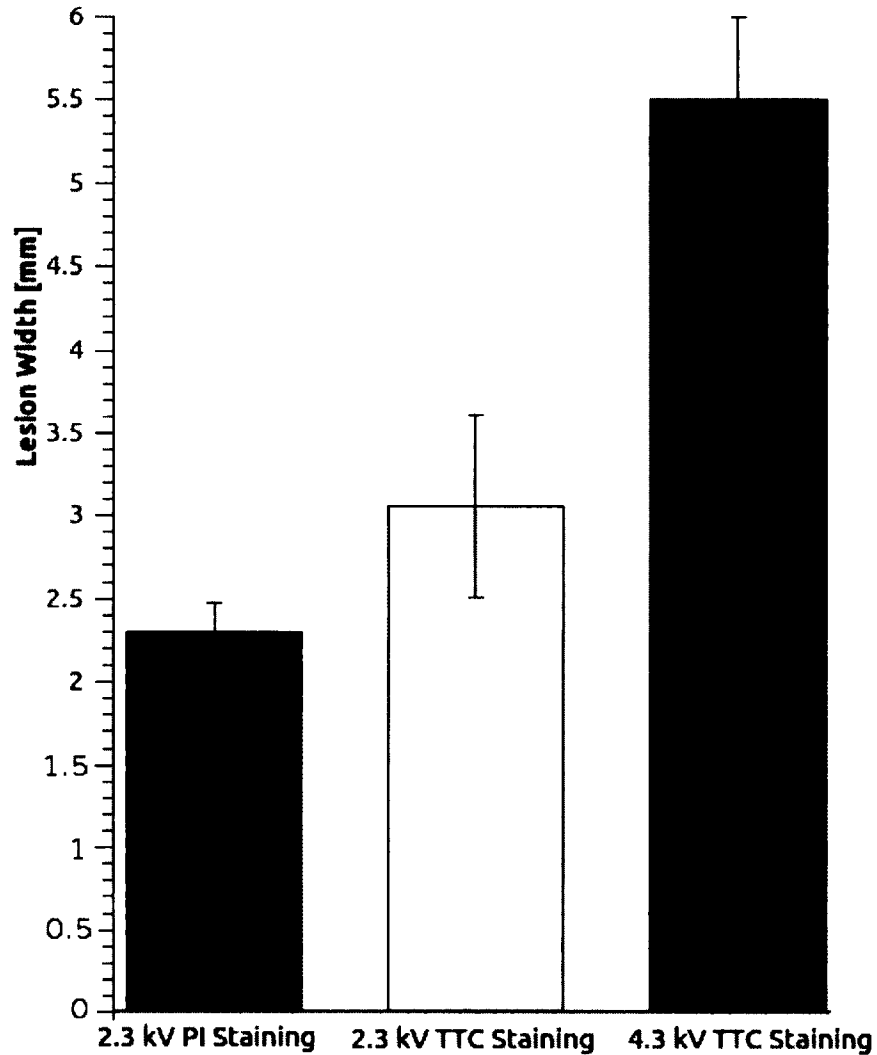


Figure 50. Lesion width statistics and standard deviation for different pulse amplitudes. Lesion width was measured perpendicular to the line connecting the electrodes, at the midpoint between the electrodes.

3.5 EXPERIMENTAL RESULTS FOR ENDO-EPI CONFIGURATIONS

Besides the penetrating electrodes configuration, we also tested the ablation effect with endo-epi configuration (one electrode touching the endocardium and the other the epicardium, see schematic in Figure 51). Figure 51 shows that with 6.5 kV, 6 pulses at 3 Hz, we achieved a complete transmural and very uniform ablation, a dramatic improvement over the results other groups published for nsPEF ablation (see Figure. 8).

To get further information on the 3D geometry of the lesion, we sectioned the tissue parallel to the cut surface shown in Figure 51. The results are shown in Figure 52; increasing section numbers indicate greater distance from the surface shown in Figure 51. The lesion remains transmural in all sections, although the width of the lesion expectedly decreased and some surviving islands of tissue are visible in sections 7-9.

A second lesion was created with the same pulse parameters. This lesion was shipped out for histological analysis with yet another stain (Masson trichrome stain), and the results are not back; however, visual inspections showed that the ablation was successful and the lesion geometry very similar to that shown in Figures 51 and 52.

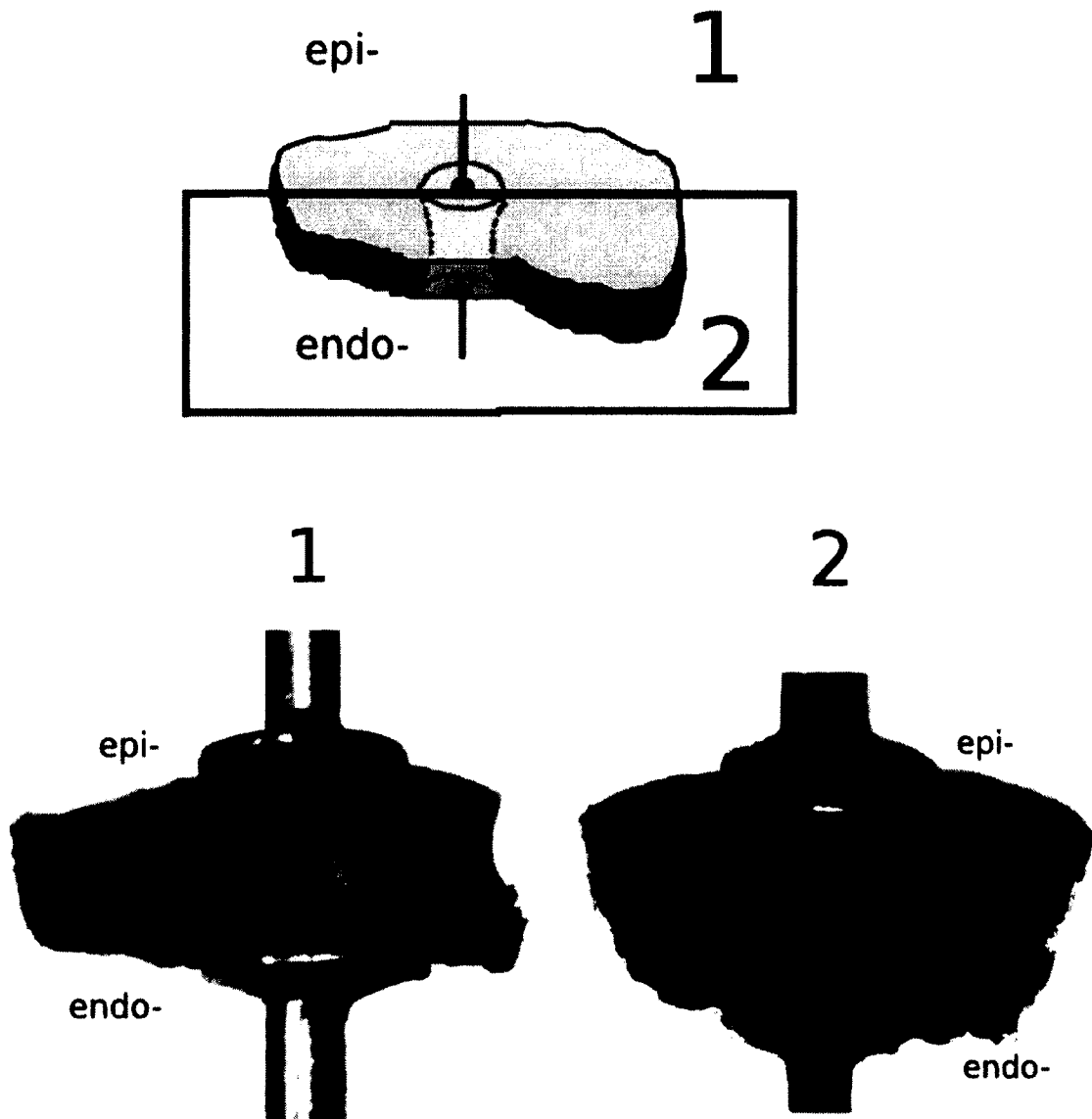


Figure 51. Cross sections of nsPEFs ablated tissue stained with TTC with 6.5 kV, 6 pulses at the frequency of 3 Hz. Schematic diagram shows that the targeted tissue was ablated with one electrode on the epicardium and the other one on the endocardium. Tissue was then cut half vertically, in the center of the electrode axis. The halves were labeled “1” and “2”, and for each half, we show the cut surface in the lower row. Electrodes in Panels “1” and “2” have been placed back onto endocardium and epicardium.

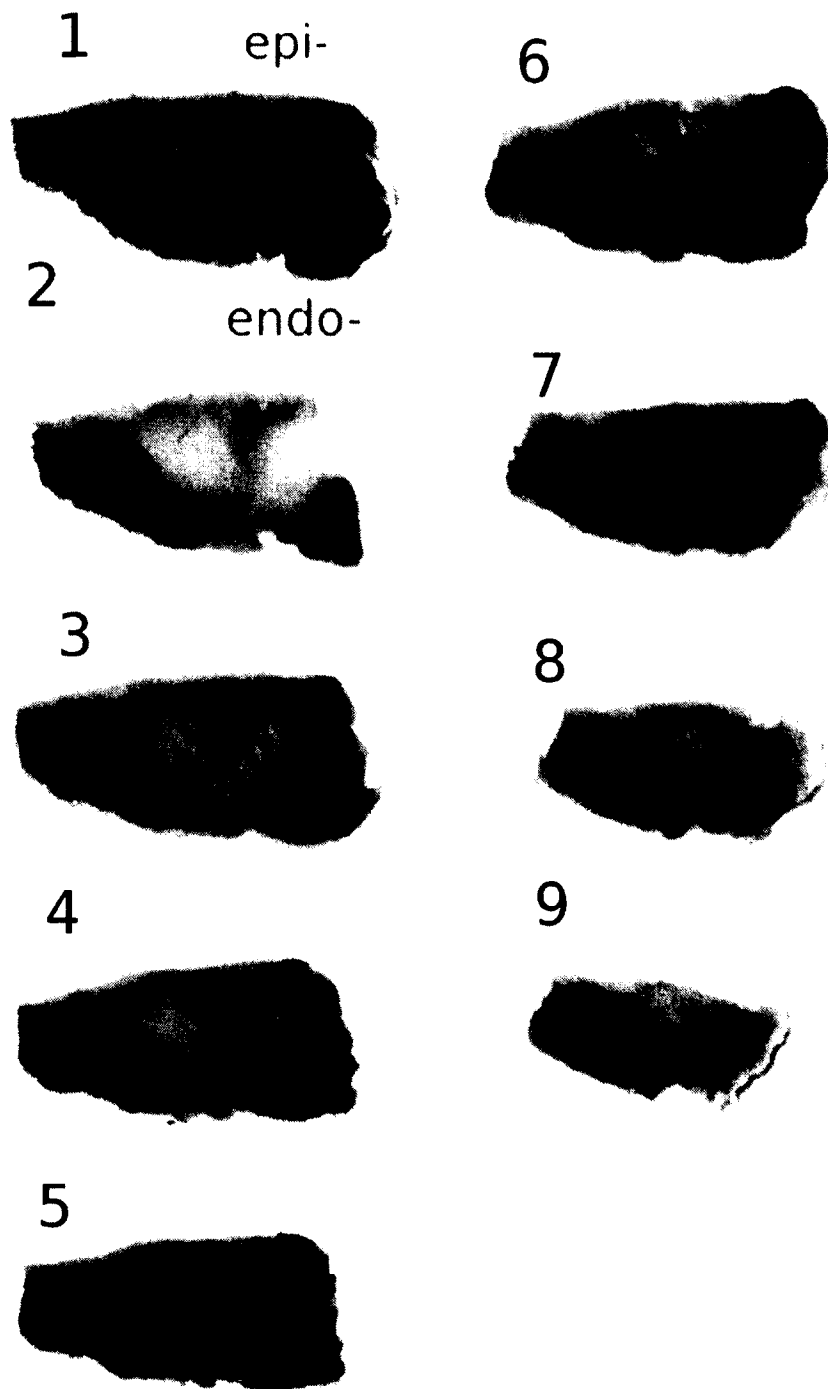


Figure 52. Sections of an ablation volume created with the endo-epi electrode configuration. Section 1 cuts through the center of the ablated volume, subsequent sections are increasingly outwards from the center. Sections are 300 μm thick. Areas stained red survived the ablation, while white regions were ablated.

3.6 DISCUSSION

Our experimental results show that nsPEFs can be used to ablate cardiac tissue and make non-conducting lesions. We have identified pulse schemes that consistently and quickly produce transmural lesions, and we are able to vary the width of the lesions within the clinically desired range (3-5.5 cm). These findings confirm our expectation that nsPEFs can overcome the major limitations of RF ablation.

Indeed, lesion geometries as those shown in Figures 47-49 and 51, show much more uniform thickness than RF ablation can achieve (compare Figure 4), and it is likely that such consistent thickness makes it less likely that the lesions later become conductive again and RF recurs. Ablation speed has been reduced from 30-60 s for RF to less than 2 s per ablation site with nsPEFs, a dramatic improvement that would reduce the overall procedure time for AF ablation from currently 4 hours to less than an hour (according to an estimate of our clinical collaborator).

Another limitation of RF ablation, the thermal side effects, has not been directly addressed in this section, but it is well known from tumor ablation that hundreds of the pulses with our characteristics are needed to warm (tumor) tissue by several degrees Celsius, so that the few pulses that we apply here should not lead to significant heating. We will address this question in more detail in the next section.

Finally, the results from this section also raise some new, interesting questions. Figures 47 and 48 clearly show that fiber organization has a decisive impact on ablation outcomes. In the following section, we want to explore this subject further in numerical simulations. Our goal is to simulate electrical field distributions for realistic tissue parameters (that mimic our experimental preparation) and to compare experimental and theoretical results. We also want to determine the critical field needed for tissue ablation and develop an understanding of how fiber organization influences the shape of the volume in which supercritical fields are reached.

CHAPTER IV

NUMERICAL SIMULATION RESULTS

Ablation effects are related to the tissue electric field distribution, and can be predicted by numerical modeling. In this chapter, we modeled rabbit heart ablation with different electrode configurations, including anisotropic twisted electric conductivities. Good matches between electric field distribution and experimental results are obtained, and the threshold electric field which lead to tissue death is also determined. Causes of the remaining discrepancies are discussed. Finally, human heart ablation results are predicted with modified models, which can provide guidelines for treatment planning.

4.1 NUMERICAL RESULTS FOR PENETRATING ELECTRODES CONFIGURATION

4.1.1 EXPLANATION OF INDENTATION OF ELECTRIC FIELD DISTRIBUTION

Based on our discussion in sections of 2.6.1 and 2.6.2, anisotropic electrical conductivities vary the local electric field distribution in the x , y and z directions; this can be related to equation (12):

$$-(\sigma_{x1} + \sigma_{y1}) \vec{i} \frac{\partial E_x}{\partial x} - (\sigma_{x2} + \sigma_{y2}) \vec{j} \frac{\partial E_y}{\partial y} - \sigma_{tz} \vec{k} \frac{\partial E_z}{\partial z} = 0 \quad (12)$$

To better illustrate how local conductivities change the electric field distribution, we assume fiber rotation equals zero, i.e, $\alpha(z)=0$, and conductivity in the z direction equals zero, i.e, $\sigma_{t,z}=0$. Thus, equation (12) becomes

$$\sigma_L \vec{i} \frac{\partial E_x}{\partial x} = -\sigma_{ty} \vec{j} \frac{\partial E_y}{\partial y} \quad (14)$$

Thus, the ratio of longitudinal conductivity to the transversal y direction determines the local field distribution. Figure 53 illustrates this by changing different value of σ_L / σ_{ty} , how the norm

local field distribution changes.

As the ratio increases from 1 to 10, the derivative of the negative electric field in the y direction increases from 1 to 10. This equation explains that the electric field change in the y-direction is much faster than in the x-direction, so the norm electric field looks compressed in the y direction, and stretched in the x direction.

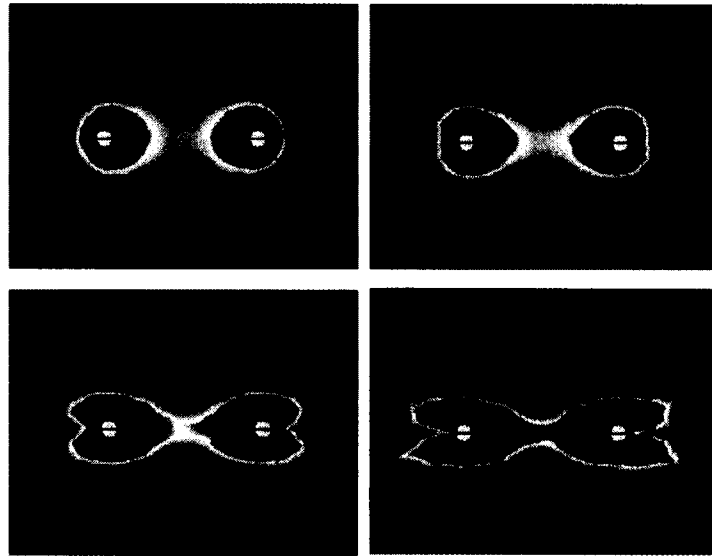


Figure 53. Electric field norm distribution changes due to different value of $\sigma_L / \sigma_{T,y}$. **Top left:** ratio=1. **Top right:** ratio=2. **Bottom left:** ratio=5. **Bottom right:** ratio=10.

The norm of the electric field is defined as

$$|E| = \sqrt{E_x^2 + E_y^2 + E_z^2} \quad (15)$$

Interesting indentations were observed around the electrodes along the x-axis. They can be explained using the panels of figure 54. In this Figure, conductivity in the z-direction has been set to zero, so the term E_z equals zero in equation (15). If the anisotropy ratio is equal to 1, the electric field is that of a regular dipole in an isotropic medium, well-known to produce a smooth norm of the electric field. When the anisotropy ratio increases to 10, the field components in the x- and y-directions are compressed in the y-direction and stretched in the x-direction (bottom panel). Because of this compression/stretch, the indentations that are always present in E_y at the x-axis

become visible in the norm of the field.

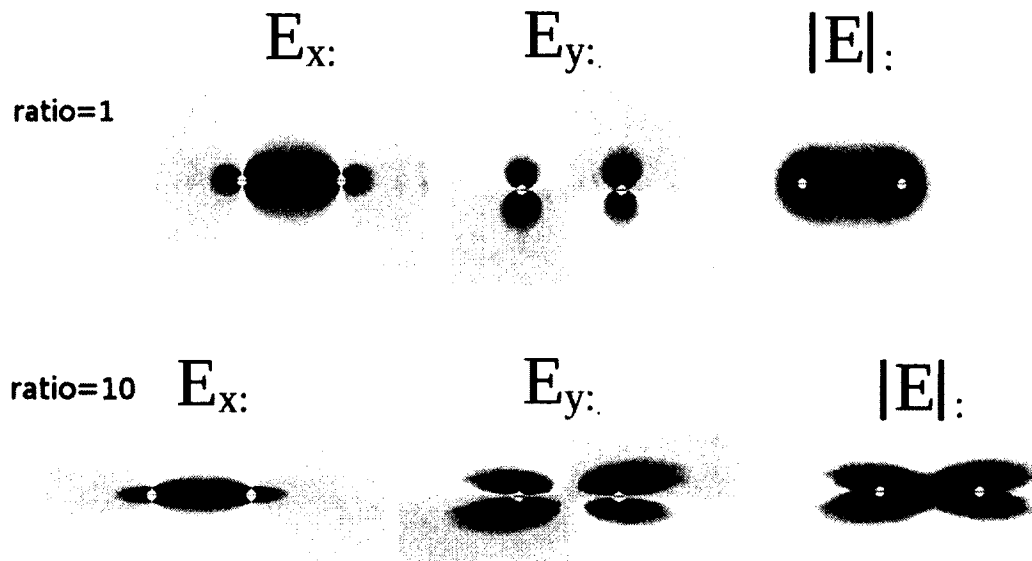


Figure 54. E_x , E_y , and the norm of the electric field for different anisotropy ratios. Blue color indicates negative field strength, while red color indicates positive electric field strength.

Due to the fact that cardiac tissue has different fiber orientations in each layer, we also need to consider the effect of twisted anisotropic conductivities. To illustrate how the fiber orientation affects the field distribution, we set the ratio of longitudinal to transversal to be 10 for 4 tissue layers, each layer with anisotropic electrical conductivities of 0° , 30° , 60° , and 90° (Figure 55). Different from the previous simulation, the different layers are now coupled, i.e. E_z is no longer zero but $E_x = E_y$. It can be seen that the electric fields are twisted, according to the fiber angle. This finding will be helpful to understand our modeling results below, in that the fiber angles change more continuously, over more tissue layers.

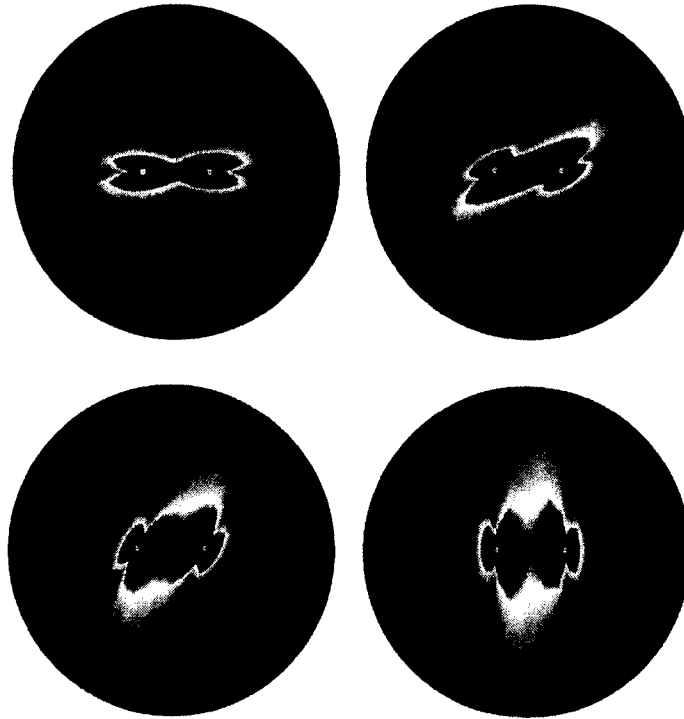


Figure 55. Illustration of local electric field distribution for different fiber orientations. Layers have fiber orientation angles (with respect to the positive x-axis) of 0° (top left), 30° (top right), 60° (bottom left), and 90° (bottom right).

4.1.2 JOULE HEATING ANALYSIS

Since Joule heating is included in our model, we can assess the temperature distribution in our tissue at the end of a pulse to exclude the possibility of unexpected thermal effects. Our result is that the shock-induced heating is minimal (see Figure 56), less than 0.2°C for all locations that are at least 100 μm away from the electrodes, and less than 1.5°C even at the node closest to the electrodes. While these results are for a single shock, a sequence of 5 shocks would result in less than five times the temperature increases and still not lead to any significant thermal effects.

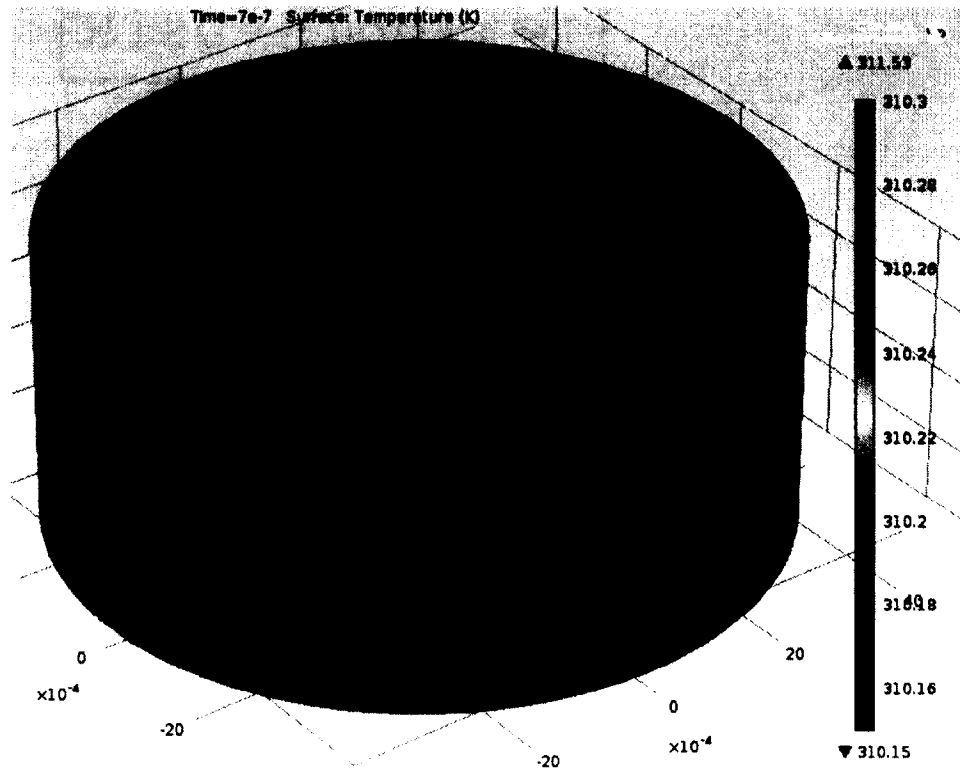


Figure 56. Temperature distribution in our model after one shock (2.3 kV, 350 ns) is applied between penetrating electrodes with 2 mm separation.

4.1.3 ELECTRIC FIELD DISTRIBUTION FOR SMOOTHLY VARYING FIBER DIRECTION

For all the numerical simulations with different electrode configurations of penetrating, endo-endo, and endo-epi, we used 40 layers, each one rotated by 2.56° compared with its neighbors (see Methods for details). The fiber orientation at the bottom layer (endocardium) was set to be 50° and that at the epicardium (after rotations through 40 layers) becomes around -50° in accordance with the experimentally measured fiber rotation in rabbit ventricles.

One crucial test for our model is whether the field distributions it predicts agree with the experimentally determined regions of dead tissue in the sense that there should be *some* critical field

strength above which tissue dies (this threshold is not a priori known). We started by comparing regions of PI fluorescence from experiments with our modeled distributions (see Figure 57) and found that a critical field of 3 kV/cm quite accurately predicts the ablated volume. The main limitation in this comparison is the accuracy of the PI stain; we show below that TTC stains give an even better agreement with simulations under the assumption that 3 kV/cm is the critical field.

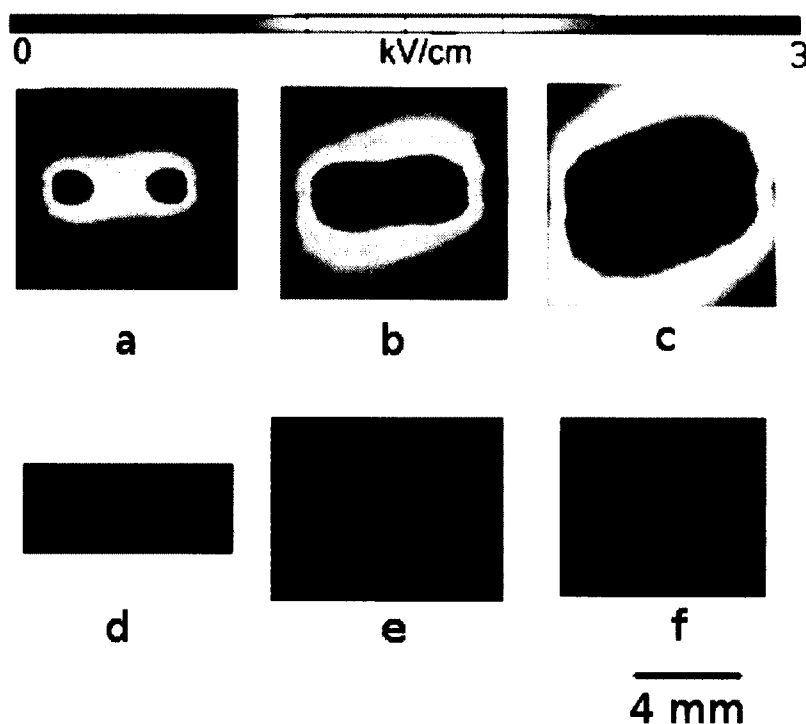


Figure 57. Comparison of theoretical simulation of electric field distribution with experimental results obtained from PI stained ablated area. Electrode spacing (a-f) is 4 mm. Amplitudes of shocks applied are 1 (a,d), 2 (b,e), and 4 (c,f) kV.

With this determined electric field strength, norm electric field distribution plotting the isosurface of 3 kV/cm is depicted in Figure 58. Electrodes are aligned in the x-axis in the upper row, and in the y-axis in the bottom row. These simulation results shows relatively uniform boundaries from the epicardium to the endocardium can be expected, no matter how we rotate the penetrating electrodes' angles. We will later see that this uniformity is due to the low ratio of longitudinal to transversal conductivity of a rabbit heart ($0.264/0.126 \approx 2$). Thus, the norm of the electric field in each layer

does not vary much in the x- and y-directions, so the difference of electric field distribution contours between x and y axis electrodes alignment does not vary too much. The transmural ablated volume in the yz-plane shows a more uniform cross section of the ablated volume than the elliptical profile obtained by RF ablation in Figure 3.

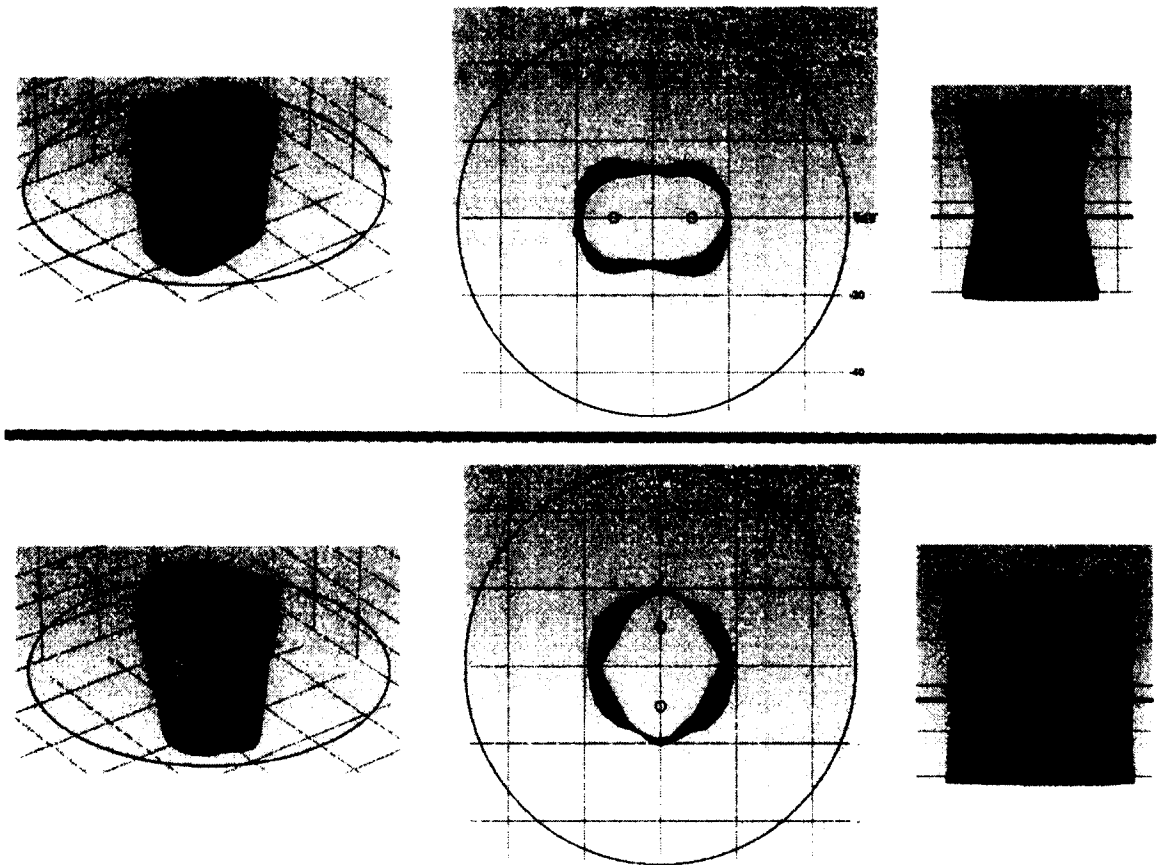


Figure 58. Isosurface of electric field strength ($E= 3 \text{ kV/cm}$) induced in tissue with twisted anisotropy with electrodes aligned in x-axis (upper row) and y-axis (bottom row). The electrodes appear as a pair of circles in the middle column (aligned horizontally in the top row and vertically in the bottom row). The amplitude of the pulses are set to 2.3 kV in order to compare the results to experimental ones. Left column: oblique view. Middle column: xy-plane. Right column: yz-plane.

4.1.4 COMPARISON OF NUMERICAL AND EXPERIMENTAL RESULTS FOR PENETRATING CONFIGURATION

By superimposing the numerically determined isosurface for 3 kV/cm onto the stained

histological sections, we can compare theoretical predictions and experimental measurement of the ablated tissue in all of our sections. For our simulations, parameters of tissue and electrodes geometry are chosen to be the same as in our experimental setup, in order for the comparison. Figures 60 and 61 show an excellent match of experimental results and theoretical predictions.

In Figure 60, the fiber direction in the different sections can be seen by the naked eye, and it changed little from epicardium to endocardium (by less than 45 degrees). The fibers are approximately in field direction in all sections. Since the upper row in Figure 58 predicts a very consistent cross-section of the ablated volume in all layers, we chose to use the xy-projection of the 3 kV/cm isosurface (top middle panel in Figure 58) and to superimpose it onto the sections in Figure 60, aligned with the fiber direction at the electrode position.

The resulting match in Figure 60 is nearly perfect. In Figure 61, the match is also close, but the limited quality of the PI stain does not allow a comparison in as much detail as in Figure 60. The remaining discrepancies between numerical and experimental results, may be due to either errors in our experimental measurement and or errors in the numerical model. Shortcomings of the model will be discussed in section 4.5. Errors from experimental measurement include: 1) PI staining measurement inaccuracy, as discussed; 2) sectioned tissue might get stretched during the sectioning process or when placed onto glass slides; 3) sometimes dead tissues were over-stained or under-stained with the PI or TTC dye, for example due to heterogeneities in the target tissue, such as blood vessels (see Figure 59) or fibrous tissue that affected the local field distribution. In these circumstances, local dead regions might vary to a certain degree from expectations; 4) sometimes the location of penetrating electrodes happened to encounter an uneven endocardial surface (see Figure 59), that might change the local field distributions.

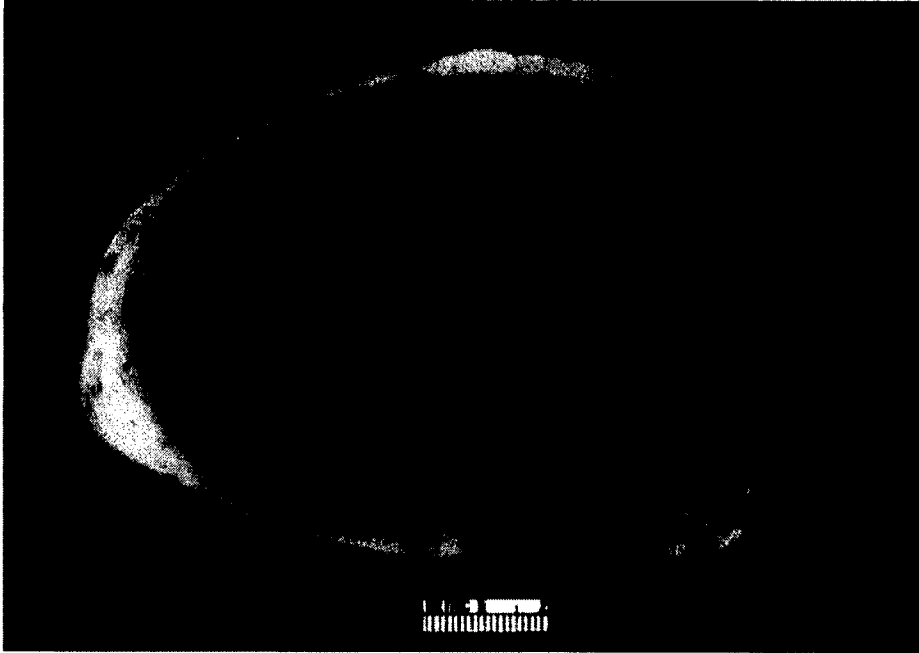


Figure 59. Cross section of a mammalian heart. Left ventricle is on the left ⁹⁰.

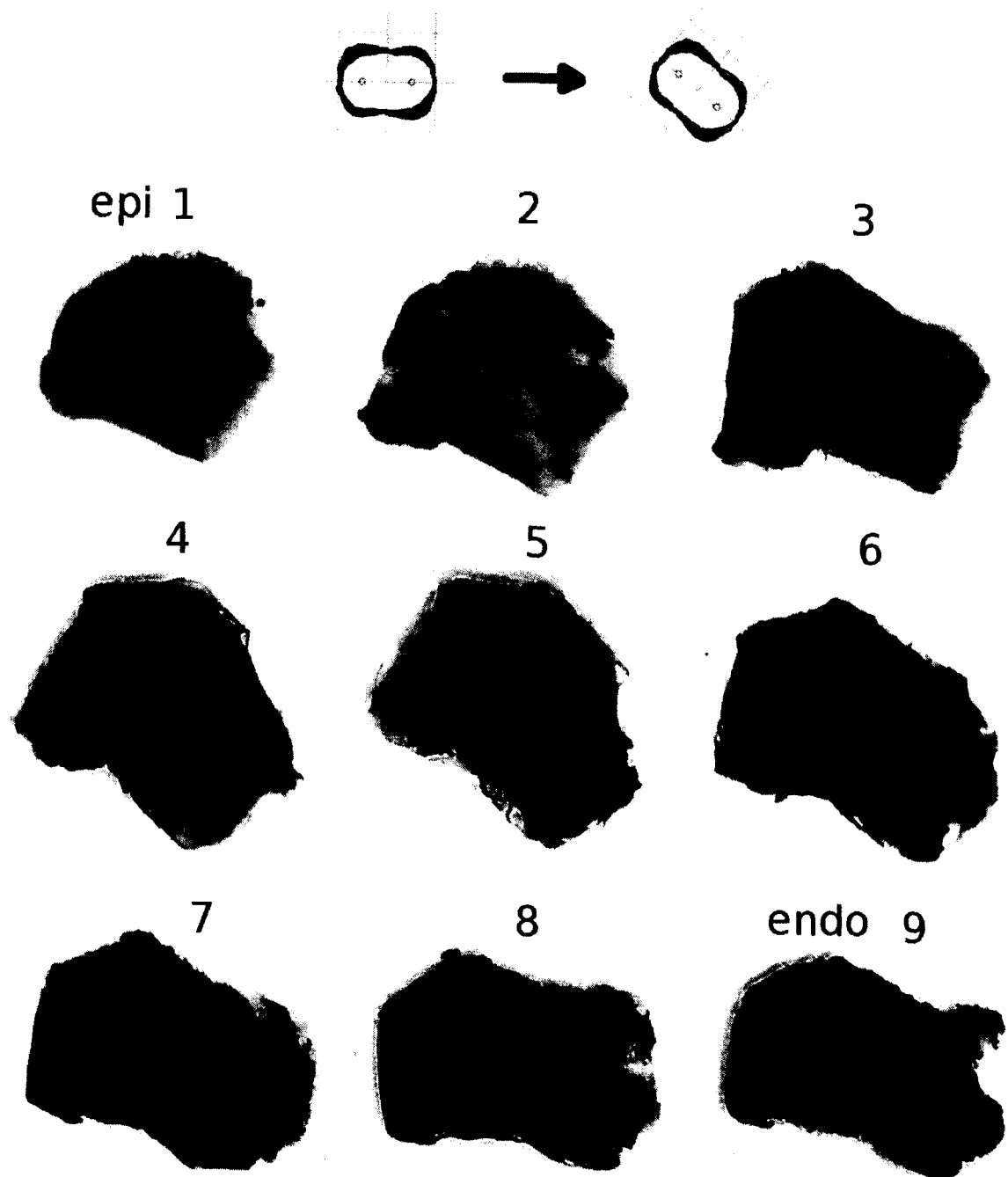


Figure 60. Superposition of the projection of the isosurface of electric field strength ($E= 3$ kV/cm) from numerical model (green) onto sectioned TTC stained tissue ablated by 2.3 kV, 5 pulses at 3Hz with 2 mm spacing, from epicardium to endocardium. The green boundary has been rotated to match the field direction (defined by the electrode positions) in each layer.

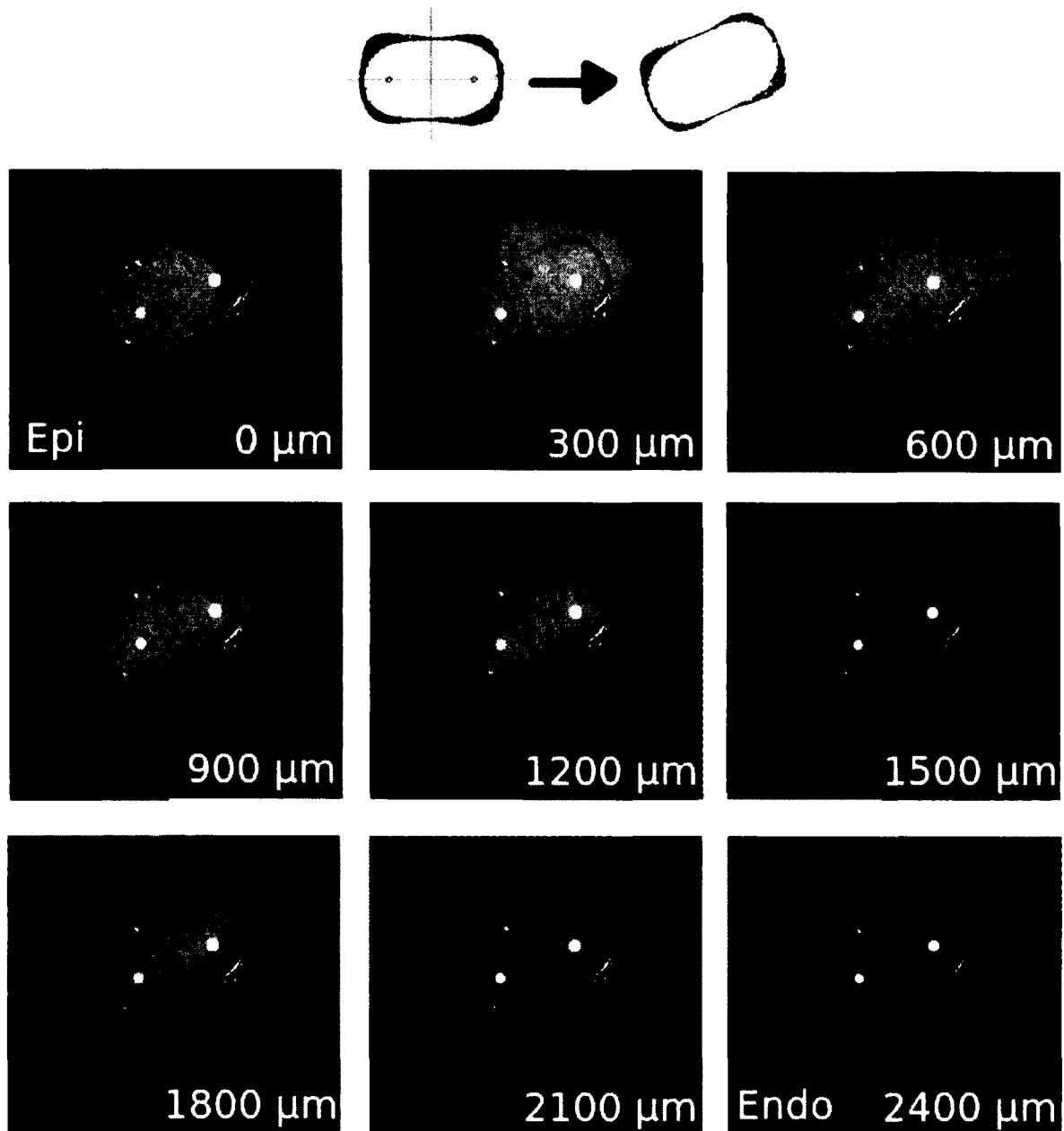


Figure 61. Superposition of the projection of the isosurface of electric field strength ($E = 3$ kV/cm) from numerical model (red) onto sectioned PI stained tissue ablated by 4kV, 20 pulses at 1Hz with 4 mm spacing, from epicardium to endocardium. The red boundary has been rotated to match the field direction (defined by the electrode positions) in each layer.

4.2 ENDO-EPI AND ENDO-ENDO CONFIGURATIONS

Endo-epi

The endo-epi configuration does not require piercing the tissue with electrodes, and the fact that electrical fields are applied transversal to fiber direction (independently of how the fiber direction changes across the wall) suggests that it will be less sensitive to fiber twist. Figure 62 shows the model geometry and the 3 kV/cm isosurface for a 6.5 kV pulse. Panels B through D show a very uniform transmural geometry that is very well suited for the construction of uniform lesions.

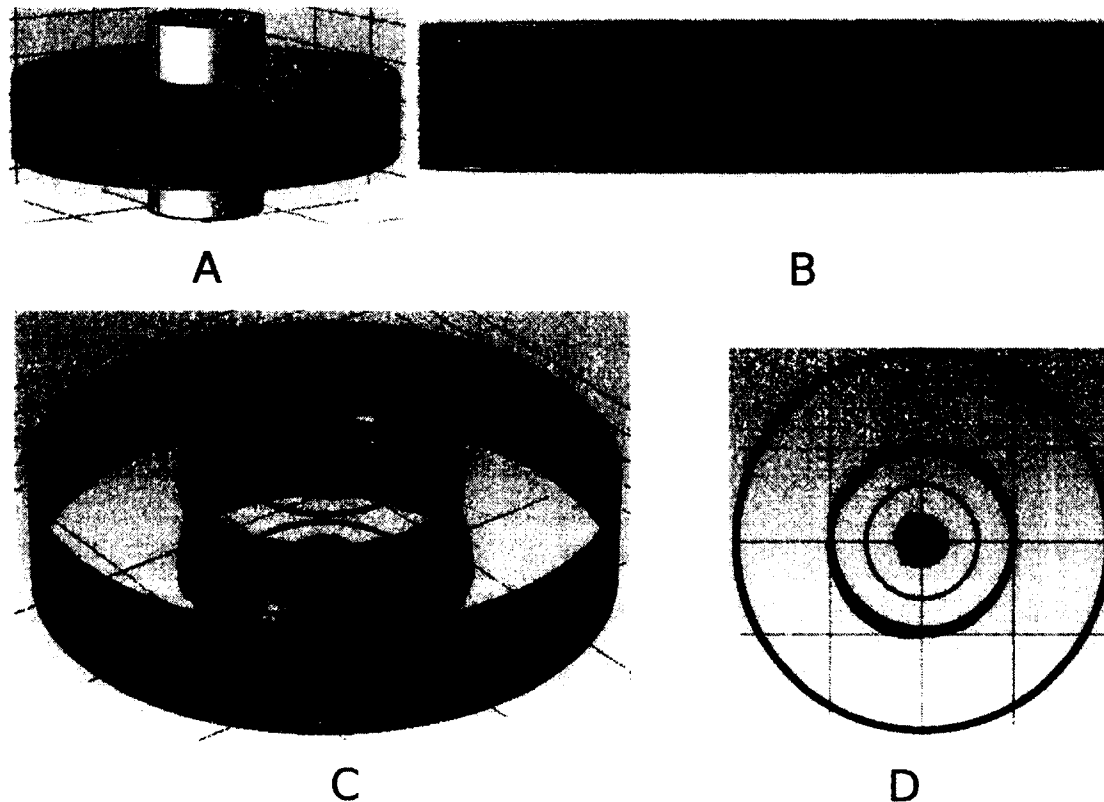


Figure 62. Isosurface (3 kV/cm) plotting of electric field distribution for 6.5kV shocks applied with the endo-epi electrode configuration. The two cylinders at the bottom and the top of the tissue in Panel A are electrodes, each with a radius of 3mm. Material parameters are the same as the one using penetrating electrodes. Panels B, C, and D show the yz-projection, an oblique view, and the xy-projection of the ablated volume. The positions of electrodes are marked with circles in Panels C and D.

Endo-Endo

Compared to the other two nsPEFs electrode configurations, the endo-endo configuration is the most straightforward to implement; existing RF ablation catheters could be used with small modifications. Figure 63 shows the model geometry (Panel A) and simulation results. The plot of the 3 kV/cm surface shows that transmural ablation can be achieved, although only for a relatively high pulse amplitude of 9 kV. Panels A, B, and D show that the cross section of the ablated tissue is not as uniform as for the endo-epi configuration. The main disadvantage of using this configuration is, however, that the pulse amplitude required for transmural ablation increases sharply with the tissue thickness, so that ablation of thicker tissues becomes impractical.

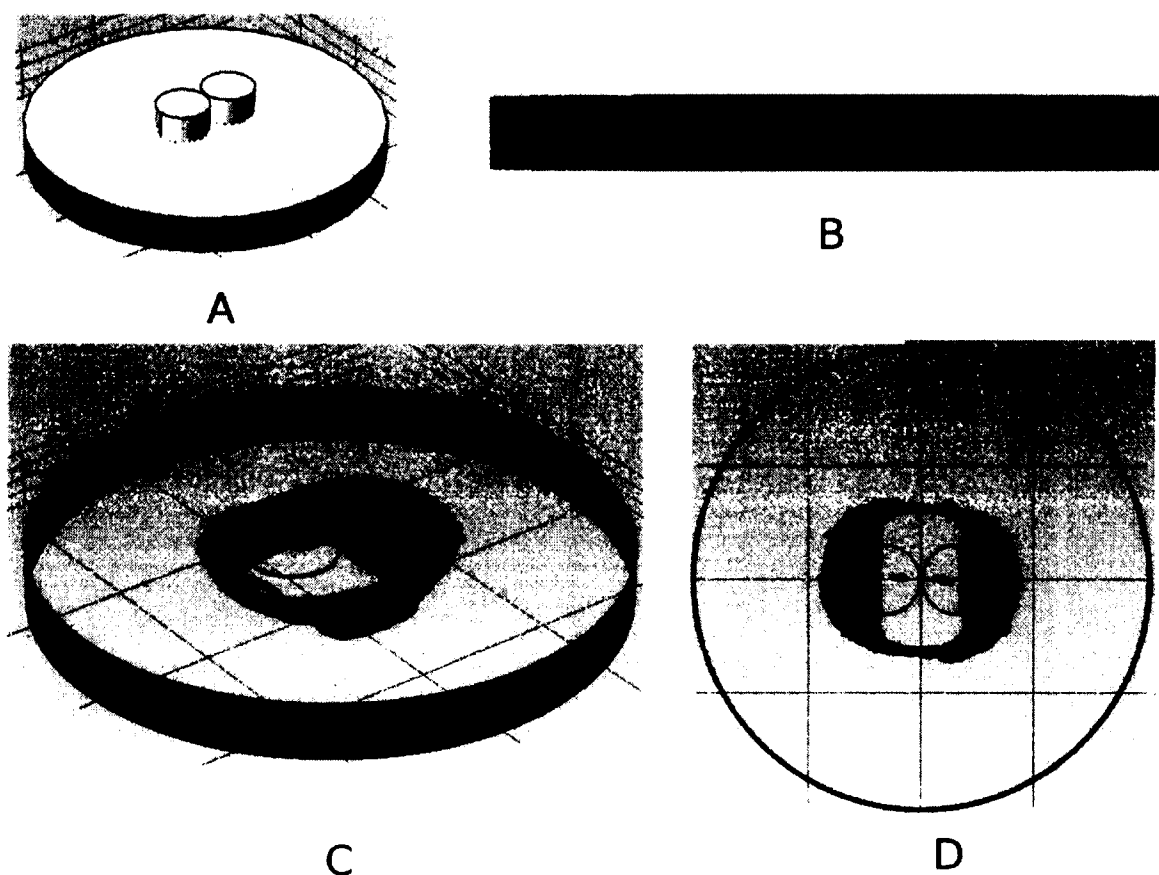


Figure 63. Isosurface (3 kV/cm) plotting of electric field distribution with 9kV shocks applied for Endo-endo electrodes configuration. Two circles (panel C) are electrodes, each with the radius of 3mm and 0.2 mm spacing. Material parameters are the same as the one using penetrating electrodes. Panels B, C, and D show the yz-projection, an oblique view, and the xy-projection of the ablated volume. The position of electrodes are marked with circles in Panels C and D.

4.2.1 COMPARISON OF NUMERICAL AND EXPERIMENTAL RESULTS FOR ENDO-EPI CONFIGURATION CONFIGURATION

To evaluate the accuracy of our model's predictions for the endo-epi configuration, we again superimpose the isosurface for 3 kV/cm onto our experimentally determined ablated volume (as in Figures 60 and 61). The results are shown in Figure 54. Remarkably, the diameter of the predicted ablated volume very closely matches the experimentally determined one, and the match in shape is likewise very close.

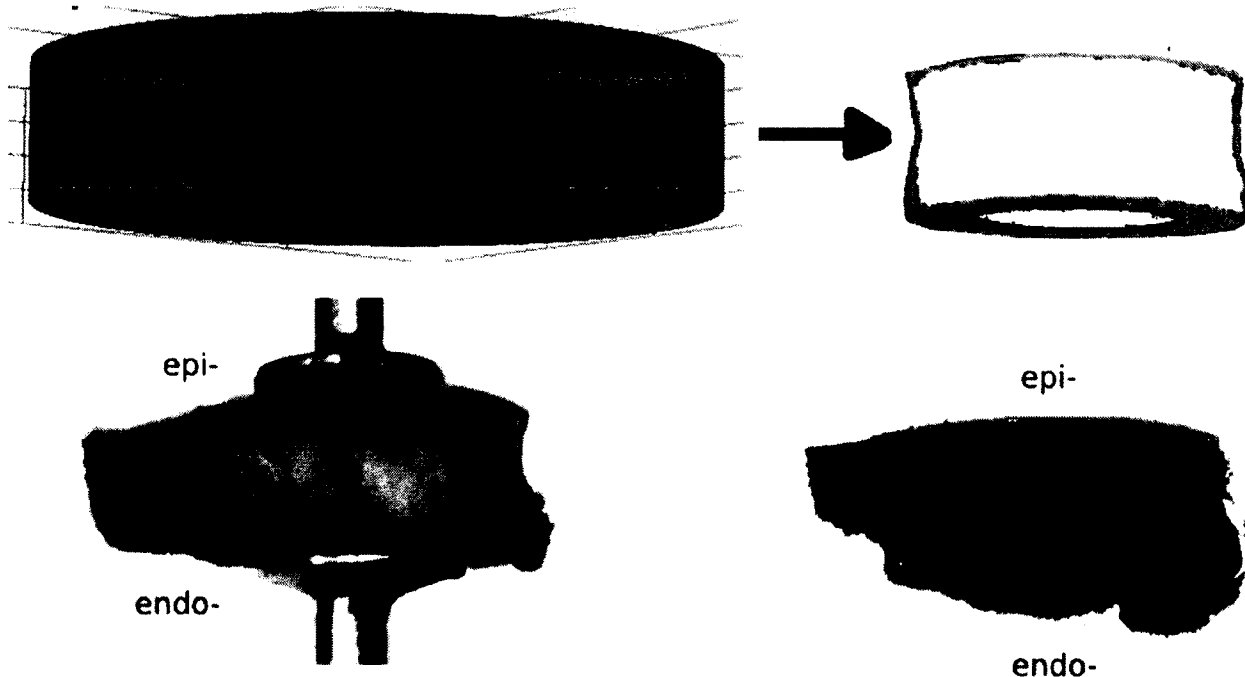


Figure 64. Superposition of critical electric field of 3 kV/cm with same electrode radius from numerical simulation onto the experimental results from Figure 51 and 52. Top row: Ablated volume and extracted outline. Bottom Row: Outline superimposed over Panel 1 of Figure 51 and Panel 1 of Figure 52.

4.3 NUMERICAL MODELING FOR HUMAN LEFT VENTRICLE ABLATION

So far we have shown that our hypothesis of 3kV/cm critical electric field for ablation in our numerical models is consistent with experimental results we obtained in rabbit hearts. It is

reasonable to assume that a similar ablation threshold applies to human cardiac tissue. In this section, we will explore how the specific properties of human cardiac tissue affect simulation results, and how our model can be used as a guideline to predict future nsPEF ablation treatment for humans. We consider both the case of human left ventricle ablation and human atrium ablation.

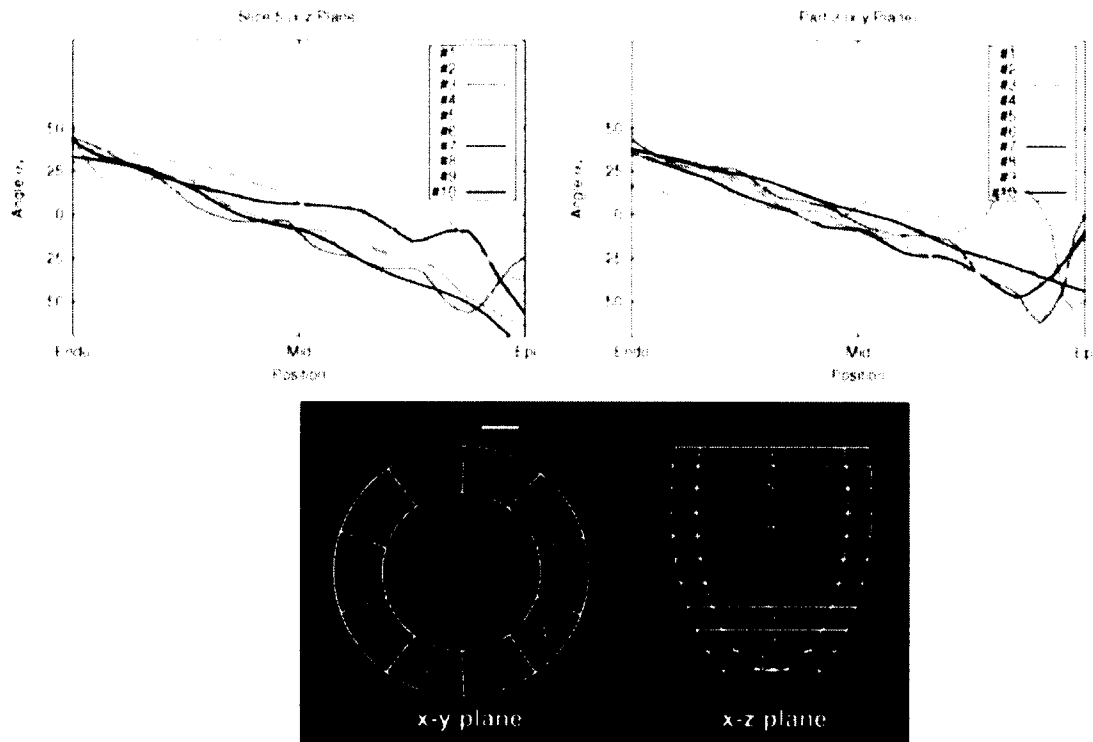


Figure 65. DTMRI-acquired fiber orientation at different subdivisions in the left ventricle⁶⁹. Bottom panel: Schematic diagram of left ventricle subdivisions. It is subdivided into 10 parts in the x-y and into 10 slices in the x-z plane. The red-colored subdivisions are part of the septum (9, 10, 1, 2). Top left: α_{helix} in slice 5 of the x-z plane at all corresponding x-y segments. Top right: α_{helix} in part 3 of the x-y plane at all x-z segments.

The main physiological difference between humane and rabbit cardiac architecture are that the cardiac anisotropy is more pronounced in humans, with a longitudinal conductivity of 0.2 S/m, a transversal 0.02 S/m, and an anisotropy ratio of 10 (see ⁸⁰). Besides, anatomical models of the human ventricles constructed using diffusion tensor (DT) MRI data suggest that the change in fiber orientation is larger across the cardiac wall, and that the helix angle (α) changes from -75°

(epicardium) to 60° (endocardium)^{81, 69}, a larger change than for the rabbit heart. Figure 65 illustrated the DTMRI acquired fiber orientation of α at different subdivisions in the left ventricle. The main reason to choose left ventricle for the simulation is that it is thicker than right ventricle, which makes the ablation more challenging. Normally, the thickness of left ventricle of human heart is around 10 mm⁸².

With these parameters, we performed simulation of the electric field distribution for the penetrating electrode configurations (Figure 66). Panel A shows the model geometry, and Panels B-D different views of the ablated volume. Due to high anisotropy ratio, the varying fiber orientation leads much greater changes of the ablated cross section across the wall (compare Figure 66 to Figure 58). The geometry of the ablated volume suffers from deficiencies similar to those of RF ablation volumes: To obtain lesions that maintain a certain minimum width everywhere, much more tissue needs to be sacrificed in other places.

Fortunately, endo-epi ablation is much less affected by varying fiber direction and high anisotropy ratio (see Figure 67). Panel A shows the model geometry, and Panels B-D views of the ablated volume that demonstrate that the cross section of the ablated volume can be kept close to constant for an adequate pulse amplitude (4.1 kV).

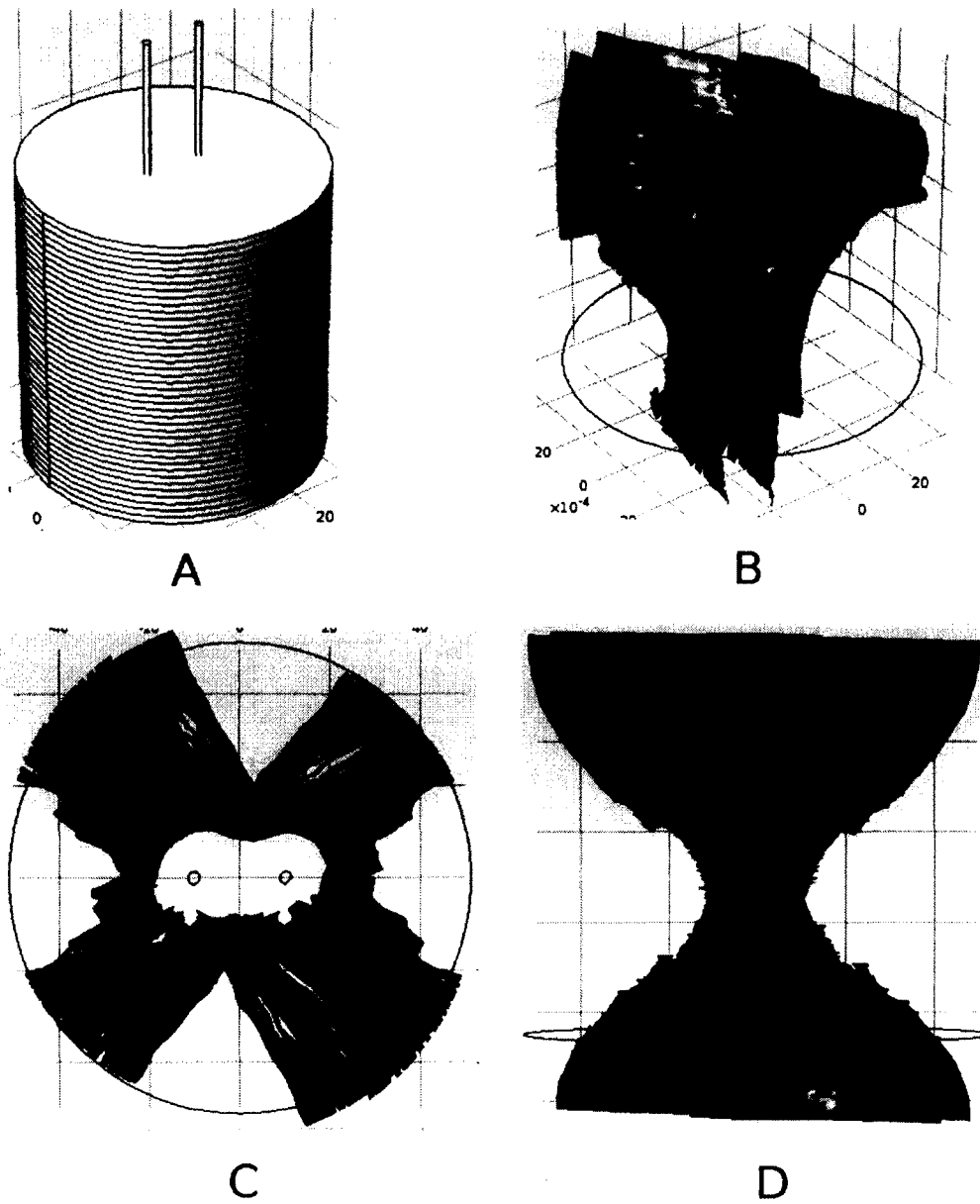


Figure 66. Isosurface (3 kV/cm) for 2.3 kV shocks applied with the penetrating electrodes configuration. Panel A shows the geometry of tissue with 10 mm thickness (40 layers). Panels B, C, and D show an oblique view, the xy-projection, and the yz-projection of the ablated volume.

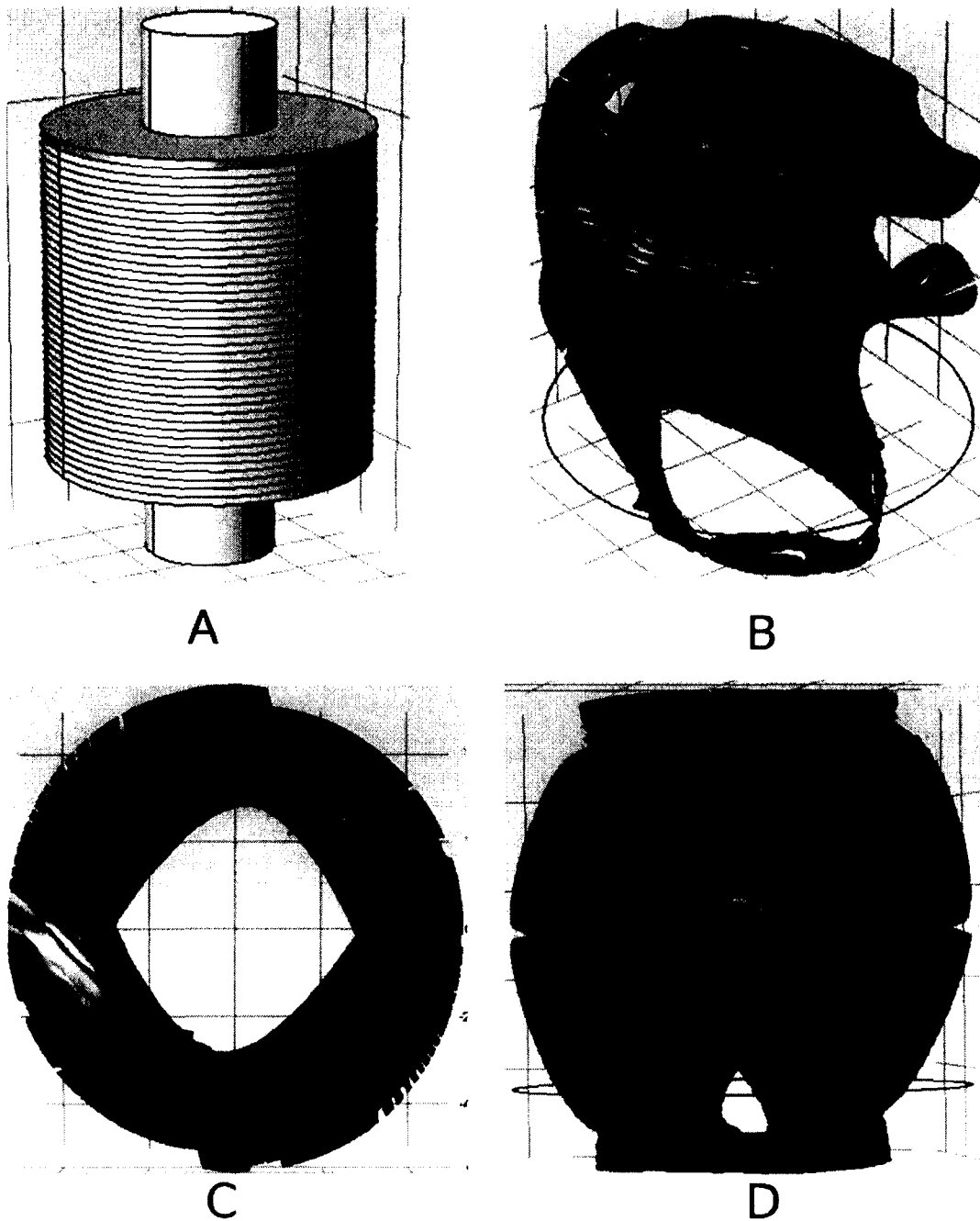


Figure 67. Isosurface (3 kV/cm) for 4.1 kV shocks applied for endo-epi electrodes configuration. Both radii of electrodes are 2 mm . Panels B, C, and D show an oblique view, the xy-projection, and the yz-projection of the ablated volume. Note that the isosurface intersects the boundaries of the medium, these intersections lead to holes in the isosurface in COMSOL's rendering.

4.4 NUMERICAL MODELING FOR HUMAN ATRIUM ABLATION

Compared with the left ventricle, the atrium is much thinner, and there is less variation in fiber orientation. There are, however, some abrupt changes in fiber orientation in some parts of the atrium (see Figure 68). The anisotropy ratio is similar to that of human ventricles.

To represent these jumps in fiber orientation in our model, we created 3 different layers in our medium (each 1 mm thick). From epicardium to endocardium, the fiber orientation in these layers are 0° , 45° and 90° .

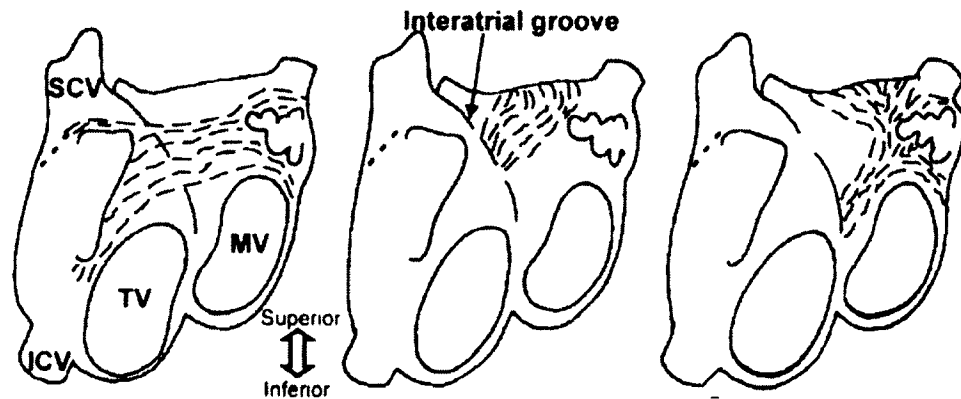


Figure 68. Schematic diagram of serial dissections from subepicardium to subendocardium (left to right) in the left atrium to display the atrial myoarchitecture in a normal human heart ⁹⁷. Broken lines highlight the major orientations. TV standard for tricuspid valve, MV for mitral valve, superior (SCV) and inferior caval veins (ICV).

Ablated volumes for penetrating and endo-epi configurations were then modeled as previously described. The results for the penetrating electrodes configuration are shown in Figure 69. Transmural ablation can be achieved with a pulse amplitude of 1.8 kV/cm, but as in the case of ventricular simulation, the high anisotropy ratio combined with significant fiber twisting results in a geometry of the ablation volume that has very different widths in different depths and therefore creates the now familiar conflict that too much tissue needs to be ablated to assure an consistent minimum thickness in the lesions. The endo-epi configuration again leads to much more uniform

lesions. As Figure 70 shows, a 2.3 kV pulse ablates a volume of approximately constant cross section.

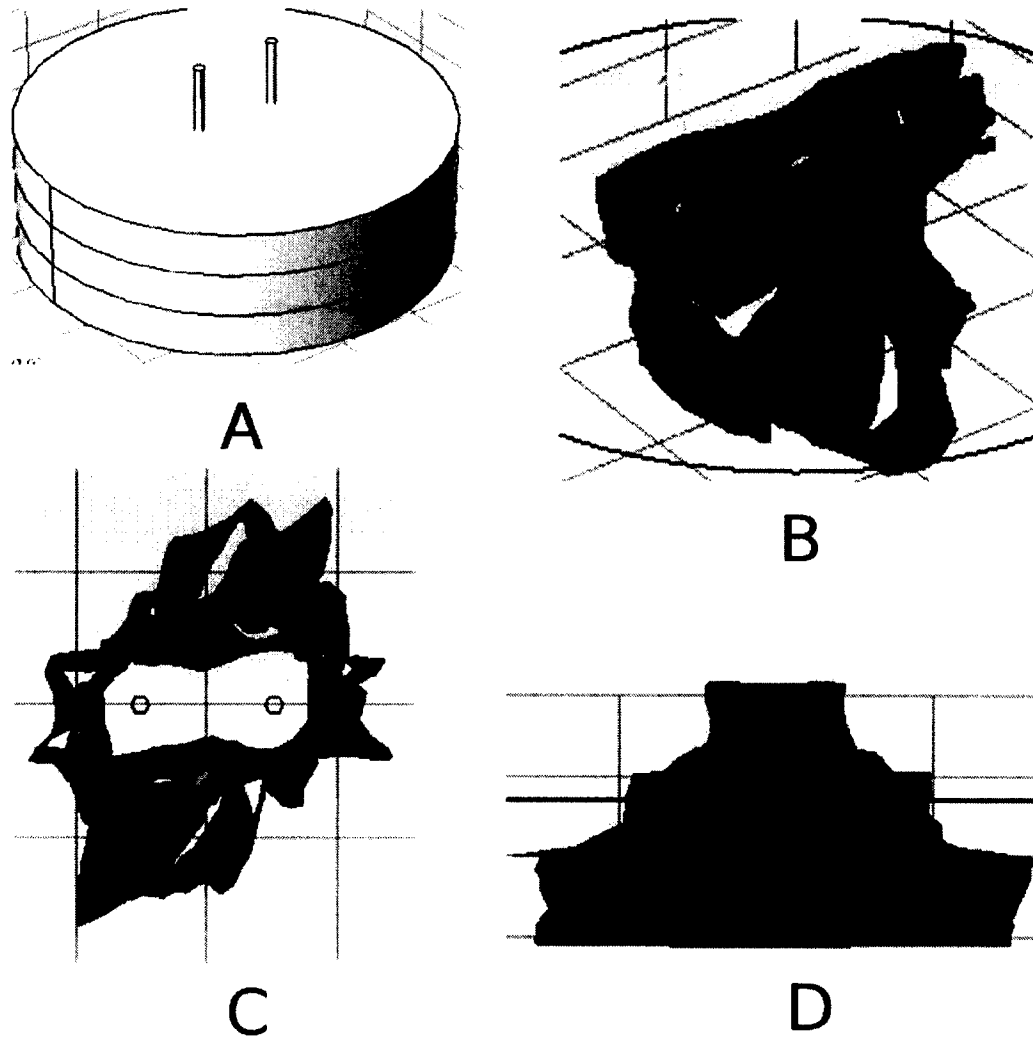


Figure 69. Isosurface (3 kV/cm) for 1.8 kV shocks applied for penetrating electrodes configuration. Panel A shows the geometry of tissue with 3 mm thickness (3 layers). Panels B, C, and D show an oblique view, the xy-projection, and the yz-projection of the ablated volume.

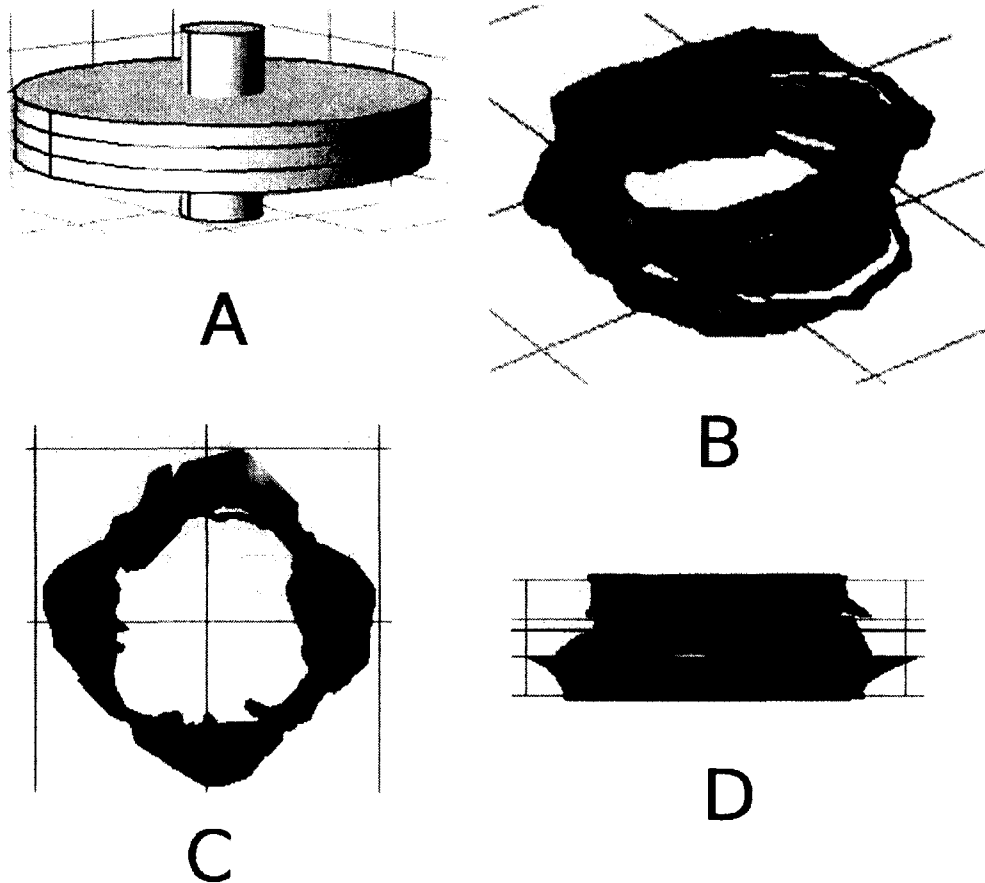


Figure 70. Isosurface (3 kV/cm) for 2.3 kV shocks applied for endo-epi electrodes configuration. Electrodes have a radius of 2 mm. Panels B, C, and D show an oblique view, the xy-projection, and the yz-projection of the ablated volume.

4.5 LIMITATIONS OF OUR NUMERICAL MODEL

While our results from numerical modeling match most of our experimental results, there is at least one important known effect of nsPEFs that are not included and that deserves some discussion, i.e. membrane permeabilization. Several studies have found that electrical conductivity is dynamic and will change in response to the pulsed electric fields⁸³. This means that the measured electrical conductivity of tissue may increase after the application of electroporation pulses or in between the application of multiple pulses, rather than being constant^{84, 50}. The main reason for such changes is that pore formation improves electrolyte mobility through the cell, increasing bulk tissue

conductivity^{85, 86}. Due to the fact that electrical conductivities are not constant after IRE treatment, the electric field distribution will change accordingly.

In particular, experiments by Neal et al. show that the conductivity of swine kidney changes in response to a single applied pulse with different pulse width⁸⁶. The electrical conductivity of the tissue samples was calculated from measured current and voltage data, shown in Figure 71. As electric field strength goes up, electric conductivities increase. It is also noticed that the pulse width affects the change of conductivity: a wider pulse leads to higher conductivity given a certain electric field.

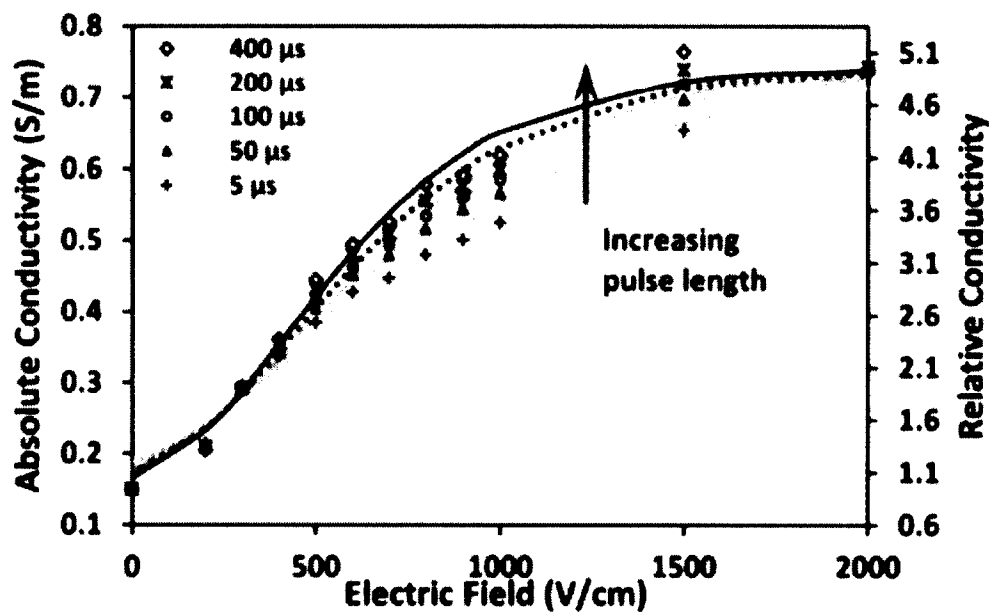


Figure 71. Electrical conductivity versus electric field with different pulse widths at $24 \pm 2 \text{ }^\circ\text{C}$ ⁸⁶. Asymmetric Gompertz fits for $\sigma(E)$ are shown as dashed lines.

In the model by Neal et al., a modified asymmetrical Gompertz curve was chosen to fit all the experimental results

$$\sigma(E) = \sigma_0 + (\sigma_{\max} - \sigma_0) \cdot \exp[-A \cdot \exp(-B \cdot E)], \quad (16)$$

where σ_0 is the baseline conductivity without IRE treatment and σ_{\max} is the maximum (fully

saturated) conductivity for thoroughly permeabilized cells within a single pulse. E is the electric field in V/cm, and A and B are unitless coefficients that vary with pulse width and need to be determined by best fitting the curve with experimental data (dashed line in Figure 71). Different tissues may have different curve shapes, so A and B coefficients need to be adjusted by experimental data accordingly. A characterization of conductivity changes for cardiac tissue following the methodology of reference⁸⁶ would make our model more predictive.

Besides the missing membrane permeabilization, our model also omits many details of the structure of cardiac tissue, such as the presence of large blood vessels, which affects the electric field distribution due to a different value of conductivity⁵⁰, or the detailed geometry of the tissue, which we assume to be flat. Inclusion of such structural details would greatly increase the complexity of our model and are probably not justified at this point, since it does not seem feasible to obtain detailed structure information in a clinical setting, and our model predictions closely match experimental results even without such detail.

4.6 DISCUSSION

We have developed a detailed model of electric field distribution in cardiac tissue that includes anisotropic conduction and the variable fiber direction. Figures 60, 61, and 64 show a remarkable agreement of our model results with experimental results and strongly suggest that the critical field needed to ablate cardiac tissue is close to 3 kV/cm.

Yet, the model does not only confirm what we know from our experiments; it also makes two important predictions that will guide our future experimental work. First, it predicts that in species with a higher anisotropy ratio ($\sigma_L / \sigma_{T,y}$), which includes humans, the penetrating electrode configuration will lead to ablation geometries that are oblong in every layer, with an orientation that varies across the cardiac wall as the fiber direction varies. Such a geometry may severely limit the usefulness of the penetrating electrode configuration because it requires high fields to maintain

some minimum lesion thickness in all layers. Such high fields will lead to unnecessarily wide lesions in other layers (similar to the case of RF ablation).

At the same time, our model also predicts that the problems with lesion geometry in the penetrating electrode configuration do not appear in the endo-epi configuration. This, in combination with the very promising experimental results for the endo-epi configuration (Figures 51 and 52), justifies optimism regarding the clinical potential of nsPEF ablation.

Before nsPEF ablation has a chance to be tested in a clinical trial, it will have to be tested in larger animals. Guided by our present results, we will choose a species that has an anisotropy ratio that is high similarly high to that of humans (most likely pigs), and expect problems with penetrating electrodes but good results for the endo-epi configuration. If we indeed obtain these results, we would have a strong argument that humans, too, may benefit from nsPEF ablation.

CHAPTER V

CONCLUSIONS AND FUTURE WORK

Irreversible electroporation is a new technique to kill cells in targeted tissue through a non-thermal mechanism using electric pulses that irreversibly permeabilize cell membranes. In this project, we successfully ablated myocardial tissue using IRE-based nsPEFs delivered by different configurations of customized electrodes. This chapter will summarize our conclusions and clarify the directions for our future research on nsPEF ablation.

5.1 CONCLUSIONS

- It has been verified experimentally by optical mapping and PI / TTC staining that nsPEFs can effectively and transmurally ablate cardiac tissue with penetrating and endo-epi electrode configurations. Single ablation can be achieved in less than 2 seconds, much faster than conventional RF ablation. Tissue sections suggest that a sharply defined and transmurally uniform ablated volume can be achieved, better than the elliptical shape from RF ablation. This better controlled ablated volume from epicardium to endocardium reduces the risk that lesions are too thin in some regions, so the treatment of atrial fibrillation should be more reliable. Besides, due to the mechanism of ablation, which is based on electroporation rather than thermal effects, there are no thermal side effects such as thrombus or char formation.
- For the penetrating electrodes configuration, the most common method in this project for pulse delivery, average width of ablated tissue of 3 mm can be achieved, by pulse a amplitude of 2.3 kV, with 5 pulses at the frequency of 3 Hz. By repeating a series of single ablations along a line, lesions were successfully created to block the propagation of action potentials.
- For the endo-epi electrodes configuration, sectioned tissue shows transmural ablation was

also successful, with a pulse amplitude of 6.5 kV and 6 pulses at the frequency of 3 Hz. This configuration requires less modification of the current RF ablation catheter than penetrating electrodes.

- The ablated region is related to the local electric field distribution inside the tissue, which can be predicted with numerical modeling. Finite element models were created using COMSOL Multiphysics to demonstrate the impact of anisotropic conductivities on the electric field distribution. We used twisted anisotropic conductivities in different layers of the tissue, as they are present in cardiac tissue. By superimposing the electric field distribution contours onto the dead region of experimental ablated tissue, the critical field required to ablate the cardiac tissue was determined to be 3kV/cm for nsPEF ablation. It is found that this critical field leads to good predictions of the ablated volume for the penetrating and endo-epi electrode configurations.
- Assuming the critical electric field for human heart ablation is the same as for rabbit hearts, we modified the model with human heart parameters for human atrium and ventricle ablation. It is predicted that for the penetrating electrodes configuration, the ablated volume in the human heart would have less uniform transmural geometry compared to the rabbit heart, due to the higher ratio of longitudinal to transversal conductivity in the human heart. For the endo-epi configuration, however, an approximately uniform transmural geometry could be achieved. These numerical simulations can function as a guideline for future human cardiac tissue ablation to a certain degree. For a precise IRE treatment planning, however, these models need to be improved. We will discuss this improvement in the following section.

5.2 FUTURE WORK

Although experimental and numerical results are encouraging and promising for this nsPEF

ablation, there are still many steps needed to bring nsPEF ablation into clinical practice. Essential steps include animal studies in large animals, long-term animal studies to test whether nsPEF-induced lesions remain non-conductive for a long time, and the development of a catheter-based delivery system for nsPEFs. Of these essential steps, we plan to perform large animal studies and long-term animal studies, while catheter development will be done in collaboration with an experienced company if the results from large animal studies and long-term studies justify the expense. Since our lab also has a strong interest in the mechanisms of nsPEF, we further plan ablation experiments in which we vary the pulse duration, particularly towards shorter shocks, and to refine our model to include shock-induced membrane permeabilization. Finally, we are currently collaborating with a company that produces ablation systems for concomitant ablation during open heart surgery. These ablation systems are not catheter based (since direct access to the heart is available), but use clamps that have electrodes on each jaw (see Figure 73) and can create applied currents along the whole length of the clamp in one step to quickly create linear lesions. Currently, these ablation clamps are used for RF ablation, but there is strong interest in testing their suitability for nsPEF ablation. In terms of the electrode configurations we have discussed so far, these ablation clamps perform endo-epi ablation, with linear rather than circular electrodes. Our promising results for endo-epi nsPEF ablation in Section 3.5 strongly suggest that this approach is viable.

The next steps that we plan to take are 1) the extension of our model to include membrane permeabilization and 2) the testing of endo-epi/endo-epi ablation with ablation clamps. These two steps can be performed in relatively little time, and they don't require extensive resources, as the large animal studies and long-term animal studies will. Below we give a more detailed description of our plans.

5.2.1 INCLUSION OF MEMBRANE PERMEABILIZATION INTO NUMERICAL MODEL

As we discussed in last chapter, nsPEFs will change tissue properties such as the conductivity because they create pores in the cell membranes. Because conductivities are not constant during and after IRE treatment, the electric field distribution will change accordingly. Such changes would be important to better predict the electric field distribution. Some electroporation devices monitor not only the voltage but also the current being applied, which can be used to measure the bulk conductivity of the tissue⁵⁰. To improve our numerical model, we plan to measure conductivities experimentally during the pulse schemes that we typically apply. Figure 72 shows a simple example of a four-electrode technique to measure the conductivity, in which two electrodes inject current and two other electrodes measure the potential. This method is used to measure the electrical properties of skeletal muscle by Gielen et al^{87, 88}.

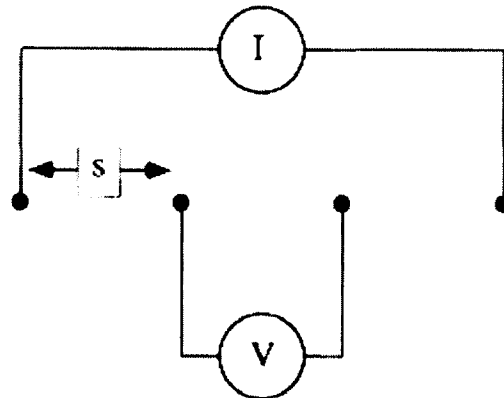


Figure 72. Schematic diagram of the four-electrode technique for measuring tissue conductivities. Current (I) is passed through the outer two electrodes, and the potential, V , is measured between the inner two electrodes⁸⁸.

Due to the fact that cardiac tissue has a myofiber structure that strongly affects the conductivity, separate longitudinal and transversal measurements of conductivities are required. Conductivity of each longitudinal and transversal measurement can simply be calculated as:

$$\rho(t) = R(t) \cdot K = R(t) \frac{SA}{L} = \frac{V(t) \cdot SA}{I(t) \cdot L} = \frac{1}{\sigma(t)} \quad (17)$$

where $\rho(t)$ is the electrical resistivity, $\sigma(t)$ is electrical conductivity, L is the tissue thickness, and SA is the surface area of the tissue (K is a tissue constant).

It is proposed that by varying the amplitude of pulses applied, a similar experimental relationship between measured conductivities and amplitude of pulses (and number of pulses) can be established, as shown in Figure 73. With enough measured data, a modified asymmetrical Gompertz curve can be chosen to fit all the experimental results (compare Figure 71). It is to be expected that the conductivity increases from its baseline value σ_0 as the shock amplitude and duration are increased and eventually saturates at a maximum conductivity σ_{\max} . The fact that electrical conductivity should reach an upper limit (σ_{\max}) is related to the composition of adjacent tissue structures⁸⁶. Even if all cells become completely permeabilized, inherent resistance from support structures such as the extracellular matrix will contribute to tissue resistance. Because of the presence of such structures, the electrical conductivity plateau will be reached in the tissue.

After the relationship between conductivities and electric field strengths is established, we can update the constant conductivity in our numerical model with a fitted modified asymmetrical Gompertz function. This conductivity updates will make our model more precise than the current one.

5.2.2 SYNERGY ABLATION CLAMP DESIGN

AtriCure, Inc is a medical device company specializing in innovative cardiac surgical ablation systems for the treatment of atrial fibrillation. There is a collaboration between our lab and Atricure on several projects. There is a potential collaboration opportunity in the future that our nsPEF ablation can be mounted onto the AtriCure synergy ablation clamp as an innovative clinical tool. Whether we perform this project is contingent on reaching an agreement on the funding and scope of the project with AtriCure.

The Synergy ablation clamp is intended to ablate cardiac tissue for the treatment of patients with

persistent atrial fibrillation who are undergoing open concomitant coronary artery bypass grafting and/or valve replacement or repair. A typical ablation protocol that shows the lesions to be created with the Synergy clamp on the heart using Synergy is shown in Figure 74 (red lines show the lesions to be created with the Synergy tool).

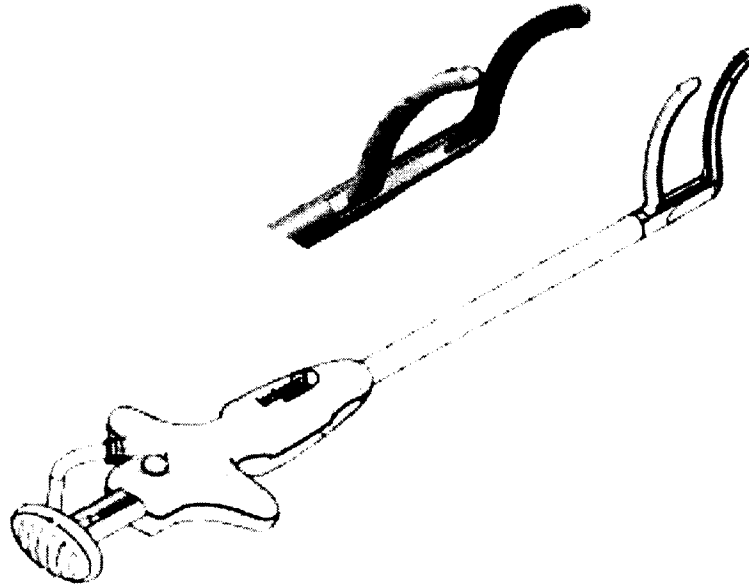


Figure 73. Synergy ablation clamp. The RF energy is delivered via the connector to the linear electrodes on the insulated jaws of the synergy ablation clamp.

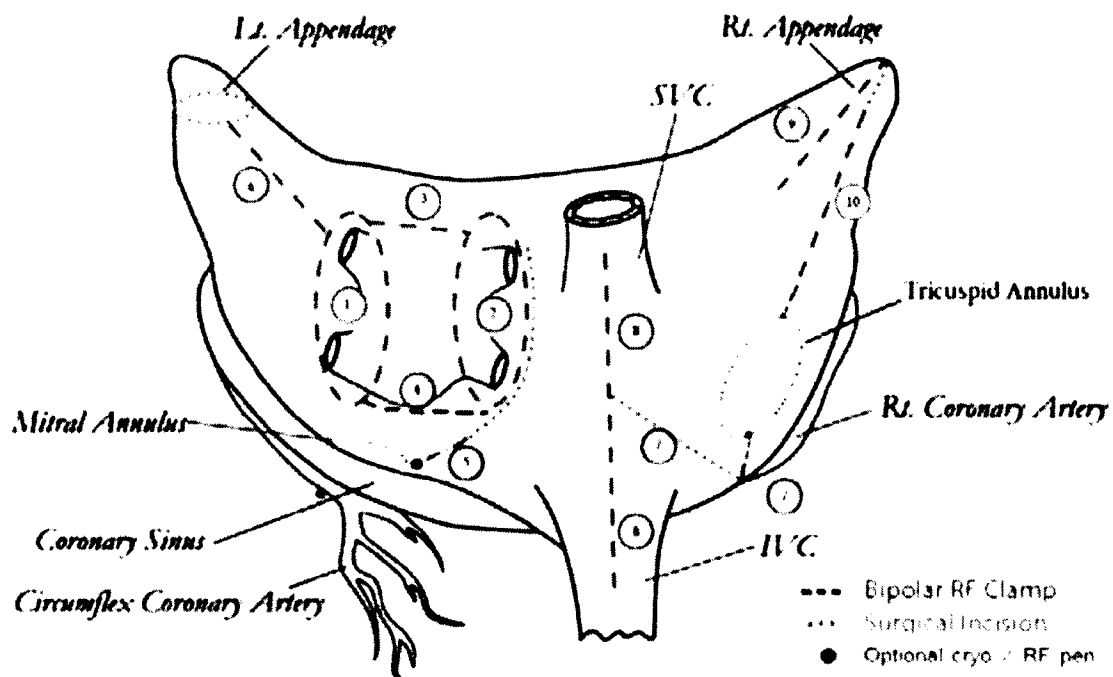


Figure 74. Ablation protocol using AtriCure synergy ablation clamp.

It is proposed that our nsPEFs can be used as the energy source, to deliver the IRE energy to the customized synergy ablation clamp. We will test the effectiveness of nsPEF ablation delivered through the synergy ablation clamp. This includes creating lesions in rabbit ventricles, using optical mapping to verify the creation of block, and histological characterization of the lesions. If nsPEF ablation with surgical clamps proves to be effective, it would open a more direct way into the clinical practice, because catheter development would not be needed for this technology. Although surgical ablation is not performed as frequently as catheter ablation in the heart, there are still more than 10,000 cases performed annually in the United States.

REFERENCES

1. Naccarelli, G. V., Varker, H., Lin, J. & Schulman, K. L. Increasing prevalence of atrial fibrillation and flutter in the United States. *Am. J. Cardiol.* **104**, 1534–1539 (2009).
2. Roger, V. L. *et al.* Heart disease and stroke statistics--2011 update: a report from the American Heart Association. *Circulation* **123**, e18–e209 (2011).
3. Marini, C. *et al.* Contribution of Atrial Fibrillation to Incidence and Outcome of Ischemic Stroke Results From a Population-Based Study. *Stroke* **36**, 1115–1119 (2005).
4. Go AS, H. E. Prevalence of diagnosed atrial fibrillation in adults: National implications for rhythm management and stroke prevention: the anticoagulation and risk factors in atrial fibrillation (atria) study. *JAMA* **285**, 2370–2375 (2001).
5. Thrall, G., Lane, D., Carroll, D. & Lip, G. Y. H. Quality of Life in Patients with Atrial Fibrillation: A Systematic Review. *Am. J. Med.* **119**, 448.e1–448.e19 (2006).
6. *Vander's Human Physiology: The Mechanisms of Body Function.* (McGraw-Hill Higher Education, 2011).
7. Douglas Zipes, Jose Jalife. *Cardiac electrophysiology 3 Ed: From cell to bedside.* Page **315**, Chapter **36**, Part **VII**, (W.B. Saunders Company, 2000).
8. Deneke, T. *et al.* Intra-operative cooled-tip radiofrequency linear atrial ablation to treat permanent atrial fibrillation. *Eur. Heart J.* **28**, 2909–2914 (2007).
9. Blaufox, A. D. Catheter Ablation of Tachyarrhythmias in Small Children. *Indian Pacing Electrophysiol. J.* **5**, 51–62 (2005).
10. Anonymous. Cooled Tip Catheter Ablation. *EP Lab Digest* (2008). at <http://www.eplabdigest.com/article/1382>
11. Nath, S., Dimarco, J. & Haines, D. Basic aspects of radiofrequency catheter ablation. *J. Cardiovasc. Electrophysiol.* **5**, 863–876 (1994).
12. Hanninen, M. *et al.* Cryoablation Versus RF Ablation for AVNRT: A Meta-analysis and

- Systematic Review. *J. Cardiovasc. Electrophysiol.* n/a–n/a (2013). doi:10.1111/jce.12247
13. Dorwarth, U. *et al.* Radiofrequency catheter ablation: different cooled and noncooled electrode systems induce specific lesion geometries and adverse effects profiles. *Pacing Clin. Electrophysiol. PACE* **26**, 1438–1445 (2003).
 14. Nakagawa, H. *et al.* Comparison of in vivo tissue temperature profile and lesion geometry for radiofrequency ablation with a saline-irrigated electrode versus temperature control in a canine thigh muscle preparation. *Circulation* **91**, 2264–2273 (1995).
 15. Khairy, P. *et al.* Lower incidence of thrombus formation with cryoenergy versus radiofrequency catheter ablation. *Circulation* **107**, 2045–2050 (2003).
 16. Morady, F. Catheter Ablation of Supraventricular Arrhythmias: *Pacing Clin. Electrophysiol.* **27**, 125–142 (2004).
 17. Katritsis, D. *et al.* Long-term follow-up after radiofrequency catheter ablation for atrial fibrillation. *Europace* **10**, 419–424 (2008).
 18. Microsoft Word - FY11-121-Heart Center AFib Handout_FINALPVI.MM.KS.6.9.11.doc - patientguidetopvi.pdf. at
<<http://www.massgeneral.org/heartcenter/assets/pdfs/patientguidetopvi.pdf>>
 19. Pilcher, T. A., Sanford, A. L., Saul, J. P. & Haemmerich, D. Convective cooling effect on cooled-tip catheter compared to large-tip catheter radiofrequency ablation. *Pacing Clin. Electrophysiol. PACE* **29**, 1368–1374 (2006).
 20. Thiagalingam, A. *et al.* Importance of catheter contact force during irrigated radiofrequency ablation: evaluation in a porcine ex vivo model using a force-sensing catheter. *J. Cardiovasc. Electrophysiol.* **21**, 806–811 (2010).
 21. Yokoyama, K. *et al.* Comparison of electrode cooling between internal and open irrigation in radiofrequency ablation lesion depth and incidence of thrombus and steam pop. *Circulation* **113**, 11–19 (2006).
 22. Hornero, F. *et al.* Intraoperative Cryoablation of Atrial Fibrillation With the Old-Fashioned Cryode Tips: A Simple, Effective, and Inexpensive Method. *Ann. Thorac. Surg.* **84**, 1408–1411

- (2007).
23. Neumann, E., Schaefer-Ridder, M., Wang, Y. and Holschneider, P.H. Gene transfer into mouse lymphoma cells by electroporation in high electric fields. *EMBO J.* **1**, 841–845. (1982).
 24. Prud'homme GJ, Glinka Y, Khan AS, Draghia-Akli R. Electroporation-enhanced nonviral gene transfer for the prevention or treatment of immunological, endocrine and neoplastic diseases. *Curr Gene Ther* **6**, 243–273 (2006).
 25. M L Escande-Géraud, M. P. R. Reversible plasma membrane ultrastructural changes correlated with electroporation in Chinese hamster ovary cells. *Biochim. Biophys. Acta* **939**, 247–59 (1988).
 26. Fromm, M., Taylor, L. P. & Walbot, V. Expression of genes transferred into monocot and dicot plant cells by electroporation. *Proc. Natl. Acad. Sci. U. S. A.* **82**, 5824–5828 (1985).
 27. Chen, X., James Swanson, R., Kolb, J. F., Nuccitelli, R. & Schoenbach, K. H. Histopathology of normal skin and melanomas after nanosecond pulsed electric field treatment. *Melanoma Res.* **19**, 361–371 (2009).
 28. Nuccitelli, R. *et al.* A new pulsed electric field therapy for melanoma disrupts the tumor's blood supply and causes complete remission without recurrence. *Int. J. Cancer* **125**, 438–445 (2009).
 29. Schoenbach, K. H. *et al.* Ultrashort electrical pulses open a new gateway into biological cells. *Proc. IEEE* **92**, 1122–1137 (2004).
 30. Davalos, R. V., Mir, I. L. M. & Rubinsky, B. Tissue ablation with irreversible electroporation. *Ann. Biomed. Eng.* **33**, 223–231 (2005).
 31. Kingham, T. P. *et al.* Ablation of Perivascular Hepatic Malignant Tumors with Irreversible Electroporation. *J. Am. Coll. Surg.* **215**, 379–387 (2012).
 32. Neal, R. E. *et al.* Successful Treatment of a Large Soft Tissue Sarcoma With Irreversible Electroporation. *J. Clin. Oncol.* **29**, e372–e377 (2011).
 33. Li, W., Fan, Q., Ji, Z., Qiu, X. & Li, Z. The Effects of Irreversible Electroporation (IRE) on Nerves. *PLoS ONE* **6**, e18831 (2011).
 34. Maor, E., Ivorra, A. & Rubinsky, B. Non Thermal Irreversible Electroporation: Novel

- Technology for Vascular Smooth Muscle Cells Ablation. *PLoS ONE* **4**, e4757 (2009).
35. Lavee, J., Onik, G., Mikus, P. & Rubinsky, B. A novel nonthermal energy source for surgical epicardial atrial ablation: irreversible electroporation. *Heart Surg. Forum* **10**, E162–167 (2007).
 36. Wittkamp, F. H. *et al.* Feasibility of electroporation for the creation of pulmonary vein ostial lesions. *J. Cardiovasc. Electrophysiol.* **22**, 302–309 (2011).
 37. Wittkamp, F. H. M. *et al.* Myocardial Lesion Depth With Circular Electroporation Ablation. *Circ. Arrhythm. Electrophysiol.* **5**, 581–586 (2012).
 38. Gowrishankar, T. R., Esser, A. T., Vasilkoski, Z., Smith, K. C. & Weaver, J. C. Microdosimetry for conventional and supra-electroporation in cells with organelles. *Biochem. Biophys. Res. Commun.* **341**, 1266–1276 (2006).
 39. Gowrishankar, T. R. & Weaver, J. C. Electrical behavior and pore accumulation in a multicellular model for conventional and supra-electroporation. *Biochem. Biophys. Res. Commun.* **349**, 643–653 (2006).
 40. Smith, K. C. & Weaver, J. C. Active Mechanisms Are Needed to Describe Cell Responses to Submicrosecond, Megavolt-per-Meter Pulses: Cell Models for Ultrashort Pulses. *Biophys. J.* **95**, 1547–1563 (2008).
 41. Esser, A. T., Smith, K. C., Gowrishankar, T. R. & Weaver, J. C. Towards solid tumor treatment by nanosecond pulsed electric fields. *Technol. Cancer Res. Treat.* **8**, 289–306 (2009).
 42. Smith, K. C. & Weaver, J. C. Transmembrane molecular transport during versus after extremely large, nanosecond electric pulses. *Biochem. Biophys. Res. Commun.* **412**, 8–12 (2011).
 43. Joshi, R. P. & Schoenbach, K. H. Bioelectric effects of intense ultrashort pulses. *Crit. Rev. Biomed. Eng.* **38**, 255–304 (2010).
 44. Xiao, D. *et al.* Irreversible electroporation and apoptosis in human liver cancer cells induced by nanosecond electric pulses. *Bioelectromagnetics* **34**, 512–520 (2013).
 45. Vernier, P. T., Sun, Y. & Gundersen, M. A. Nanoelectropulse-driven membrane perturbation and small molecule permeabilization. *BMC Cell Biol.* **7**, 37 (2006).
 46. Tekle, E. *et al.* Selective Field Effects on Intracellular Vacuoles and Vesicle Membranes with

- Nanosecond Electric Pulses. *Biophys. J.* **89**, 274–284 (2005).
47. Pakhomov, A. G. *et al.* Membrane permeabilization and cell damage by ultrashort electric field shocks. *Arch. Biochem. Biophys.* **465**, 109–118 (2007).
 48. Chen, X., Swanson, R. J., Kolb, J. F., Nuccitelli, R. & Schoenbach, K. H. Histopathology of normal skin and melanomas after nanosecond pulsed electric field treatment. *Melanoma Res.* **19**, 361–371 (2009).
 49. Nuccitelli, R. *et al.* Nanosecond pulsed electric fields cause melanomas to self-destruct. *Biochem. Biophys. Res. Commun.* **343**, 351–360 (2006).
 50. Edd, J. F. & Davalos, R. V. Mathematical modeling of irreversible electroporation for treatment planning. *Technol. Cancer Res. Treat.* **6**, 275–286 (2007).
 51. Arena, C. B., Szot, C. S., Garcia, P. A., Rylander, M. N. & Davalos, R. V. A Three-Dimensional In Vitro Tumor Platform for Modeling Therapeutic Irreversible Electroporation. *Biophys. J.* **103**, 2033–2042 (2012).
 52. Corovic, S. *et al.* Modeling of electric field distribution in tissues during electroporation. *Biomed. Eng. OnLine* **12**, 16 (2013).
 53. Garcia, P. A., Rossmeisl, J. H., Neal, R. E., Ellis, T. L. & Davalos, R. V. A Parametric Study Delineating Irreversible Electroporation from Thermal Damage Based on a Minimally Invasive Intracranial Procedure. *Biomed. Eng. OnLine* **10**, 34 (2011).
 54. Zupanic, A., Corovic, S., Miklavcic, D. & Pavlin, M. Numerical optimization of gene electrotransfer into muscle tissue. *Biomed. Eng. OnLine* **9**, 66 (2010).
 55. I. Lacković, R. M. Influence of anisotropic tissue electrical conductivity on electric field and temperature distribution during electroporation-based therapy. 210–213 (2010).
doi:10.1007/978-3-642-03895-2_62
 56. Lou, Q., Li, W. & Efimov, I. R. Multiparametric Optical Mapping of the Langendorff-perfused Rabbit Heart. *J. Vis. Exp.* (2011). doi:10.3791/3160
 57. Lou, Q., Li, W. & Efimov, I. R. Multiparametric Optical Mapping of the Langendorff-perfused Rabbit Heart. *J. Vis. Exp. JoVE* (2011). doi:10.3791/3160

58. Propidium iodide. *Wikipedia, the free encyclopedia* (2015). at http://en.wikipedia.org/w/index.php?title=Propidium_iodide&oldid=641813565
59. Holmbom, B., Näslund, U., Eriksson, A., Virtanen, I. & Thornell, L. E. Comparison of triphenyltetrazolium chloride (TTC) staining versus detection of fibronectin in experimental myocardial infarction. *Histochemistry* **99**, 265–275 (1993).
60. Adegboyega, P. A., Adesokan, A., Haque, A. K. & Boor, P. J. Sensitivity and specificity of triphenyl tetrazolium chloride in the gross diagnosis of acute myocardial infarcts. *Arch. Pathol. Lab. Med.* **121**, 1063–1068 (1997).
61. Lippold, H. J. Quantitative succinic dehydrogenases histochemistry. A comparison of different tetrazolium salts. *Histochemistry* **76**, 381–405 (1982).
62. Honjo, I. & Ozawa, K. Lysolecithin inhibition of mitochondrial metabolism. *Biochim. Biophys. Acta BBA - Bioenerg.* **162**, 624–627 (1968).
63. Smith, P. W. *Transient electronics: pulsed circuit technology*. (J. Wiley, 2002).
64. Basic pulse forming circuit. at http://www.kentech.co.uk/index.html?/tl_basic_pfl.html&2
65. LeGrice, I. J. *et al.* Laminar structure of the heart: ventricular myocyte arrangement and connective tissue architecture in the dog. *Am. J. Physiol. - Heart Circ. Physiol.* **269**, H571–H582 (1995).
66. Rogers, K. *The Cardiovascular System*. (The Rosen Publishing Group, 2010).
67. Thiriet, M. *Diseases of the Cardiac Pump*. (Springer, 2015).
68. Geerts, L., Bovendeerd, P., Nicolay, K. & Arts, T. Characterization of the normal cardiac myofiber field in goat measured with MR-diffusion tensor imaging. *Am. J. Physiol. Heart Circ. Physiol.* **283**, H139–145 (2002).
69. Seemann, G., Keller, D. U. J., Weiss, D. L. & Dossel, O. Modeling human ventricular geometry and fiber orientation based on diffusion tensor MRI. in *Computers in Cardiology, 2006* 801–804 (2006).
70. Pravdin, S. F. *et al.* Mathematical model of the anatomy and fibre orientation field of the left ventricle of the heart. *Biomed. Eng. OnLine* **12**, 54 (2013).

71. Healy, L. J., Jiang, Y. & Hsu, E. W. Quantitative comparison of myocardial fiber structure between mice, rabbit, and sheep using diffusion tensor cardiovascular magnetic resonance. *J. Cardiovasc. Magn. Reson.* **13**, 74 (2011).
72. AndrewD McCulloch. in *Biomedical Engineering Fundamentals* 54–1–54–27 (CRC Press, 2006). at <<http://www.crcnetbase.com/doi/abs/10.1201/9781420003857.ch54>>
73. Streeter, D. D., Spotnitz, H. M., Patel, D. P., Ross, J. & Sonnenblick, E. H. Fiber Orientation in the Canine Left Ventricle during Diastole and Systole. *Circ. Res.* **24**, 339–347 (1969).
74. Basser, P. J. & Pierpaoli, C. Microstructural and physiological features of tissues elucidated by quantitative-diffusion-tensor MRI. *J. Magn. Reson. B* **111**, 209–219 (1996).
75. Robert E Neal, R. V. D. The feasibility of irreversible electroporation for the treatment of breast cancer and other heterogeneous systems. *Ann. Biomed. Eng.* **37**, 2615–25 (2009).
76. Schwab, B. C. *et al.* Quantitative Analysis of Cardiac Tissue Including Fibroblasts Using Three-Dimensional Confocal Microscopy and Image Reconstruction: Towards a Basis for Electrophysiological Modeling. *IEEE Trans. Med. Imaging* **32**, 862–872 (2013).
77. Muscle. *Wikipedia, the free encyclopedia* (2015). at <<http://en.wikipedia.org/w/index.php?title=Muscle&oldid=650167001>>
78. Bello, O. The Specific Heat Capacity Of Some Internal Tissues And Organs Of Cow. *Afr. J. Phys. Sci.* **Volume 2**, (2009).
79. Kim, D.-H. *et al.* Electronic sensor and actuator webs for large-area complex geometry cardiac mapping and therapy. *Proc. Natl. Acad. Sci. U. S. A.* **109**, 19910–19915 (2012).
80. Bishop, M. J. & Plank, G. Representing Cardiac Bidomain Bath-Loading Effects by an Augmented Monodomain Approach: Application to Complex Ventricular Models. *IEEE Trans. Biomed. Eng.* **58**, 1066–1075 (2011).
81. Pravdin, S. F. *et al.* Mathematical model of the anatomy and fibre orientation field of the left ventricle of the heart. *Biomed. Eng. OnLine* **12**, 54 (2013).
82. Traill, T. A., Gibson, D. G. & Brown, D. J. Study of left ventricular wall thickness and dimension changes using echocardiography. *Br. Heart J.* **40**, 162–169 (1978).

83. Neal, R. E. *et al.* In vivo characterization and numerical simulation of prostate properties for non-thermal irreversible electroporation ablation. *The Prostate* **74**, 458–468 (2014).
84. Rubinsky, B. *Irreversible Electroporation*. (Springer Science & Business Media, 2009).
85. Lee, R. C., Zhang, D. & Hannig, J. Biophysical injury mechanisms in electrical shock trauma. *Annu. Rev. Biomed. Eng.* **2**, 477–509 (2000).
86. Neal, R. E., Garcia, P. A., Robertson, J. L. & Davalos, R. V. Experimental characterization and numerical modeling of tissue electrical conductivity during pulsed electric fields for irreversible electroporation treatment planning. *IEEE Trans. Biomed. Eng.* **59**, 1076–1085 (2012).
87. Gielen, F. L., Wallinga-de Jonge, W. & Boon, K. L. Electrical conductivity of skeletal muscle tissue: experimental results from different muscles in vivo. *Med. Biol. Eng. Comput.* **22**, 569–577 (1984).
88. Bradley J Roth. in *The Biomedical Engineering Handbook, Second Edition. 2 Volume Set* (CRC Press, 1999). at <<http://www.crcnetbase.com/doi/abs/10.1201/9781420049510.ch10>>
89. Fratzl, P. *Collagen: Structure and Mechanics*. (Springer Science & Business Media, 2008).
90. Medical School • The human heart in cross section. *Medical School* at <<http://medicalschooll.tumblr.com/post/35136168795/the-human-heart-in-cross-section>>
91. Martin, R. B. *Skeletal tissue mechanics / Burr, David B.* (Springer, 1998).
92. Kandušer, M. & Miklavčič, D. in *Electrotechnologies for Extraction from Food Plants and Biomaterials* 1–37 (Springer New York, 2009). at <http://link.springer.com/chapter/10.1007/978-0-387-79374-0_1>
93. Lou, Q., Li, W. & Efimov, I. R. Multiparametric Optical Mapping of the Langendorff-perfused Rabbit Heart. *J. Vis. Exp.* (2011). doi:10.3791/3160
94. Thiagalingam, A., Campbell, C. R., Boyd, A., Ross, D. L. & Kovoov, P. Catheter intramural needle radiofrequency ablation creates deeper lesions than irrigated tip catheter ablation. *Pacing Clin. Electrophysiol. PACE* **26**, 2146–2150 (2003).
95. Latchamsetty, R. & Oral, H. Ablation of atrial fibrillation using an irrigated-tip catheter: open

- or closed? *Pacing Clin. Electrophysiol. PACE* **35**, 503–505 (2012).
96. Haines, D. The biophysics of radiofrequency catheter ablation in the heart: the importance of temperature monitoring. *Pacing Clin. Electrophysiol.* **16**, 586–591 (1993).
97. Ho, S. Y., Anderson, R. H. & Sánchez-Quintana, D. Atrial structure and fibres: morphologic bases of atrial conduction. *Cardiovasc. Res.* **54**, 325–336 (2002).

VITA

Fei Xie

Education:

PhD in Biomedical Engineering program, Old Dominion University, May 2015.

MSc in RF Communications System, University of Southampton, UK, March 2006.

BEng in Telecommunications Engineering, Chongqing University, China, July 2004.

Selected Peer-Reviewed Publications:

1. **Fei Xie**, Christian Zemlin “Filter design for optically recorded cardiac electrical activity recorded during ischemia”, *International Journal of Sciences: Basic and Applied Research*, Vol 15, No 2, 2014.
2. Ren Wang, Peng Cheng, **Fei Xie**, Darrin Young, and Zhili Hao, "A Multiple-beam tuning-fork Gyroscopes with high Quality factors," *Sensors and Actuators A*, 2011.

Selected Conference Papers:

1. **Fei Xie**, Christian Zemlin, “Fast and precise ablation with nanosecond pulsed electric fields”, *Heart Rhythm Society's 35th Annual Scientific Sessions, San Francisco, May 7-10, 2014, Heart Rhythm, Volume 11, No.5, pp. S337.*
2. **Fei Xie**, F. Varghese, S. Xiao, and C. W. Zemlin, “Ablation of Myocardial Tissue with Nanosecond Pulsed Electric Fields”, *Heart Rhythm, Denver, May 8, 2013.*

Selected Conference Presentations:

1. “Ablation of Myocardial Tissue with Nanosecond Pulsed Electric Fields”, *Biomedical Engineering Regional Career Conference (SEMABECC), Washintong. DC. Oct 25th, 2013*
2. “Treating Cardiac Arrhythmias with Nanosecond Pulsed Electric Fields”, *Bioelectronics, Karlsruhe, Germany, 2013.*
3. “Filtering of movies of cardiac activity: how to improve signals withoutdistorting them ”, *IEEE Signal Processing in Medicine and Biology Symposium (spmb12), City College of New York, December 1st, 2012.*